HORIZONTAL BLOCH LINE MOTION IN MAGNETIC BUBBLE MATERIALS

Thesis by

Bruce E. MacNeal

In Partial Fulfillment of the Requirements

for the Degree of

Doctor of Philosophy

California Institute of Technology

Pasadena, California

1979

(Submitted April 24, 1979)

to my parents

Acknowledgements

I would like to acknowledge the assistance of those individuals and organizations who have helped to make this work possible. First and foremost, I would like to thank my thesis advisor, Professor Floyd B. Humphrey, for his invaluable assistance and patience during the course of this work. I would also like to thank Professor Charles H. Wilts, Timothy J. Gallagher, Dr. Kochan Ju, Kadri Vural, Dr. Laslo Gal, Tsutomu Kobayashi, and Dr. George J. Zimmer for their many helpful discussions of wall motion. I would like to thank Terry Morris for showing me the equipment and Stanley H. Bacon for his help in designing the photometric experiment. I would like to express my gratitude to the California Institute of Technology, the International Business Machines Corporation, and the National Science Foundation for their financial assistance. Finally, I would like to thank Mrs. Vere Snell for her able assistance in preparing the manuscript.

Abstract

The purpose of this work is to extend experimental and theoretical understanding of horizontal Bloch line (HBL) motion in magnetic bubble materials. The present theory of HBL motion is reviewed, and then extended to include transient effects in which the internal domain wall structure changes with time. This is accomplished by numerically solving the equations of motion for the internal azimuthal angle ϕ and the wall position q as functions of z, the coordinate perpendicular to the thin-film material, and time. The effects of HBL's on domain wall motion are investigated by comparing results from wall oscillation experiments with those from the theory. In these experiments, a bias field pulse is used to make a step change in equilibrium position of either bubble or stripe domain walls, and the wall response is measured by using transient photography. During the initial response, the dynamic wall structure closely resembles the initial static structure. The wall accelerates to a relatively high velocity ($\approx$20 m/sec), resulting in a short ($\approx$ 22 nsec) section of initial rapid motion. An HBL gradually forms near one of the film surfaces as a result of local dynamic properties, and moves along the wall surface toward the film center. The presence of this structure produces low-frequency, triangular-shaped oscillations in which the experimental wall velocity is nearly constant, $v_s \approx$ 5-8 m/sec. If the HBL reaches the opposite surface,

i.e., if the average internal angle reaches an integer multiple of π, the momentum stored in the HBL is lost, and the wall chirality is reversed. This results in abrupt transitions to overdamped motion and changes in wall chirality, which are observed as a function of bias pulse amplitude. The pulse amplitude at which the n^{th} punch-through occurs just as the wall reaches equilibrium is given within 0.2 Oe by $H_n = (2v_s H'/\gamma)^{\frac{1}{2}} \cdot (n\pi)^{\frac{1}{2}} + H_{sv}$, where H' is the effective field gradient from the surrounding domains, and H_{sv} is a small (<0.03 Oe), effective drag field. Observations of wall oscillation in the presence of in-plane fields parallel to the wall show that HBL formation is suppressed by fields greater than about 40 Oe ($\approx 2\pi M_s$), resulting in the high-frequency, sinusoidal oscillations associated with a simple internal wall structure.

TABLE OF CONTENTS

Chapter 1

Introduction

Magnetic bubble devices [1-4] represent a new solid state digital storage technology. In these devices, small (< 5 μm) cylindrical domains, called magnetic bubbles, move through a thin-film ferromagnetic material. These domains are actually regions where the magnetization $\overline{M}$ is perpendicular to the film plane, and opposite to $\overline{M}$ in the surrounding material. An external bias field directed anti-parallel to $\overline{M}$ in the bubble is required for stability. The bubbles are manipulated by a rotating external in-plane field through a series of thin (<5000 Å) evaporated permalloy overlay structures. These overlays are usually arranged in the form of continuous shift registers. As bubbles move around the registers in a lock-step manner, bit information is stored by the presence or absence of a bubble at each bit location. A typical bubble chip in production today contains several hundred of these minor loop registers, each containing about 1000 bits of information. The register period is about 14 μm, which gives a typical storage density of 10^6 bits/cm^2. Information is decoded by replicating the bubble pattern from each minor loop into a common major loop register, and then transferring the bubble patterns to a magnetoresistive detector [5,6]. There, bubbles are stretched into long (10^2 μm) stripe domains oriented perpendicular to the propagation direction. As the stripe passes under the permalloy conductor detector, the stray magnetic fields cause a 5% change in electrical

resistance, which is detected electronically. Other functions necessary for complete device operation, such as selective switching [7], replication-transfer [8], nucleation [9], and annihilation are implemented by a combination of current conductors and overlay structures. In addition, certain binary logic operations [2], which make use of bubble-bubble interactions, make possible on-chip data processing [10,11]. With the in-plane field rotating at 100 KHz, typical average access times of 0.5 msec, and data rates of 10^5 bits/sec have been achieved. Present individual chip capacity is typically 300 Kbits [12], but designs with up to 1 Mbit are available [13]. Complete bubble memory systems, which contain several chips mounted in a common bias field and rotating field assembly, are now available.

Propagation of bubbles with the classic T-bar overlay structure [14] is shown in Fig. (1.1). When a uniform in-plane field is applied to the magnetically soft permalloy overlays, magnetic poles from $\nabla \cdot \overline{M}$ are produced at the edges. Bubbles in the underlying material are attracted to positive poles, and repelled by negative poles. Since the location of these poles depends on in-plane field orientation, the bubbles slide along the overlay structures as the in-plane field rotates. For example, with $+H_y$ (case A), bubbles are located under the positive pole at the center of the T element. When the field rotates by 90° to $+H_x$ (case B), the bubble moves to the right side of the T element. When the field rotates to $-H_y$ (case C), the bubble moves across the gap to the lower end of the bar element. When the field rotates to $-H_x$ (case D), the bubble moves across the second gap

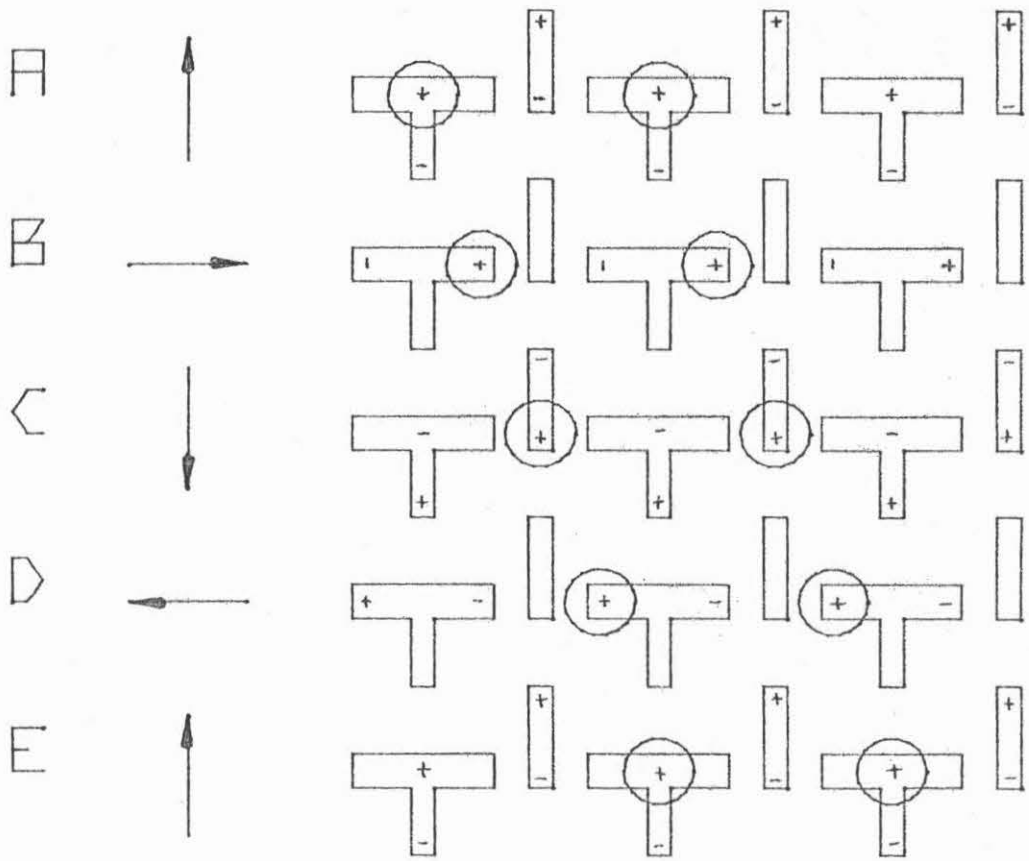

Fig. 1.1. Propagation of Bubbles by T-bar Overlay Structures. As the in-plane field (indicated by arrows) rotates, the magnetic poles (+ or -) in the permalloy overlay structures change position, and the bubbles, which are located under the overlays, move along the register by one bit location for each 360° rotation.

to the left side of the next T element. Finally, when the in-plane field returns to $+H_y$ (case E), the bubble moves again to the center of the T element. In this way, bubbles advance along the shift register by one bit position each time the in-plane field rotates by 360°. A number of similar propagation structures, such as the Y-bar [15], X-bar [16], and Y-Y [7] designs, have also been developed. Recently, gap-tolerant structures [17], such as the asymmetric half-disc [18], have been developed to relax lithographic requirements. Each of these structures operates on the same principle as the basic T-bar design.

Bubble devices have significant advantages over existing semiconductor and magnetic disk recording technologies [4]. Unlike semiconductor memory, bubble memory is non-volatile, i.e., power is not required to maintain stored information. Bubbles also promise a lower per-bit cost because of higher storage densities. At present, bubble and semiconductor densities are about the same, but with new propagation mechanisms [19,20] and E-beam (0.25 μm) lithography, bubbles may surpass the ultimate semiconductor density (10^7 bits/cm^2) by an order of magnitude. Bubbles also promise higher yields because of much easier fabrication techniques. Semiconductor memory requires at least five masking levels, some of which involve active diffusion into the Si substrate, while bubbles require two, and perhaps just one [21] passive overlay level. This advantage has already resulted in larger bubble chip capacity (1 Mbit) with satisfactory yields. Because magnetic disk devices distribute the cost of expensive mechanical drive equipment over many bits (10^9), the per-bit cost is much lower than

for bubbles. Thus, bubbles will probably be cost competitive only for small ($< 10^7$ bit) memory applications. However, the absence of moving parts makes bubbles more attractive from a reliability and maintenance standpoint. Furthermore, bubble access times are much shorter than for either fixed-head (20 msec) or movable-head (100 msec) disk devices. Finally, the possibility of asynchronous operation, and on-chip logic functions make bubbles more versatile. Bubble memory, which combines the simplicity and reliability of solid state operation with the low cost and non-volatility of magnetic storage, fills the technological gap between existing semiconductor and magnetic disk devices.

Bubble materials [22] must satisfy certain requirements, which are imposed by the technology. Bubble stability requires a strong magnetic easy axis perpendicular to the plane of the material. To prevent the coherent rotation of $\overline{M}$ into the plane, the magnetic anisotropy energy density K_u must satisfy

$$K_u/2\pi M_s^2 = Q > 1 \quad , \tag{1.1}$$

where $M_s = |\overline{M}|$, and Q is the so-called quality factor. Stability also requires that the bubble radius r_o and film thickness h satisfy

$$r_o = h = \frac{\sigma_w}{\pi M_s^2} \quad , \tag{1.2}$$

where the wall energy per unit area σ_w describes surface tension. Bubble walls must move freely under the influence of relatively small drive fields H_z. It will be shown in Ch. 2 that the theoretical wall velocity is given in the simplest approximation by

$$V = \mu(H_z - H_{co}) \quad , \tag{1.3}$$

where μ is the wall mobility, and H_{co} is the coercive field. Thus, bubble materials should have high mobilities, and low coercive fields. Material defects, which can produce large barriers to wall motion, must be eliminated. In order to ensure device operation over an acceptable temperature range, material properties must vary slowly with temperature. Finally, material characteristics must be constant within a single chip, and reproducible from one chip to the next.

Single-crystal rare-earth-iron garnets are, at present, the only materials used in bubble devices. These materials have a garnet crystal structure with nominal chemical composition, $\{RE_3\}\ [Fe_2]\ [Fe_3]\ O_{12}$. The iron ions occupy two separate ferromagnetic sublattices, while coupling between sublattices is antiferromagnetic. The intrinsic or stress-induced anisotropy found in these crystals is normally too small for device applications. However, Bobeck et al.[23] found that garnets with a number of different rare-earth ions can have a large growth-induced anisotropy of the proper type. The origin of this anisotropy is not well understood, but it can be controlled by using empirical formulas. The magnetization is controlled by substituting various nonmagnetic ions into the three sublattices. Since the magnetic moment of each sublattice depends on temperature, there is a unique compensation temperature at which the total moment is zero. Satisfactory device operation has been achieved over the range, -50°C to 100°C, by adjusting the compensation point so that the

temperature dependence matches that of the permanent bias magnet. Garnets flux-grown on nonmagnetic garnet substrates through LPE yield satisfactory coercivities (< 0.5 Oe), and defect densities (< 5 per cm^2). Attempts to produce high-velocity samples have met with limited success. Low-α materials have been produced, but the presence of internal wall structures prevents the realization of large velocities. High-γ materials have also been produced, but large temperature dependences make them unsuitable for use in devices. Because various ions can be substituted into the three crystal sublattices, magnetic characteristics can be controlled over a wide range of parameters. This feature makes magnetic garnets attractive for device applications.

Amorphous alloys of the form Gd-Co-X (X = Mo, Cu, Au, Cr) are also being considered as bubble materials [22, 24, 25]. These materials have two advantages over the garnets: lower material cost, and smaller bubble size. These materials are deposited on glass or Si substrates by sputtering or evaporation, thus eliminating the need for more expensive single-crystal substrates. The required perpendicular anisotropy, also growth-induced, has been found in sputtered alloys [26], but it is sensitive both to composition and preparation conditions. The magnetization is generally an order of magnitude larger than in garnets, and varies significantly with composition. In order to obtain bubbles large enough for device applications [see Eq. (1.2)], it is necessary to use compositions near the compensation point. Unfortunately, the extreme temperature sensitivity of these compositions

poses a major problem in device design. Sufficiently high wall velocities have been observed [27,28], but control of coercivity has been another major problem. Amorphous materials also exhibit oxidation, which is not found in garnets. These materials show promise in small-bubble applications, but a number of problems, especially temperature sensitivity, must first be solved.

Since thin-film garnets are nearly transparent, domains are most easily observed by using the Faraday effect [29]. When plane-polarized light passes through the material along the easy axis, the plane of polarization rotates by a small amount (<1°). The sense of rotation depends on whether $\overline{M}$ is parallel or antiparallel to the propagation direction. Contrast is produced by passing the light through an analyzer with its transmission direction perpendicular to one of the rotated polarizations. In this way, domains with opposite orientations of $\overline{M}$ along the easy axis can be seen with a microscope as a series of light and dark images.

Two domain configurations commonly found in bubble materials are shown schematically in Fig. (1.2). In the demagnetized state with zero bias field, the material is divided by a series of serpentine stripe domains in which $\overline{M}$ alternates between opposite directions along the easy axis [Fig. (1.2a)]. When the bias field $\overline{H}_B$ is applied, those stripes with $\overline{M}$ parallel to $\overline{H}_B$ expand at the expense of the antiparallel domains. The stripe widths d_1 and d_2 are functions of H_B, h, and σ_w. When H_B exceeds about 2.5 M_s, stripe domains become unstable. The

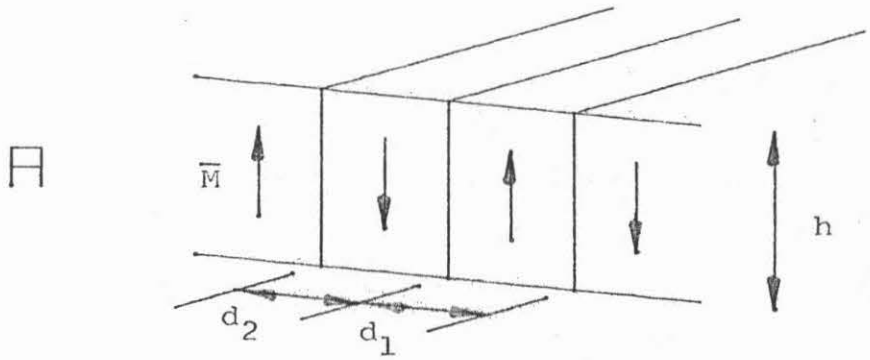

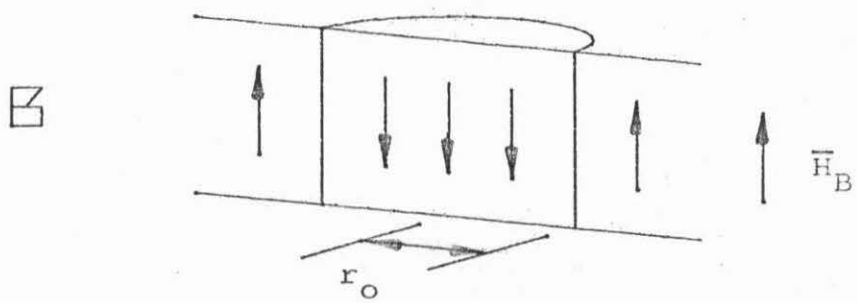

Fig. 1.2. Schematic Diagram of Stripe (A) and Bubble Domains (B) Found in Thin-Film Bubble Materials. The directions of the magnetization $\overline{M}$ and bias field $\overline{H}_B$ are indicated. The stripe widths d_1 and d_2, the film thickness h, and the bubble radius r_o are also shown.

stripe ends move in from the material boundaries and contract into bubble domains [Fig. (1.2b)] with $\overline{M}$ inside opposite to $\overline{H}_B$. The equilibrium bubble radius is also a function of H_B, h, and σ_w. Bubbles are only stable over a limited bias field range. If H_B is too large, the bubbles collapse, leaving the material saturated with $\overline{M}$ parallel to $\overline{H}_B$, and if H_B is too small the bubbles stripe out. A quantitative analysis of the static properties of bubble and stripe domains is given in Appendix A.

Domain walls in both configurations can contain internal wall structure like those shown schematically in Fig. (1.3). Domain walls are narrow regions in which $\overline{M}$ rotates between opposite orientations along the easy axis. In the wall center, $\overline{M}$ lies in the plane of the material. It is shown in Ch. 2 that in a static wall this center spin must be tangent to the wall surface in order to minimize wall energy. The center spin may point in opposite directions, so that there are two physically distinct static wall types. These two walls are said to have opposite senses of wall chirality. In the simplest case, unichiral bubbles only contain one sense of chirality. A more complicated example, in which the bubble contains both senses of chiralty, is shown in Fig. (1.2a). On the left side, the center spins point counterclockwise around the circumference, while on the right side, the center spins point clockwise. These regions are separated by an internal wall structure, called a vertical Bloch line (VBL), which is indicated by a dashed line. Naturally, since the total rotation of the center spin around the circumference must be an

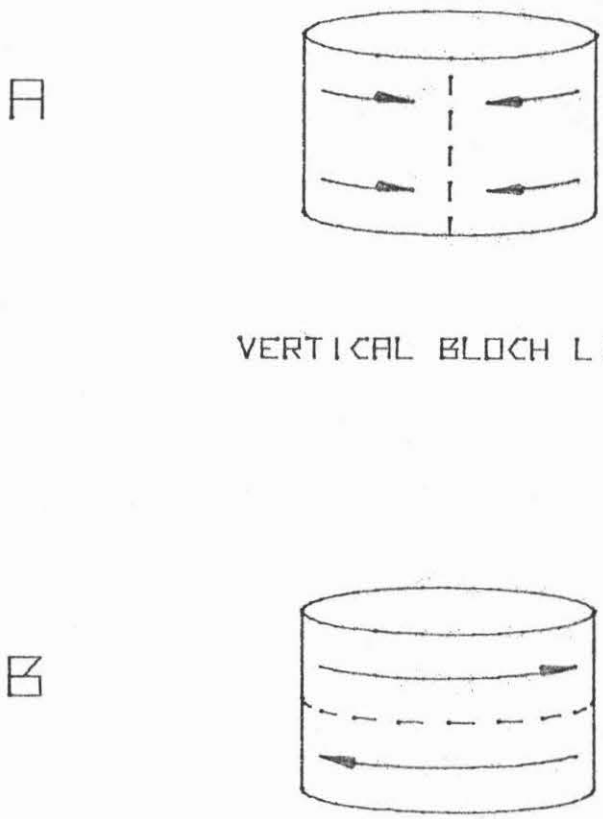

Fig. 1.3. Schematic Diagram of Vertical and Horizontal Bloch Line Structures in Bubble Domain Walls. These structures, which are indicated by dashed lines, separate regions of opposite wall chirality.

integer multiple of 2π, at least one additional VBL (not shown) must be present. A second example, in which opposite chiralities are separated by horizontal Bloch line (HBL), is shown in Fig. (1.3b). The presence of either structure is thought to strongly affect dynamic wall properties. For this reason, internal structure has become an important factor in device design.

There is strong experimental evidence for the existence of vertical Bloch lines. These structures have been seen in thin metal foils by using Lorentz microscopy [30,31] as abrupt changes in chirality. Such direct observations are not possible in thicker bubble materials; however, much indirect evidence has been accumulated by investigating the effects of VBL's on static and dynamic wall properties. Bubbles containing a large number of VBL's are more resistant to bubble collapse due to mutual Bloch line repulsion. These "hard" bubbles, which collapse at anomalously high bias fields, are often seen experimentally [32]. Hard wall sections, which exhibit greatly reduced velocities [33,34], have been observed in stripe domains [35]. The presence of VBL's can produce transverse forces [36] and shape distortions [37] which are observed during bubble translation. There is little doubt that VBL's exist in bubble materials, and that they are responsible for a variety of static and dynamic effects.

The existence of horizontal Bloch lines is much less certain. These structures are only thought to occur in moving walls, so that their presence is only detectable in dynamic effects such as velocity saturation, and dynamic conversion. It was found experimentally [38-40]

that wall velocities increase linearly with H_z, but the slope is usually much lower than the theoretical wall mobility. Beyond a certain point, the velocity becomes saturated, i.e., independent of H_z, with a typical value between 5 and 20 m/sec. One explanation of this phenomenon [41] involves the continuous motion of HBL's between the film surfaces. The dynamic conversion of VBL structures during bubble translation [42] has also been explained by HBL motion [43]. Unfortunately, neither of these effects require the existence of HBL's as specific micromagnetic structures. It will be shown in Ch. 2 that reasonable agreement with observed saturation velocities can be obtained by assuming different internal structures. Dynamic conversion can also be explained as a result of local Walker breakdown[44] or Bloch ring nucleation [45]. Hence, the dynamic effects now attributed to HBL's may be equally well explained by other mechanisms.

The wall oscillation phenomenon studied here provides a unique opportunity to investigate the effects of HBL's on wall motion. When a wall is subjected to a step change in equilibrium position, it oscillates about its new equilibrium position in some low-loss bubble materials. The rate at which these wall oscillations are damped depends on the energy losses associated with wall motion. Their frequency depends both on the effective wall mass, and on the restoring force provided by the surrounding domains. Walls with the simplest, unichiral structure have a uniform mass density, which is characteristic of the material. More complex walls exhibit inertial properties, which are dominated by internal structure. The wall

oscillation phenomenon is used here as a sensitive probe into the nature of these internal wall structures.

The Thesis

The purpose of this work is to extend experimental and theoretical understanding of horizontal Bloch line motion in magnetic bubble materials. A model of wall motion in bubble materials is presented in Ch. 2. The existing model is extended in order to analyze transient wall response by numerically solving the equations of motion. An experimental investigation of wall oscillations in a low-loss material is presented in Ch. 3. It is shown that the unusual dynamic behavior found during wall oscillation is due to the presence of horizontal Bloch lines. The relationship between the loss of stored momentum and changes in wall chirality during HBL instabilities is demonstrated for the first time. Finally, HBL nucleation is studied by investigating wall oscillation in the presence of in-plane fields. These results constitute the first experimental evidence for the existence of horizontal Bloch lines as specific micromagnetic structures.

References

1. A. H. Bobeck, P. I. Bonyhard, and J. E. Geusic, IEEE Proc. 63, 1176 (1975).

2. A. H. Bobeck and H. E. D. Scovil, Scientific American 224, 78 (June, 1971).

3. A. B. Smith, Bubble-Domain Memory Devices (Artech House, Dedham, Mass., 1974).

4. Magnetic Bubble Technology: Integrated-Circuit Magnetics for Digital Storage and Processing, ed. Hsu Chang, (IEEE Press, New York, 1975).

5. L. R. Tocci, P. K. George, and J. L. Archer, AIP Conf. Proc. 10, 197 (1972).

6. W. Strauss, A. H. Bobeck, and F. J. Ciak, AIP Conf. Proc. 10, 202 (1972).

7. F. Yamauchi, K. Hoshimi, S. Fugiwara, and T. Furouya, IEEE Trans. MAG-8, 372 (1972).

8. P. I. Bonyhard, Y. S. Chen, and J. L. Smith, AIP Conf. Proc. 18, 100 (1974).

9. T. J. Nelson, Y. S. Chen, and J. E. Geusic, IEEE Trans. MAG-9, 289 (1973).

10. Hsu Chang, J. Fox, D. Lu, and L. L. Rosier, IEEE Trans. MAG-8, 214 (1972).

11. R. C. Minnick, P. T. Bailey, R. M. Sandfort, and W. L. Semon, Proc.

Fall Joint Computer Conf.,1279 (1972). Reprinted in Ref. 4.

12. S. Orihara, R. Knoshita, T. Yanase, M. Segawa, S. Matsuyama, K. Yamagishi, J. Appl. Phys. 49, 1930 (1978).
13. J. L. Archer, Digest of '77 Intermag Conf.
14. A. J. Perneski, IEEE Trans. MAG-5, 554 (1969).
15. I. Danylchuk, J. Appl. Phys. 42, 1358 (1971).
16. F. Parzefall, B. Littwin, and W. Metzdorf, IEEE Trans. MAG-9, 293 (1973).
17. I. S. Gergis, P. K. George, and T. Kobayashi, IEEE Trans. MAG-12, 651 (1976).
18. D. C. Bullock, M. S. Shaikh, and F. G. West, Jr., IEEE Trans. MAG-12, 654 (1976).
19. R. Wolfe, J. C. North, W. A. Johnson, R. R. Spiwak, L. J. Varnerin, and R. F. Fischer, AIP Conf. Proc. 10, 339 (1973).
20. G. S. Almasi, E. A. Giess, R. J. Hendel, G. E. Keefe, Y. S. Lin, and M. Slusarczuk, AIP Conf. Proc. 24, 630 (1975).
21. A. H. Bobeck, I. Danylchuck, F. C. Rossol, and W. Strauss, IEEE Trans. MAG-9, 474 (1973).
22. J. W. Nielsen, IEEE Trans. MAG-12, 327 (1976).
23. A. H. Bobeck, E. G. Spencer, L. G. Van Uitert, S. C. Abrahams, R. L. Barns, W. H. Grodkiewicz, R. C. Sherwood, P. H. Schmidt, D. H. Smith, and E. M. Walters, Appl. Phys. Lett. 17, 131 (1970).
24. C. H. Bajorek, and R. J. Kobliska, IBM J. Res. and Develop. 20, 271 (1976).

25. P. Chaudhari, J. J. Coumo, and R. J. Gambino, IBM J. Res. and Develop. 17, 66 (1973).

26. C. T. Chen, W. L. Wilson, Jr., and G. E. Roberts, J. Appl. Phys. 49, 1756 (1978).

27. M. H. Kryder, and H. L. Hu, AIP Conf. Proc. 18, 213 (1973).

28. D. Hafner, and F. B. Humphrey, Appl. Phys. Lett. 30, 303 (1977).

29. R. Carey, and E. D. Isaac, Magnetic Domains and Techniques for Their Observation, (Academic, New York, 1966).

30. P. J. Grundy, D. C. Hothersall, G. A. Jones, B. K. Middleton, and R. S. Tebble, Phys. Status Solidi A9, 79 (1972).

31. P. Chaudhari, and S. R. Herd, IBM J. Res. and Develop. 20, 102 (1976).

32. A. Rosencwaig, W. J. Tabor, and T. J. Nelson, Phys. Rev. Lett. 29, 946 (1972).

33. G. P. Vella-Coleiro, A. Rosencwaig, and W. J. Tabor, Phys. Rev. Lett. 29, 949 (1972).

34. A. P. Malozemoff, and J. C. Slonczewski, Phys. Rev. Lett. 29, 952 (1972).

35. T. M. Morris, G. J. Zimmer, and F. B. Humphrey, J. Appl. Phys. 47, 721 (1976).

36. W. J. Tabor, A. H. Bobeck, G. P. Vella-Coleiro, and A. Rosencwaig, Bell Syst. Tech. J. 51, 1427 (1972).

37. Kochan Ju, and F. B. Humphrey, IEEE Trans. MAG-13, 1190 (1977).

38. B. A. Calhoun, E. A. Giess, and L. L. Rosier, Appl. Phys. Lett.

18, 287 (1971).

39. H. Callen, R. M. Josephs, J. A. Seitchik, and B. F. Stein, Appl. Phys. Lett. 21, 366 (1972).

40. G. P. Vella-Coleiro, F. B. Hagedorn, Y. S. Chen, and S. L. Blank, Appl. Phys. Lett. 22, 324 (1973).

41. B. E. Argyle, J. C. Slonczewski, and A. E. Mayadas, AIP Conf. Proc. 5, 175 (1972).

42. G. P. Vella-Coleiro, AIP Conf. Proc. 18, 217 (1973).

43. F. B. Hagedorn, AIP Conf. Proc. 18, 222 (1973).

44. Kochan Ju, and F. B. Humphrey, J. Appl. Phys. 48, 4656 (1977).

45. A. A. Thiele, J. Appl. Phys. 45, 377 (1974).

Chapter 2

Theory of Domain Wall Motion in Magnetic Bubble Materials

The dynamic behavior of the magnetic moment per unit volume $\overline{M}$ is described in terms of gyroscopic precession by a phenomenological model proposed by Landau and Lifschitz [1]. In this approach [1,2], the magnetization is treated as a continuous function of space and time. Its magnitude M_s is constant, and its direction is specified by the angles θ and ϕ shown in Fig. (2.i.1). Associated with the magnetization is an underlying angular momentum per unit volume $\overline{L}$, which is constant in magnitude and directed opposite to $\overline{M}$, so that $\overline{L} = -\overline{M}/\gamma$. The value of the gyromagnetic ratio γ that is predicted by quantum mechanics is $g|e|/2mc$. The Landé g-factor g [3] describes the relative contributions to the magnetic moment from orbital motion and from electron spin. In ferromagnetic materials, the moment is due primarily to electron spin, so that g is about two, and γ is approximately 1.7×10^7 $Oe^{-1}sec^{-1}$. In the presence of an effective magnetic field $\overline{H}_e$, the angular momentum precesses according to $\dot{\overline{L}} = \overline{M} \times \overline{H}_e$. In order to account for relaxation in magnetic materials, it is necessary to include a small torque that tends to align the magnetization with the effective field. Landau and Lifschitz proposed a torque of the form, $\overline{M} \times (\overline{M} \times \overline{H}_e)$. Later, Gilbert [4] proposed an alternative form, $\alpha/M_s \cdot (\overline{M} \times \dot{\overline{M}})$, which is analogous to viscous damping. These two forms are equivalent in the limit of small

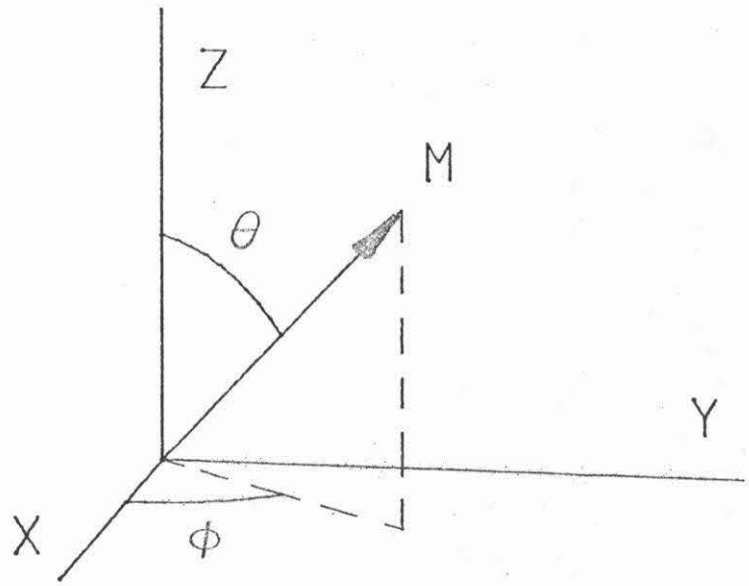

Fig. 2.i.1. The Spherical-Polar Coordinate System Used to Describe the Orientation of $\bar{M}$. A Cartesian coordinate system (x,y,z) is used to describe position within the magnetic material.

damping. By combining these results, the dynamic behavior of the magnetization is described by

$$\dot{\bar{M}} = -\gamma \bar{M} \times \bar{H}_e + \frac{\alpha}{M_s}(\bar{M} \times \dot{\bar{M}}) \quad . \tag{2.i.1}$$

This equation, known as the Landau-Lifschitz-Gilbert equation (LLG), is the theoretical basis for the analysis of dynamic ferromagnetism.

Wall motion will be analyzed by using the Lagrangian formulation of classical mechanics for continuous systems [2,5]. In this formulation, the Lagrangian per unit volume L is the difference between the kinetic energy per unit volume w and the potential energy per unit volume ρ_E. In general, L depends on the local orientation of $\bar{M}$, its gradients, and on position. Dissipation is described by a Rayleigh function per unit volume F. By applying Hamilton's variational principle,

$$\delta \int dt \iiint_V d^3r \; L(\theta, \phi, \nabla\theta, \nabla\phi, \dot{\phi}, \dot{\theta}, \bar{r}) = 0 \quad , \tag{2.i.2}$$

and by using well-known techniques from the calculus of variations [4,6], the Euler equations and boundary conditions are obtained:

$$\frac{d}{dt}\left(\frac{\partial L}{\partial q_j}\right) + \sum_{i=1}^{3} \frac{d}{dx_i}\left(\frac{\partial L}{\partial \frac{\partial q_j}{\partial x_i}}\right) - \frac{\partial L}{\partial q_j} + \frac{\partial F}{\partial q_j} = 0 \quad , \tag{2.i.3a}$$

$$\delta q_j \Big|_S = 0 \quad , \tag{2.i.3b}$$

$$\text{or} \qquad \frac{\partial L}{\partial \left(\frac{\partial q_j}{\partial x_i}\right)} = 0 \quad , \tag{2.i.3c}$$

where $(q_1,q_2) = (\theta,\phi)$, and $(x_1,x_2,x_3) = (x,y,z)$. Given specific forms for L and F, the Euler equations may be solved for the time and spatial dependence of θ and ϕ.

The functional forms of L and F are determined from the LLG equation. One expression for the kinetic energy density that is consistent with gyroscopic precession is

$$w = \frac{-M_s}{\gamma} \dot{\phi} \cos\theta \quad . \tag{2.i.4a}$$

This is the kinetic energy of a classical top in which only the principal moment of inertia parallel to the angular momentum is nonzero. This expression has an unusual form, in that it assigns a special role to the direction of the z-axis. Hence, the functional form of w is not unique, but depends on the choice of coordinate axes. For example, another equivalent form is

$$w = \frac{-M_s}{\gamma} \dot{\theta}\phi \sin\theta \tag{2.i.4b}$$

However, all of these forms differ by an exact time derivative of some function of the coordinates, in this case $\frac{M_s}{\gamma} \phi \cos\theta$, so that all preference for coordinate systems is lost in the equations of motion. The Lagrangian is given by $w - \rho_E$, where ρ_E is the potential energy associated with reversible torques. The Rayleigh function per unit volume that is consistent with the Gilbert damping torque is

$$F = \frac{\alpha M_s}{2\gamma} (\dot{\theta}^2 + \sin^2\theta \, \dot{\phi}^2) \quad . \tag{2.i.5}$$

Physically, $2F$ represents the rate at which the magnetic system loses energy in the form of heat (per unit volume).

Contributions to the potential energy come from four sources: anisotropy, exchange, external magnetic fields, and magnetic dipole interactions. The magnetic moments interact with the underlying material, so that the energy depends on orientation. In uniaxial materials, the anisotropy energy is given by

$$K_u \sin^2\theta \quad , \tag{2.i.6a}$$

where the easy axis has been taken as the z-axis. In ferromagnets, there is a strong torque, which tends to align $\overline{M}$ with its nearest neighbors. This torque, which comes from the quantum-mechanical exchange interaction, is represented here by the exchange energy density,

$$A\,[\nabla\theta \cdot \nabla\theta + \sin^2\theta\ \nabla\phi \cdot \nabla\phi\ ] \quad . \tag{2.i.6b}$$

The energy due to the external field $\overline{H}$ is just

$$-\overline{M} \cdot \overline{H} \quad . \tag{2.i.6c}$$

The energy due to long range dipole-dipole interactions is given in terms of the magnetic charge density, $\nabla \cdot \overline{M}$, as

$$\frac{1}{2}\nabla \cdot \overline{M}(r) \iiint_V d^3r' \frac{\nabla' \cdot \overline{M}(\overline{r}')}{|\overline{r}-\overline{r}'|} \quad . \tag{2.i.6d}$$

This is often written in terms of a demagnetizing field $\overline{H}_d$:

$$-\frac{1}{2}\overline{M} \cdot \overline{H}_d \quad . \tag{2.i.6e}$$

In general, $\overline{H}_d$ depends on the orientation of $\overline{M}$ throughout the material, but in some simple situations, it is only a function of the local orientation of $\overline{M}$. The sum of these contributions,

$$\rho_E = K_u \sin^2\theta + A[(\nabla\theta)^2 + \sin^2\theta\ (\nabla\phi)^2] - \overline{M}\cdot\overline{H} - \frac{1}{2}\overline{M}\cdot\overline{H}_d \quad , \qquad (2.i.7)$$

is the potential energy function used in the Lagrangian.

The purpose here is to develop a model of domain wall motion in magnetic bubble materials. Motion in these thin-film materials is complicated by the presence of demagnetizing fields from $\nabla\cdot\overline{M}$ at the film surfaces. These fields produce static and dynamic wall twist structures which vary through the film thickness. However, in high-Q materials, where the wall thickness is much smaller than the film thickness, the structure changes slowly, so that each point in the wall may be thought of as having a locally uniform wall structure. Furthermore, since the demagnetizing fields are roughly independent of the internal wall structure in this limit, they may be treated as constant in-plane fields. The development begins in Sec. 2.1 by considering the dynamic properties of a domain wall with a uniform, i.e., one-dimensional structure. In Sec. 2.2, the analysis is extended to motion of one-dimensional walls in the presence of in-plane fields. These results are used in Sec. 2.3 to develop equations of motion for domain walls in magnetic bubble materials. An approximate analysis shows that internal twist structures, called horizontal Bloch lines, are formed as a result of the surface fields. The dynamic properties of these structures are investigated in some detail by using the horizontal Bloch line model, and it is shown that they have a significant effect on wall motion. Finally, wall motion is treated more rigorously in Sec. 2.4 by solving the equations of motion numerically.

These results are used in Ch. 3 to show that the unusual wall behavior found during wall oscillation is due to the presence of horizontal Bloch lines.

Section 2.1 Motion of One-Dimensional Wall Structures

Consider the case of an isolated domain wall parallel to the xz-plane in an infinite, uniaxial magnetic material. The properties of the wall are independent of both x and z, so that $\overline{M}$ only depends on one coordinate, y. This situation is somewhat artificial [11] in that the boundary conditions on $\overline{M}$ which produce the wall structure are established by the surrounding domains. It is assumed here that domains are present, but that the material boundaries are far away, so that interactions with $\nabla\cdot\overline{M}$ at these surfaces may be neglected. Such interactions are considered in Sec. 2.3.

In this situation, the Lagrangian has a relatively simple form. The gradients of θ and ϕ only have one nonzero component each, θ_y and ϕ_y, so that the exchange energy has two terms. Subscripts on the functions ϕ and θ represent spatial derivatives, e.g., $\phi_y=\partial\phi/\partial y$. There is only one term in $\nabla\cdot\overline{M}$, $\frac{\partial M_y}{\partial y}$, so that $\overline{H}_d$ has only a y-component, which is proportional to M_y. From Eq. (2.i.6e), the demagnetizing energy is given by

$$2\pi M_s^2 \sin^2\theta \sin^2\phi \ . \qquad (2.1.1)$$

In the case considered here, there are no external in-plane fields, so

that $\bar{H}$ has only one component, H_z. By combining these results with Eqs. (2.i.4a) and (2.i.7), the Lagrangian is given by

$$L = -\frac{M_s}{\gamma}\dot{\phi}\cos\theta - K_u \sin^2\theta - A(\theta_y^2 + \sin^2\theta\,\phi_y^2)$$

$$+ M_s H_z \cos\theta - 2\pi M_s^2 \sin^2\theta \sin^2\phi \quad . \qquad (2.1.2)$$

Far from the wall, $\bar{M}$ aligns with the easy axis, so that $\theta \to 0$ as $y \to -\infty$, and $\theta \to \pi$ as $y \to +\infty$. With these conditions, $\theta(y)$ meets the first boundary condition, Eq. (2.i.3b). Since L does not depend on ϕ_y in this region, ϕ meets the second boundary condition, Eq. (2.i.3c).

Static Wall Structure

The static wall structure may be determined by substituting the explicit form for L into the Euler equations. In a static wall, $\dot{\theta}$ and $\dot{\phi}$ are zero, so that the first and last terms in Eq. (2.i.3a) are zero. The kinetic energy term in L is zero, so that Hamilton's principle is equivalent to minimizing the potential energy. For the wall to be stationary, H_z must be zero. By substituting Eq. (2.1.2) into Eq. (2.i.3a), two coupled, nonlinear differential equations are obtained:

$$K_u \sin 2\theta - 2A\theta_{yy} + 2A \sin 2\theta \phi_y^2 + 2\pi M_s^2 \sin 2\theta \sin^2\phi = 0 \quad , \qquad (2.1.3a)$$

and

$$-2A \sin 2\theta\, \theta_y \phi_y + 2\pi M_s^2 \sin^2\theta \sin 2\phi - 2A \sin^2\theta \phi_{yy} = 0 \quad . \qquad (2.1.3b)$$

The solutions of these equations, $\theta(y)$ and $\phi(y)$, describe the spatial dependence of $\overline{M}$ in a static one-dimensional wall.

The wall structure is determined by assuming a simple form for $\phi(y)$ and then showing that this assumption leads to an exact solution of the differential equations. If $\phi(y) = \phi$ is a constant, then Eqs. (2.1.3a-b) reduce to

$$(K_u + 2\pi M_s^2 \sin^2\phi) \sin 2\theta - 2A\theta_{yy} = 0 \quad , \tag{2.1.4a}$$

and

$$2\pi M_s^2 \sin^2\theta \sin 2\phi = 0 \quad . \tag{2.1.4b}$$

The second equation is satisfied at each point in the wall when ϕ is an integer multiple of $\pi/2$. Bloch wall solutions [1] are obtained by setting ϕ equal to zero or π. Equation (2.1.4a) may be integrated to give the wall shape.

$$\theta(y) = 2 \arctan \left(\exp \left(\frac{y}{\Delta_B}\right)\right) \quad , \tag{2.1.5}$$

where $\Delta_B = \sqrt{A/K_u}$ characterizes the width of the domain wall. This functional form has the useful property:

$$\theta_y = \frac{\sin\theta}{\Delta_B} \quad . \tag{2.1.6}$$

Since ρ_E is translationally invariant, the location of the wall center is undetermined and has been taken as zero. Neél wall solutions [7] are obtained by making ϕ either $+\frac{\pi}{2}$ or $-\frac{\pi}{2}$. The wall shape is exactly

the same, but the wall width parameter Δ_B is replaced by

$$\Delta_N = \frac{\Delta_B}{\sqrt{1 + Q^{-1}}} \tag{2.1.7}$$

These results were obtained by assuming that the material surfaces do not affect the wall structure. With this assumption, the Bloch and Neél wall structures do not depend on film thickness. Static wall structures in real, thin-film materials are considered in Sec. 2.3. There, it is shown that near the surfaces the wall has a Neél structure, while in the film center it has a Bloch structure.

The Bloch and Neél wall shapes $\theta(y)$ are shown in Fig. (2.1.1). In both cases, changes in θ are confined within a few Δ_B of the wall center. The Bloch wall solution represents an energy compromise between anisotropy, which tends to compress the wall, and exchange, which tends to expand it. In the Neél wall solution, there is an additional energy term due to $\nabla\cdot\bar{M}$ within the wall. It can be seen from the functional form, Eq. (2.1.5), that $\nabla\cdot\bar{M}$ takes the approximate form of two charged sheets with opposite sign separated by a distance, Δ_B. These charges attract each other, and tend to compress the wall. Therefore, the Neél wall width is always somewhat smaller than the Bloch wall width. A relatively small value, $Q = 2$, has been used in this figure to emphasize this difference. The wall width parameter in bubble materials is typically less than 0.1 μm, so that the wall width is usually much smaller than the film thickness.

Since the energies of the Bloch and Neél walls are different,

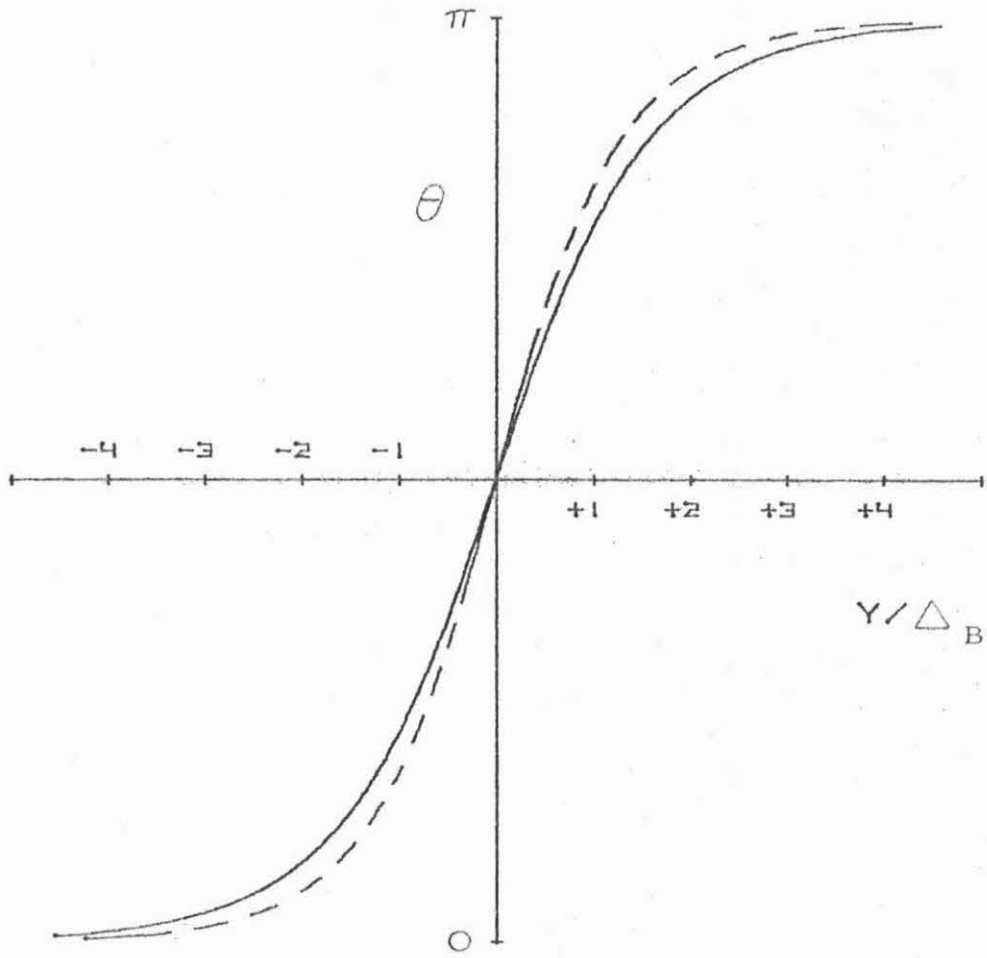

Fig. 2.1.1. The Polar Angle θ as a Function of Position (y/Δ_B) Through the Wall Thickness. Bloch and Neél wall structures are shown as solid and dashed curves, respectively. In calculating the Neél wall structure, the value Q = 2 was used.

they cannot both represent energy minima. The wall energy is obtained by integrating ρ_E through the wall thickness, and by making use of Eq. (2.1.6). The Bloch wall energy σ_B and Neél wall energy σ_N obtained in this way are

$$\sigma_B = 4\sqrt{AK_u} \quad , \tag{2.1.8a}$$

and

$$\sigma_N = \sigma_B \sqrt{1 + Q^{-1}} \quad . \tag{2.1.8b}$$

Clearly, the function $\theta(y)$ represents a local energy minimum in both cases, since perturbations can be found in which all three terms in ρ_E are simultaneously increased. Hence, the orientations, $\phi=\pm\frac{\pi}{2}$, represent a local energy maximum, and the Neél wall represents a saddle point solution. It is the Bloch wall solution that represents the static, one-dimensional wall structure. Note that there are two physically distinct Bloch wall structures, corresponding to the orientations, $\phi=0,\pi$. These structures are said to have opposite senses of wall chirality. It will be shown that this dual chirality is preserved even in the more complicated structures found in thin-film materials. Neél walls also have two distinct chiralities, corresponding to $\phi=\pm\pi/2$.

Walker Model

Equations of motion for a one-dimensional wall structure are obtained by assuming that θ and ϕ only depend on y and t. By substitut-

ing the Lagrangian, Eq. (2.1.2) and dissipation function, Eq. (2.i.5) into the Euler equation, Eq. (2.i.3a), the following equations of motion are obtained:

$$-2A\theta_{yy} - \frac{M_s}{\gamma}\sin\theta\dot{\phi} + K_u\sin 2\theta + M_s H_z \sin\theta + A\phi_y^2\sin 2\theta$$

$$+ 2\pi M_s^2 \sin 2\theta \sin^2\phi - \frac{\alpha M_s}{\gamma}\dot{\theta} = 0 \quad , \tag{2.1.9a}$$

and

$$\frac{M_s}{\gamma}\sin\theta\dot{\theta} - 2A\theta_y\phi_y\sin 2\theta - 2A\phi_{yy}\sin^2\theta$$

$$+ 2\pi M_s^2 \sin^2\theta \sin 2\phi - \frac{\alpha M_s}{\gamma}\sin^2\theta\dot{\phi} = 0 \quad . \tag{2.1.9b}$$

The solutions of these nonlinear, partial differential equations, $\theta(y,t)$ and $\phi(y,t)$, specify the dynamic behavior of the one-dimensional wall structure.

Solutions to these equations of motion [8-10] are obtained by assuming that a moving wall has the same structure as a stationary wall. Assume that $\theta(y)$ maintains the functional form,

$$\theta(y,t) = 2\arctan(\exp(s)) \quad , \tag{2.1.10}$$

where $s = \frac{y-q(t)}{\Delta(t)}$.

Here, the wall position q and the wall width parameter Δ are functions of time. It is also assumed that ϕ is only a function of time. This

structure may be substituted into Eqs. (2.1.9a-b) by making use of the following:

$$\dot{\theta} = \sin\theta \dot{s} \quad , \tag{2.1.11a}$$

$$\theta_{yy} = \frac{\sin 2\theta}{2\Delta^2} \quad , \tag{2.1.11b}$$

and

$$\dot{s} = \frac{-(y-q)}{\Delta}\left(\frac{\dot{\Delta}}{\Delta}\right) - \frac{\dot{q}}{\Delta} \quad . \tag{2.1.11c}$$

A consistent solution is obtained by separately equating to zero the coefficients of sin (2θ), and $\sin\theta$ in Eq. (2.1.9a), and $\sin^2\theta$ in Eq. (2.1.9b). The three equations which result are

$$\frac{-2A}{\Delta^2} + 2K_u + 4\pi M_s^2 \sin^2\phi = 0 \quad , \tag{2.1.12a}$$

$$\frac{-M_s}{\gamma}\dot{\phi} + M_s H_z + \frac{\alpha M_s}{\gamma}\dot{\phi} = 0 \quad , \tag{2.1.12b}$$

and

$$\frac{M_s}{\gamma}\dot{s} + 2\pi M_s^2 \sin 2\phi + \frac{\alpha M_s}{\gamma}\dot{\phi} = 0 \quad . \tag{2.1.12c}$$

Assume that changes in wall width are relatively small and slow, so that contributions to $\dot{s}$ from $\dot{\Delta}$ may be neglected in comparison with contributions from $\dot{q}$ [see Eq. (2.1.11c)]. This assumption is most appropriate in high-Q materials, and in cases where H_z is small, so that ϕ changes slowly. In this limit, wall width changes are quasistatic, and

make no contribution to the kinetic energy density. With this assumption, Eqs. (2.1.12a-c) reduce to

$$\dot{q} = \gamma\Delta f(\phi) + \alpha\Delta\dot{\phi} \quad , \tag{2.1.13a}$$

and

$$\dot{\phi} = \gamma H_z - \frac{\alpha\dot{q}}{\Delta} \quad , \tag{2.1.13b}$$

where

$$\Delta = \frac{\Delta_B}{\sqrt{1 + \frac{\sin^2\phi}{Q}}} \quad , \tag{2.1.13c}$$

and

$$f(\phi) = 2\pi M_s \sin 2\phi \quad . \tag{2.1.13d}$$

In the limit of small damping, $\dot{\phi}$ is governed by the external field, while the wall velocity is determined by the size of M_s and the value of ϕ. When ϕ is zero or π, the wall has a Bloch structure, and $\Delta = \Delta_B$, while for $\phi = \pm\frac{\pi}{2}$, $\Delta = \Delta_N$, and the wall has a Neél structure. In cases where $\dot{\Delta}$ is zero, i.e., when $\dot{\phi}$ is zero or in the limit, $Q \to \infty$, the structure assumed here leads to an exact solution of the equations of motion. Recent numerical solutions of the full equations [10] indicate that the static wall shape and uniform ϕ angle are preserved even in more complicated situations. In general, solutions of Eqs. (2.1.13a-d) only represent approximate solutions of the original equations of motion.

The motion described by Eqs. (2.1.13a-d) may be divided into two distinct types: steady-state motion, and oscillatory motion. In steady-state motion, $\dot{\phi}$ is zero, and $\dot{q} = v$ is a constant. Under these conditions, the left side of Eq. (2.1.13b) is zero, or

$$v = \mu H_z \quad , \tag{2.1.14a}$$

where

$$\mu = \frac{\gamma\Delta}{\alpha} \quad . \tag{2.1.14b}$$

The steady-state velocity is proportional to H_z, and the mobility μ is inversely proportional to α. The steady-state orientation of ϕ is obtained from Eqs. (2.1.14a) and (2.1.13a). Conversely, for each orientation of ϕ, there is a corresponding steady-state velocity:

$$v = \gamma\Delta(\phi) \cdot 2\pi M_s \sin 2\phi \quad . \tag{2.1.15}$$

This relationship is shown in Fig. (2.1.2). Because the wall width contraction in Eq. (2.1.13c) is small in high-Q materials, it has been neglected in this figure. The velocity increases as ϕ increases from the static orientation $\phi_o = 0$. The maximum steady-state velocity, which occurs at $\phi = \frac{\pi}{2}$, is called the Walker velocity:

$$v_w = \frac{\gamma\Delta_B \cdot 2\pi M_s}{\sqrt{1 + \frac{1}{2Q}}} \quad . \tag{2.1.16}$$

For $\phi<0$, the velocity is negative, and reaches a minimum velocity

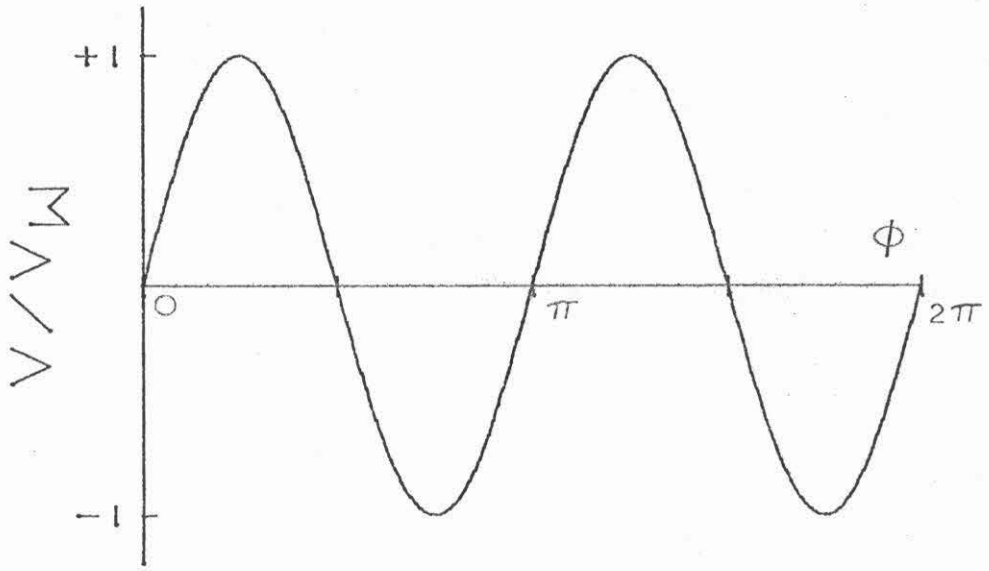

Fig. 2.1.2. Steady-State Velocity v/v_w as a Function of ϕ.

$-v_w$ at $\phi = \frac{-\pi}{4}$. The same behavior can be seen for the other wall chirality, which has a static orientation, $\phi_o = \pi$.

Oscillatory motion occurs if H_z exceeds a certain critical value. The balance between H_z and the damping term in Eq. (2.1.13b) required for steady-state motion is only possible if H_z is less than the Walker field:

$$H_w = \frac{v_w}{\mu} = 2\pi M_s \quad \alpha \quad . \tag{2.1.17}$$

If H_z is greater than H_w, $\dot{\phi}$ is greater than zero, and ϕ increases with time. In the limit, $\alpha \to 0$, ϕ increases at a constant rate, and $\dot{q}$ follows the curve shown in Fig. (2.1.2). In the regions $0<\phi<\pi/2$ and $\pi<\phi<\frac{3\pi}{2}$, the wall travels forward, while for $\frac{\pi}{2}<\phi<\pi$ and $\frac{3\pi}{2}<\phi<2\pi$, the wall travels backward by an equal amount, so that the wall oscillates back and forth with no change in average position. For nonzero damping, the damping term in Eq. (2.1.13b) decreases $\dot{\phi}$ when $\dot{q}$ is positive and increases $\dot{\phi}$ when $\dot{q}$ is negative, so that the wall spends slightly more time moving forward. The wall still alternates between forward and reverse motion, but there is a small average forward velocity. Walker has shown [10] that this average velocity decreases with increasing H_z. The reason for this is that when H_z is large, the asymmetry in $\dot{\phi}$ caused by the damping terms becomes less significant, and the forward and reverse motion tend to cancel more completely. A more thorough treatment of oscillatory motion may be obtained by solving Eqs. (2.1.13a-d), numerically, but this is beyond the scope of the present discussion.

Section 2.2. Motion of One-Dimensional Wall Structures in the Presence in In-Plane Fields

The presence of a constant, homogeneous in-plane field $\overline{H}_{ip}$ significantly alters the analysis in two respects. First, the in-plane field changes the boundary conditions on ϕ. Far from the wall, there is no kinetic, exchange, or demagnetizing energy, so that the Lagrangian is just

$$L = -K_u \sin^2\theta + M_s H_z \cos\theta + M_s H_x \sin\theta \cos\phi$$

$$+ M_s H_y \sin\theta \sin\phi \quad . \tag{2.2.1}$$

The boundary conditions are determined by substituting this expression into the Euler equations. The solution of these equations, which are the asymptotic values of θ and ϕ , θ° and ϕ°,are given by

$$\theta^\circ = \frac{H_{ip}}{H_k + H_z} \quad , \tag{2.2.2a}$$

and

$$\tan\phi^\circ = H_y/H_x \quad , \tag{2.2.2b}$$

for $H_{ip} << H_k$. Here , H_k is the effective anisotropy field, $2K_u/M_s$. It will sometimes be convenient to scale in-plane fields to H_k. Such scaled fields are indicated by lower case letters, e.g., $H_x/H_k = h_x$. The in-plane field tilts $\overline{M}$ slightly away from the easy

axis, but, more important, the projection of $\bar{M}$ in the xy-plane aligns with the in-plane field. Second, the Lagrangian is complicated by two additional energy terms. By making use of the alternate form for the kinetic energy, Eq. (2.i.4b), the Lagrangian may be written as

$$L = \frac{-M_s}{\gamma}\dot{\phi}\sin\theta\dot{\theta} - K_u \sin^2\theta - A[\theta_y^2 + \sin^2\theta\,\phi_y^2]$$
$$+ M_s H_z \cos\theta + M_s H_x \sin\theta\cos\phi + M_s H_y \sin\theta\sin\phi$$
$$+ 2\pi M_s^2 \sin^2\theta\sin^2\phi + \rho_E^o \quad , \tag{2.2.3}$$

where ρ_E^o is the constant background energy density far from the wall,

$$\rho_E^o = K_u\sin^2\theta^o + M_s H_z\cos\theta^o + 2\pi M_s^2 \sin^2\theta^o\sin^2\phi^o$$
$$- M_s H_x \sin\theta^o\cos\phi^o - M_s H_y \sin\theta^o\sin\phi^o \quad . \tag{2.2.4}$$

Equations of motion for the wall may be obtained by substiting this expression into the Euler equation. Approximate solutions are again obtained by constraining the wall to a particular dynamic structure.

Static Wall Structure

Different structures have been used in the past to approximate the static wall structure in the presence of in-plane fields. In all cases, the function $\theta(y)$ is not strongly influenced by the in-plane field, because it is determined mainly by much larger exchange and anisotropy energy terms. However, since $\phi(y)$ is determined by in-

plane field and demagnetizing energies, which may be comparable in size, it can be significantly affected by the in-plane field. For the special case in which $\overline{H}_{ip}$ is parallel to the wall (H_x only), these energy terms are simultaneously minimized by taking $\phi(y)$ to be zero. For other orientations of $\overline{H}_{ip}$, the situation is more complicated, and the structure is approximated by making certain assumptions about $\overline{M}(y)$. In Bloch-type walls [13,14], demagnetizing energy is avoided by making M_y constant, so that $\nabla \cdot \overline{M}$ is zero everywhere. The constant value of M_y is determined from the boundary conditions, Eqs. (2.2.2a-b). This structure is most suitable when H_{ip} is small compared to $4\pi M_s$, since it then avoids the more significant energy term; however, when H_{ip} and $4\pi M_s$ are comparable in size, it gives poor results because $\overline{M}$ is always misaligned with the in-plane field near the wall center. In Neél-type walls [14], $\phi = \phi^o$ is a constant, which is determined from Eq. (2.2.2b). This structure is most suitable when H_{ip} is large, because it aligns $\overline{M}$ with $\overline{H}_{ip}$ as much as possible. However, when H_{ip} is small this structure overestimates the demagnetizing energy. Neither type of structure gives adequate results over the entire range of in-plane fields considered here.

The problem with these assumptions is that the structure near the wall center is determined by conditions far from the wall. Solutions must meet the proper boundary conditions, so that the parameters which characterize the entire structure, either M_y or ϕ^o, are determined by the in-plane field. It seems clear that a better solution would be one in which the structure near the wall is determined by both the

in-plane field and demagnetizing energies. Hubert [15] has proposed more general one-dimensional structures in which this is accomplished indirectly, but the conceptual complexity of these structures make them unsuitable for use in modeling dynamic properties.

A relatively simple structure, which takes into account both the in-plane field and demagnetizing energies, is shown schematically in Figs. (2.2.1). It is assumed that inside the wall, $\theta(y)$ has the conventional Bloch wall form, Eq. (2.1.5), with an adjustable wall width parameter Δ. When θ reaches the asymptotic value given by Eq. (2.2.2a), it remains constant (solid line) rather than continuing with the Bloch wall form (dotted line). The function $\phi(y)$ shown in Fig. (2.2.1b) has an adjustable, constant value in the vicinity of the wall ϕ^i. At the point where θ reaches θ^o, $\phi(y)$ begins a linear transition to the asymptotic value ϕ^o given in Eq. (2.2.2b). The width of this transition region b is also adjustable. Note that in the limit, $H_{ip} \to 0$, this model structure reduces to the Bloch wall structure.

The static wall structure is determined by calculating the Lagrangian based on this model structure. The Lagrangian per unit wall area L_a is obtained by integrating L in Eq. (2.2.3) through the wall thickness. The result to first order in h_{ip} is

$$\begin{aligned} L_a = {} & \frac{2M_s}{\gamma}\,\phi^i\,\dot{q} - 2K_u\Delta - \frac{2A}{\Delta} + 2M_s H_z\, q \\ & + \pi H_x M_s \Delta \cos\phi^i + \pi H_y M_s \Delta \sin\phi^i \\ & - 4\pi M_s^2 \Delta \sin^2\phi^i \quad . \end{aligned} \tag{2.2.5}$$

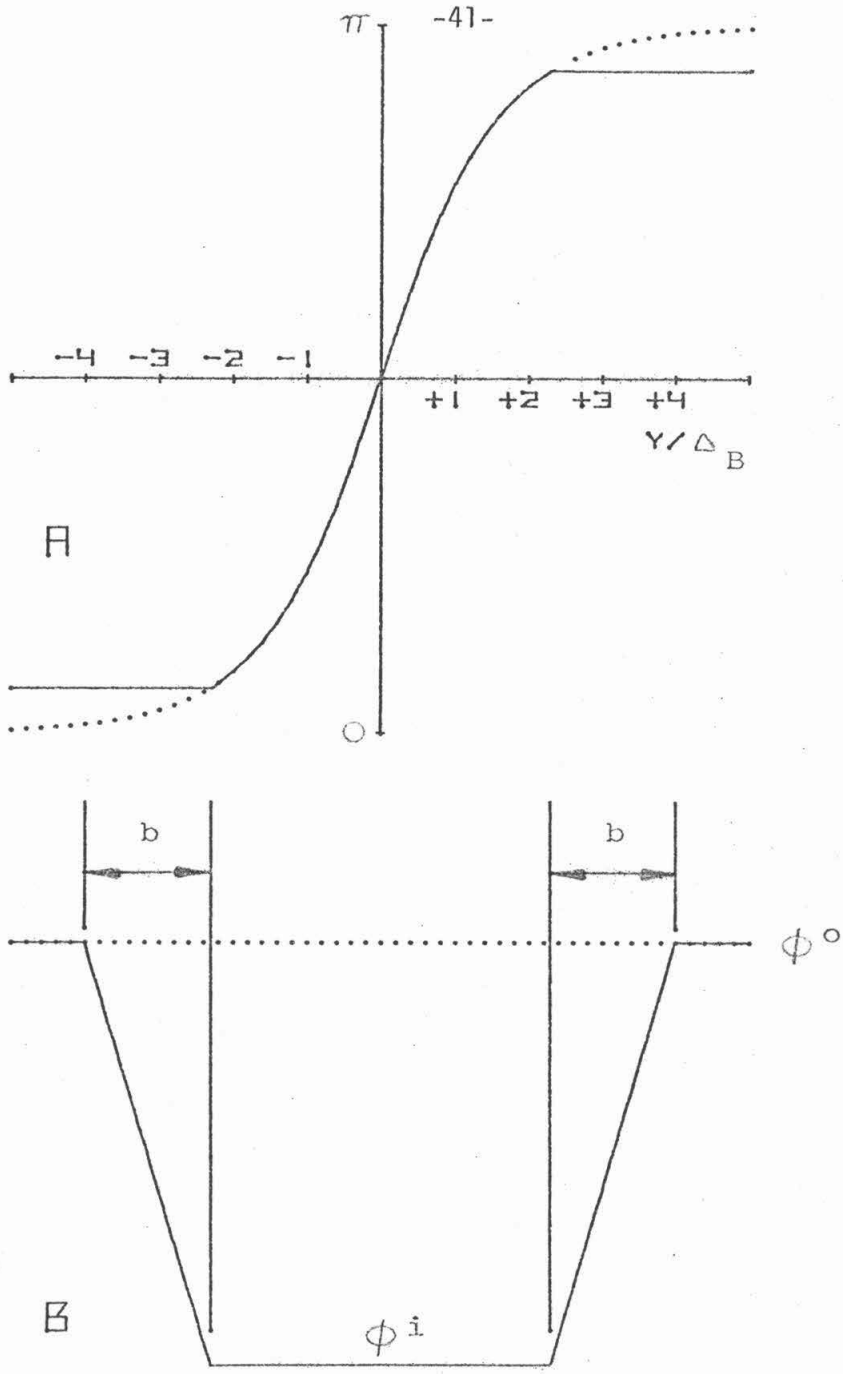

Fig. 2.2.1. Schematic Diagram of the Model Wall Structure in the Presence of In-plane Fields. Fig. (2.2.1a) shows B, the assumed structure for $\theta(y)$, and Fig. (2.2.1b) shows the structure for $\phi(y)$.

Note that the transition region from ϕ^i to ϕ^o makes no contribution to L_a in first order, so that L_a is only a function of three dynamical variables, q, ϕ^i, and Δ. In a stationary wall, $\dot{q}$ and H_z are zero, so that L_a only depends on ϕ^i and Δ. Treating these as dynamical variables, the Euler equations for the static structure are, from Eq. (2.i.3a),

$$H_x \sin\phi^i - H_y \cos\phi^i + 4M_s \sin 2\phi^i = 0 \quad , \tag{2.2.6a}$$

and

$$\Delta = \frac{\Delta_B}{\sqrt{1 - \pi h_x \cos\phi^i - \pi h_y \sin\phi^i + \frac{\sin^2\phi^i}{Q}}} \quad . \tag{2.2.6b}$$

The first equations give the static value of ϕ^i in terms of a compromise between the in-plane field and demagnetizing energies, as expected. The second equation indicates that the static wall width is decreased by demagnetizing effects, as in the Neél wall structure, and is increased by the in-plane field. The reason for this is that the in-plane field energy is lowered by tilting $\overline{M}$ away from the easy axis, toward $\overline{H}_{ip}$. This is accomplished here by widening the domain wall.

The static wall energy is calculated by integrating the energy density ρ_E through the wall thickness. Since only the energy due to the presence of the wall is of interest, the constant background energy ρ_E^o is subtracted from ρ_E. The result is

$$\sigma_w = \sigma_B \sqrt{1 - \pi h_x \cos\phi^i - \pi h_y \sin\phi^i + \frac{\sin^2\phi^i}{Q}} \quad , \qquad (2.2.7)$$

where the static orientation of ϕ^i is determined from Eq. (2.2.6a). Note that as H_{ip} tends to zero, the wall energy reduces to the Bloch wall energy.

Domain Wall Motion

Moving walls will be analyzed by assuming that the dynamic wall structure has the same form as the static structure. The Lagrangian per unit area is given in Eq. (2.2.5). The dissipation function per unit area L_a is obtained by integrating L from Eq. (2.i.5) through the wall thickness, and by making use of the assumed wall structure. The result, to first order in H_{ip}, is

$$F_a = \frac{\alpha \Delta M_s}{\gamma} \left[\left(\frac{\dot{q}}{\Delta} \right)^2 + \dot{\phi}^2 \right] . \qquad (2.2.8)$$

From now on, the superscript on ϕ^i will be omitted, and the value of $\phi(y)$ inside the wall will be designated by ϕ. By substituting the results of Eqs. (2.2.5) and (2.2.8) into Eq. (2.i.3a), and by treating q, ϕ, and Δ as dynamical variables, the following equations of motion are obtained [16],

$$\dot{q} = \gamma \Delta f(\phi) + \alpha \Delta \dot{\phi} \quad , \qquad (2.2.9a)$$

and

$$\dot{\phi} = \gamma H_z - \frac{\alpha \dot{q}}{\Delta} \quad , \qquad (2.2.9b)$$

where

$$\Delta = \frac{1}{\sqrt{1 - \pi h_x \cos\phi - \pi h_y \sin\phi + \frac{\sin^2\phi}{Q}}} \quad , \tag{2.2.9c}$$

and

$$f(\phi) = \frac{\pi}{2} H_x \sin\phi - \frac{\pi}{2} H_y \cos\phi + 2\pi M_s \sin 2\phi \quad . \tag{2.2.9d}$$

These equations are similar to those obtained in the Walker model, except that the in-plane field has a significant influence on dynamic behavior through the function $f(\phi)$. As before, the precession of ϕ is due mainly to the external field. The changes in wall width described by the third equation are the same as in a static wall [see Eq. (2.2.6b)].

The motion described by these equations may also be divided into steady-state and oscillatory motion. The steady-state velocity v is still given by Eq. (2.1.14a), but the wall width is changed slightly by the in-plane field according to Eq. (2.2.9c). The relationship between v and ϕ analogous to Eq. (2.1.15) is

$$v = \gamma\Delta[2\pi M_s \sin 2\phi + \frac{\pi}{2} H_x \sin\phi - \frac{\pi}{2} H_y \cos\phi] \quad . \tag{2.2.10}$$

The static orientation of ϕ, which satisfies $f(\phi_o) = 0$, may be changed by an in-plane field. For example, when H_y is positive, $\bar{M}$ tilts away from the plane of the wall, toward the in-plane field, and ϕ_o increases. However, with H_x only, ϕ is zero, and $\bar{M}$ is already aligned with the in-

plane field, so that no change occurs. Oscillatory motion results when μH_z exceeds the maximum steady-state velocity, i.e., the maximum value of v in Eq. (2.2.10). When this occurs, ϕ increases and $\dot{q}$ follows the steady-state velocity curve, as in the Walker model. However, since $v(\phi)$ may be strongly affected by in-plane fields, oscillatory motion is sensitive to these fields.

A more general energy conservation principle is obtained by calculating the Hamiltonian of a moving domain wall. The Hamiltonian per unit area is defined by [4]

$$\mathcal{H}_a = \sum_{i=1}^{3} p_i \dot{q}_i - L_a(q_i, \dot{q}_i, \bar{r}) \quad , \tag{2.2.11}$$

where $(q_1, q_2, q_3) = (q, \phi, \Delta)$. From Eq. (2.2.5), the momentum conjugate to q is $p_1 = \partial L_a / \partial \dot{q}_1 = \frac{2M_s}{\gamma}\phi$. All other momenta are zero. With this result, the Hamiltonian may be written as

$$\mathcal{H}_a = 2K_u\Delta + \frac{2A}{\Delta} - \pi H_x M_s \Delta \cos\phi - \pi H_y M_s \Delta \sin\phi$$

$$+ 4\pi M_s^2 \Delta \sin^2\phi - 2M_s H_z q \quad . \tag{2.2.12}$$

Since Δ is connected to ϕ through Eq. (2.2.9c), the Hamiltonian may also be written as

$$\mathcal{H}_a = \sigma_B \left[1 - \pi h_x \cos\phi - \pi h_y \sin\phi + \frac{\sin^2\phi}{Q}\right]^{1/2} - 2M_s H_z q \quad . \tag{2.2.13}$$

This is immediately recognized as the sum of the kinetic energy of the domain wall, and the potential energy due to wall position. Since L_a does not depend on time explicitly, the Hamiltonian is a constant of the motion.

The steady-state and oscillatory motion found both here and in the Walker model may be viewed as a consequence of energy conservation. The power dissipated per unit wall area is from Eq. (2.2.8),

$$2F_a = \frac{2\alpha\Delta M_s}{\gamma}\left[\left(\frac{\dot{q}}{\Delta}\right)^2 + \dot{\phi}^2\right] \quad . \tag{2.2.14}$$

In steady-state motion, the kinetic energy is constant, because $\dot{\phi}$ is zero, so that the input power from the external field, $2M_sH_z\dot{q}$, must be dissipated by viscous damping. By equating these two expressions, the steady-state velocity is μH_z, as before. If μH_z exceeds the maximum possible steady-state velocity, then some power is left over and must be stored as kinetic energy. However, the kinetic energy has a maximum value, which occurs when ϕ reaches $\frac{\pi}{2}$ in the Walker model. When ϕ rotates beyond this value, the kinetic energy decreases, and the wall returns energy to the external field by moving backwards. Oscillatory motion may be seen as a consequence of energy alternating between kinetic and potential forms in such a way that the total, $\mathcal{H}_a$, is constant. Because α is not actually zero, some energy is dissipated, resulting in a small, net forward velocity.

Harmonic Oscillator Model

Wall motion may be approximated as simple harmonic motion in the limit of small deviations from static conditions. It has long been recognized [18-20] that walls possess inertial properties, which may be described in terms of an effective mass per unit wall area. This effective mass is determined by expanding the kinetic energy in Eq. (2.2.13) in powers of the velocity. The energy is first expanded in powers of ϕ, and then ϕ is related to v through Eq. (2.2.9a). The result to second order in v is

$$\sigma_{K.E.} = \sigma_B + \frac{1}{2}\left[\frac{2M_s}{\gamma^2 \Delta_B f_o'}\right] v^2 + \text{Order } (v^3) \quad , \tag{2.2.15}$$

where $f_o' = \left.\frac{\partial f}{\partial \phi}\right|_{\phi=\phi_o}$.

The term in brackets is just the effective wall mass:

$$m = \frac{2M_s}{\gamma^2 \Delta_B f_o'} \quad . \tag{2.2.16}$$

In the absence of in-plane fields, this expression reduces to the classical Döring mass [18]:

$$m_D = \frac{1}{2\pi\gamma^2 \Delta_B} \quad . \tag{2.2.17}$$

The restoring force acting on the wall is provided by the surrounding domains. Assume that H_z can be approximated by $H_z = H_a\, u(t) + H' q(t)$. The first term represents the uniform time dependence of H_z through the

function u(t), while the second term represents the restoring force. The effective field gradient H' comes from the surrounding domains, and is calculated for bubble and stripe domains in Appendix A. In general, H' depends somewhat on the domain configuration. The gradient is typically only a few tenths of an oersted per wall width, so that it may be neglected when calculating the wall structure.

The harmonic oscillator model is obtained by expanding Eqs. (2.2.9a-d) around ϕ_o in the limit of small damping. The linear equations which result may be written as a single harmonic oscillator equation for the wall position:

$$\frac{\ddot{q}}{\gamma^2 \Delta_B f_o'} + \frac{\dot{q}}{\gamma \Delta_B} - H'q = H_a\, u(t) \quad . \tag{2.2.18}$$

The coefficient of $\ddot{q}$, which is proportional to the wall mass density, is in agreement with Eq. (2.2.16). For stability, H' must be less than zero. The frequency of the wall oscillations described by Eq. (2.2.18) is given in the limit of small damping by

$$\nu = \frac{1}{2\pi}\sqrt{H'\gamma^2 \Delta_B f_o'} \quad . \tag{2.2.19}$$

The factor f_o' depends on $\bar{H}_{ip}$, so that the oscillation frequency can be significantly altered by an external in-plane field. In bubble materials, ν is typically a few megaHertz. The characteristic decay time of these oscillations is

$$\frac{2}{\alpha\gamma f_o'} \quad . \tag{2.2.20}$$

A typical decay time in bubble materials is about 20 nsec, but in the special low-loss sample investigated in Ch. 3, it is more than 300 nsec. In deriving this model, $f(\phi)$ was approximated by the first term in its Taylor series, $f_o' \cdot (\phi-\phi_o)$. As can be seen from Fig. (2.1.2), where $v = \gamma\Delta_B f(\phi)$ is shown as a function of ϕ, this approximation is only valid for small deviations from ϕ_o.

Section 2.3 Twisted Wall Motion in Thin-Film Materials

Wall motion in thin-film materials is complicated by interactions with $\nabla \cdot \bar{M}$ at the film surfaces. In Secs. 2.1 and 2.2, it was assumed that the material boundaries were far away, so that these interactions were neglected; however, in thin-film materials, these interactions must be taken into account. In the materials considered here, where Δ_B is much less than the film thickness h, the source configuration at the surface does not depend on the internal wall structure [21]. Therefore, the surface demagnetizing field may be treated as a constant magnetic field. This field has a large in-plane component perpenducular to the wall $H_s(z)$. As described earlier in Sec. 2.2, such in-plane fields tend to reorient ϕ toward the y-axis, normal to the wall. Since the field magnitude varies through the film thickness, the surface demagnetizing field produces a twisted wall structure, i.e., a structure in which ϕ varies with z. The purpose here is to develop

a model of twisted wall motion based on the model structure proposed in Sec. 2.2.

The surface demagnetizing field may be calculated for various domain configurations. It is assumed that H_s is constant across the wall width and is given by the value at the wall center. The perpendicular component of the surface demagnetizing field is given by an integral over the magneto-static charge density:

$$H_s(\bar{r}) = - \frac{\partial}{\partial y} \left[\iiint d^3r' \, \frac{\nabla' \cdot \bar{M}(\bar{r}')}{|\bar{r}-\bar{r}'|} \right] \quad . \tag{2.3.1}$$

This expression may be evaluated analytically in the limit, $\Delta_B \to 0$, for an isolated wall, and the result is [22]

$$H_s(z)\Big|_{y=0} = 4M_s \ell n \left(\frac{\frac{h}{2} + z}{\frac{h}{2} - z} \right) \tag{2.3.2}$$

For a parallel stripe array with zero bias field, the result is [22]

$$H_s(z)\Big|_{y=o} = 4M_s \ell n \left(\frac{\tanh\left(\frac{\pi}{2d}\left(\frac{h}{2} + z\right)\right)}{\tanh\left(\frac{\pi}{2d}\left(\frac{h}{2} - z\right)\right)} \right) \tag{2.3.3}$$

For bubble domains, H_s is given by

$$H_s(z)\Big|_{r=r_o} = 4M_s \left(D\left(\frac{\frac{h}{2} + z}{2r_o}\right) - D\left(\frac{\frac{h}{2} - z}{2r_o}\right) \right) \quad , \tag{2.3.4a}$$

where

$$D(\zeta) = \int_0^{\pi/2} d\theta \cos\theta \, \ell n \left(\frac{\sin\theta + (\sin^2\theta + \zeta^2)^{1/2}}{|\zeta|} \right) - \frac{\sin\theta}{(\sin^2\theta+\zeta^2)^{1/2}} \quad , \tag{2.3.4b}$$

and r_o is the bubble radius. In bubble domains, the surface field also has a z-component, which tends to bulge the wall. Wall bulging is discussed later. Note that all of these fields have unrealistic singularities at the film surfaces. This results from the assumption, $\Delta_B = 0$. A more rigorous approach would be to calculate the orientation of $\bar{M}$ near the film surface in detail. This would result in a redistribution of the surface charges, and a finite demagnetizing field. Instead, Hubert [23] has suggested that this redistribution can be simulated with the transformation,

$$z \to z - \frac{2\Delta_B \sinh(\frac{z}{2\Delta_B})}{\cosh(\frac{h}{4\Delta_B})} \quad , \tag{2.3.5}$$

which is only effective within a few wall widths of the surface. Use of this transformation does not significantly alter the wall twist structure, but it does eliminate the unrealistic singularities at the film surfaces.

The fields in Eqs. (2.3.2-4), as modified by the transformation, Eq. (2.3.5), are shown in Fig. (2.3.1). Here, H_s is plotted as a function of position through the film thickness. The values of bubble radius, $r_o = 1.1h$, and stripe width, $d = 2.3\ h$, represent typical

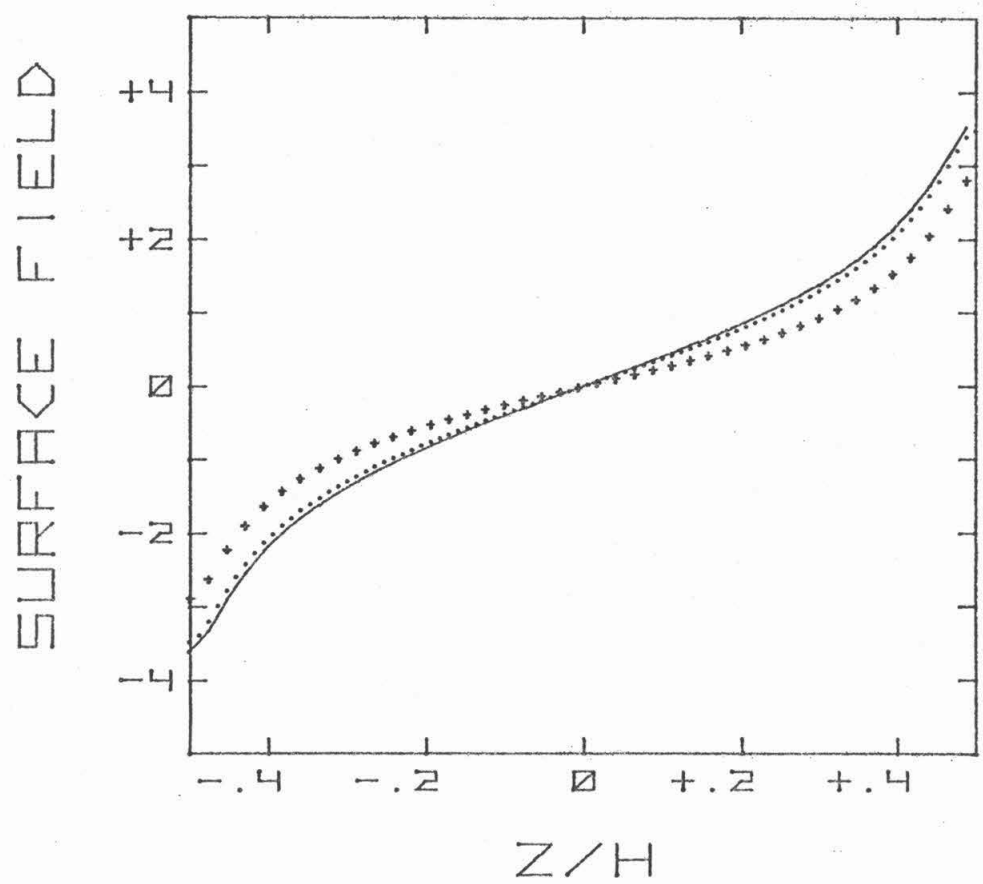

Fig. 2.3.1. Perpendicular Component of the Surface Demagnetizing Field, $H_s/4M_s$, as a Function of Position, Z/H, in Isolated Walls (solid), Parallel Zero-bias Stripes (dotted) and Bubble Domains (+). The bubble radius, r_o = 1.1 h, and the stripe width, d = 2.3 h, used in the calculation are typical for these domain structures.

domain geometries found in these materials (see Appendix A). From symmetry, the fields are antisymmetric about the film center. It can be seen that the fields in an isolated wall are almost identical to those found in zero-bias stripe domains. However, the fields found in bubble domains are always slightly smaller than in the other configurations. Since the most accurate experimental data presented in Ch. 3 were obtained in stripe domains, the examples given in the remainder of Ch. 2 are for zero-bias stripes. Examples from bubble domains are not significantly different.

Additional exchange terms must be incorporated in L_a, because the wall structure varies with z. To simplify the analysis, changes in wall width are neglected, so that Δ is always Δ_B. With this assumption, contributions to exchange from θ_z come from two sources: variations in wall position, $\partial q/\partial z = q_z$, and variations in boundary conditions, θ_z^o. Since contributions from this latter source are second order in h_{ip}, they may be negelcted. Contributions to L_a from q_z are given, to first order in h_{ip}, by

$$\int_{-\infty}^{+\infty} dy\ A\theta_z^2 = \frac{2A}{\Delta_B} q_z^2 \quad . \tag{2.3.6}$$

Contributions to exchange from variations in the boundary condition, ϕ_z^o, may also be neglected, since these terms, being proportional to $\sin^2\theta^o$, are also second order. Inside the wall, $\sin^2\theta$ is not small, and large changes in ϕ can occur, so contributions from ϕ_z must be included. To first order, this additional exchange energy is given by

$$\int_{-\infty}^{+\infty} dy\ A\sin^2\theta\ \phi_z^2 = 2A\Delta_B\ \phi_z^2 \quad . \tag{2.3.7}$$

Because H_s, and hence the wall structure, vary over distances much larger than the wall width, these additional terms are much smaller than the exchange energy of the wall itself, $\frac{2A}{\Delta_B}$.

Additional magneto-static interactions are also introduced by variations in wall structure. Since ϕ varies with z, interaction between $\nabla\cdot\overline{M}$ within the wall is no longer given exactly by the local form, Eq. (2.1.1). However, because the charge distribution takes the form of two charged sheets separated by a short distance, Δ_B, the characteristic interaction length is only a few Δ_B [22,24]. Since wall structure changes are negligible over such distances, this magneto-static interaction is still given approximately by the local form. Additional sources occur whenever the wall is not parallel to the easy axis, i.e., whenever q_z is not zero [16]. However, it is assumed that q_z is much smaller than one, so that these additional sources may be neglected. With these approximations, the demagnetizing energy density is still only a function of the local orientation of $\overline{M}$.

Static Twisted Wall Structure

Differential equations for the static wall structure are obtained by substituting the Lagrangian into Eq. (2.i.3a). By combining the results from Eqs. (2.2.5) and (2.3.6,7), the Lagrangian may be written as

$$L_a = \frac{2M_s}{\gamma}\dot{\phi}q - \sigma_B + 2M_sH_zq - \frac{2A}{\Delta_B}q_z^2 - 2A\Delta_B\phi_z^2$$

$$+ \pi M_sH_x\Delta_B\cos\phi + \pi M_s(H_y + H_s(z))\sin\phi$$

$$- 4\pi M_s^2\Delta_B\sin^2\phi \quad . \qquad (2.3.8)$$

Note that the in-plane field perpendicular to the wall consists of a homogeneous component from external sources H_y, and an inhomogeneous component from the surface fields $H_s(z)$. In a stationary wall, $\dot{q}$, ϕ, and H_z are zero, so that the first and last terms in Eq. (2.i.3a) are zero. By substituting Eq. (2.3.8) into Eq. (2.i.3a), the following differential equations are obtained:

$$\phi_{zz} = \frac{\pi M_s}{4A}\left[H_x\sin\phi - (H_y + H_s(z))\cos\phi + 4M_s\sin 2\phi\right], \qquad (2.3.9a)$$

and

$$q_{zz} = 0 \quad . \qquad (2.3.9b)$$

It is assumed that there is no interaction between the wall and the material boundaries, so that the proper boundary conditions are, from Eq. (2.i.3c), $\phi_z = 0$, and $q_z = 0$. The only solution of Eq. (2.3.9b) that is consistent with these conditions is $q_z = 0$, i.e., a flat wall parallel to the easy axis. The effects of wall bulging, which are only thought to be significant in very thick materials [25], have been neglected here.

An approximate form the wall twist structure is obtained by neglecting exchange in Eq. (2.3.9a). In the absence of external in-plane fields, the approximate form is

$$\phi(z) = \arcsin\left(\frac{H_s(z)}{8M_s}\right) \quad . \tag{2.3.10}$$

This magnetostatic solution is shown as a dotted curve in Fig. (2.3.2). In regions where $H_s > 8M_s$, ϕ is taken as $\frac{\pi}{2}$, and in regions where $H_s < -8M_s$, ϕ is $\frac{-\pi}{2}$. The points where $|H_s|$ is equal to $8M_s$ are called the critical points, z_{c1} and z_{c2}. The surface field is strong enough near the top surface to rotate $\overline{M}$ out along the +y-axis, perpendicular to the plane of the wall. Similarly, $\overline{M}$ is along the -y-axis near the bottom surface. Between the critical points, $\overline{M}$ rotates gradually between these two orientations, with $\overline{M}$ in the film center along the +x-axis. There is an equally valid solution with an opposite sense of wall chirality, in which $\overline{M}$ in the film center is along the -x-axis.

More accurate twist structures are obtained by taking into account exchange effects. This is usually done in one of two ways. In the Ritz method [21,22,24,26], the wall structure is approximated by a trial function, which contains several adjustable parameters. The total energy of the system is calculated, and then minimized with respect to these parameters. This method has the advantage that non-local dipole interactions are treated rigorously. One disadvantage is that solutions are restricted by the choice of trial functions. In some situations [21], where the trial function is not sufficiently

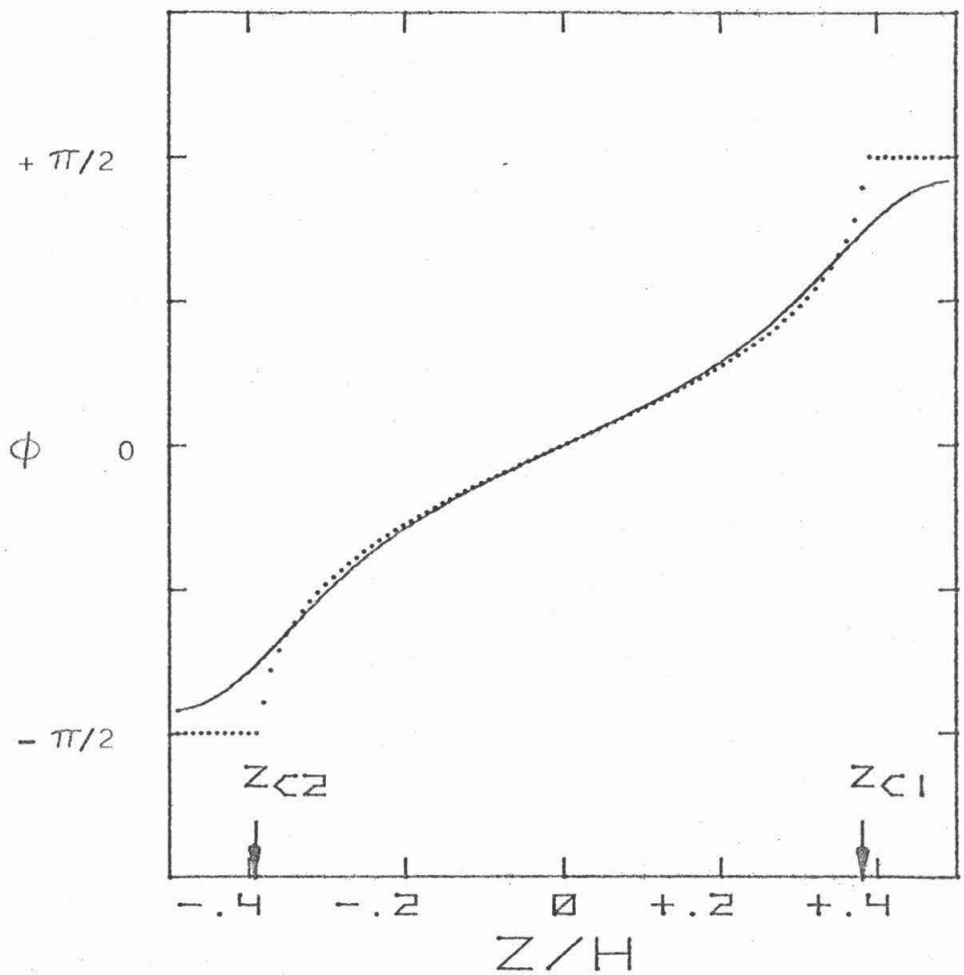

Fig. 2.3.2. Azimuthal Angle ϕ as a Function of Position Through the Film Thickness, z/h, in a Static Twisted Wall. The magnetostatic structure (dotted) was obtained by neglecting exchange effects. The solid curve, which includes the effects of exchange, was calculated numerically. Both structures were obtained by using $H_s(z)$ from zero-bias stripes. The arrows indicate the upper and lower critical points, z_{c1} and z_{c2}.

general, the Ritz method can lead to erroneous results. In the numerical technique used here, the solution is calculated at a set of 100 grid points, spaced equally through the film thickness. At each point (indexed by i) the derivative in Eq. (2.3.9a) is replaced by the finite difference expression,

$$\phi_{zz} = \frac{\phi_{i+1} - 2\phi_i + \phi_{i+1}}{(\Delta z)^2} \quad , \tag{2.3.11}$$

where Δz is the grid point spacing. This results in a system of nonlinear equations for the solutions ϕ_i, which is solved by using the Newton-Raphson iterative method [12]. The boundary conditions are imposed by setting ϕ_i at the first two and last two grid points equal to each other. This method has the advantage that the solutions are completely general, but one disadvantage is that the nonlocal interactions must be approximated by a local expression, as discussed earlier. The twist functions obtained here are similar to those obtained earlier [15] by using a similar numerical method.

An example of the twist structures obtained with this method is shown in Fig. (2.3.2) as a solid curve. The surface fields used in this calculation were the same as those used to calculate the magnetostatic solution (dotted curve). The material parameters were taken from the sample investigated in Ch. 3. The only significant difference between these two solutions occurs near the critical points. Since exchange energy was neglected in calculating the magnetostatic solution, this solution greatly overestimates this energy component.

In the numerical solution, ϕ moves away from the magnetostatic solution in such a way that the corresponding rise in energy due to $-M_y H_s$ is more that offset by the reduction in exchange energy. In the film center, exchange effects are negligible, and the two solutions are nearly the same. The average energy of this twist structure is lower than σ_B due to the presence of the surface fields; however, since these fields are much smaller than H_k, the reduction is only about 2%. As with the magnetostatic solution, there is a second, equivalent numerical solution with the opposite sense of wall chirality.

Motion of Twisted Wall Structures

Equations of motion for twisted wall structures are obtained by substituting the Lagragian, Eq. (2.3.8), into the Euler equations, Eq. (2.i.3a). By treating q and ϕ as dynamical variables, two equations are obtained [27]:

$$\dot{q} = \gamma\Delta_B \left[f(\phi) - \frac{2A}{M_s}\phi_{zz}\right] + \alpha\Delta_B\dot{\phi} \quad , \tag{2.3.12a}$$

and

$$\dot{\phi} = \gamma\left[H_z + \frac{2A}{M_s}\frac{q_{zz}}{\Delta_B}\right] - \alpha\frac{\dot{q}}{\Delta_B} \quad , \tag{2.3.12b}$$

where

$$f(\phi) = \frac{\pi}{2}\left[H_x \sin\phi - (H_y + H_s(z))\cos\phi\right] + 2\pi M_s \sin 2\phi \quad . \tag{2.3.12c}$$

These equations are similar to those derived earlier for the motion of one-dimensional structures, except for two additional exchange terms. The first equation indicates that the local velocity is governed primarily by the orientation of ϕ, as in Secs. 2.1 and 2.2. The dynamic effects of curvature on the velocity are characterized by the parameter, $\frac{2A}{M_s h^2}$. Since this parameter is typically less than 1 Oe in most materials, while $f(\phi)$ is usually at least 50 Oe, curvature in $\phi(z)$ does not significantly affect the local wall velocity. The second equation indicates that the rotation of ϕ is governed by a combination of the external field and curvature in the wall surface. The effects of exchange in this case can be significant. The boundary conditions are the same as those in the static case, $\phi_z = 0$, and $q_z = 0$. These equations of motion form the basis for the analysis of twisted wall motion presented here.

The time dependence of the average value of ϕ is determined primarily by the external field. The average value may be calculated from Eq. (2.3.12b) by integrating through the film thickness. In the limit, $\alpha \to 0$, the result is [27]

$$\frac{1}{h}\int_{-\frac{h}{2}}^{+\frac{h}{2}} dz\ \dot{\phi}(z) = \langle\dot{\phi}\rangle = \gamma H_z \quad . \tag{2.3.13}$$

Quantities averaged through the film thickness will be indicated by brackets, e.g., $\langle\phi\rangle$. The boundary condition, $q_z = 0$, has been used to eliminate the term proportional to q_{zz}. Since $\langle\phi\rangle$ is proportional to

the average wall momentum, this states that the time rate of change of momentum is proportional to the external field, regardless of the internal wall structure. Because the sum of the internal torques due to wall curvature is zero, one-dimensional and twisted wall structures obey the same momentum principle.

Steady-State Motion

The equations of motion may be solved by assuming steady-state conditions. The wall is assumed to be flat (q_z=0) and moving with a constant velocity v. The twist structure does not change with time, so that $\dot{\phi}$ is zero everywhere. With these assumptions, Eqs. (2.3.12a-b) reduce to

$$\phi_{zz} = \frac{\pi M_s^2}{A} \left(\frac{f(\phi)}{2\pi M_s} - \frac{v}{v_w} \right) \quad , \tag{2.3.14a}$$

and

$$v = \mu H_z \quad . \tag{2.3.14b}$$

The first equation specifies the twist structure as a function of v, and also the inverse relationship, $v(\langle\phi\rangle)$. It is identical to the static condition, Eq. (2.3.9a), except for an additional constant term v/v_w. Since the internal structure is constant by assumption, no additional energy can be stored internally, and all input energy from the external field must be dissipated by viscous damping. Hence, twisted walls in steady-state motion obey the same linear mobility

relation as one-dimensional structures.

Twisted wall motion may be modeled as simple harmonic motion in the limit of small steady-state velocities. Assume that for small deviations from static conditions, the average velocity $\langle \dot{q} \rangle$ follows the steady-state relation $v(\langle \phi \rangle)$ given by Eq. (2.3.14a). Also assume that the wall is subject to a restoring force as discussed previously. Eqs. (2.3.12a-b) are then linearized by approximating $v(\langle \phi \rangle)$ around $\langle \phi \rangle = 0$ by $v_o' \langle \phi \rangle$, where $v_o' = \left. \frac{\partial v}{\partial \langle \phi \rangle} \right|_o$. The result is a linear harmonic oscillator equation for the average wall position similar to Eq. (2.2.18). The effective wall mass is given by

$$m = 2m_D \left(\frac{v_w}{v_o'} \right) \quad . \tag{2.3.15}$$

For the simple twisted wall shown in Fig. (2.3.2) as a solid line, the effective mass is 1.7 m_D, in agreement with calculations by Hubert [23], and Schlöman [28]. Hence, for small steady-state velocities, a twisted wall can be treated as a harmonic oscillator, but its effective mass is nearly twice the Döring mass.

The wall surface may be treated as a flexible membrane for small deviations from steady-state structures. Assume that the wall is moving with some steady-state configuration, specified by Eq. (2.3.14a). The twist function is expanded around its steady-state configuration. Similarly, the wall velocity is expanded around v as $\dot{q} = v + \dot{\varepsilon}(z)$. Expand $f(\phi)$ at each point by the first term in its Taylor series. By neglecting damping, Eqs. (2.3.12a-b) may be reduced to

$$\ddot{\varepsilon} = \frac{S}{m}\,\varepsilon_{zz} - \left(\frac{2\gamma A}{M_s}\right)^2 \frac{\partial^4 \varepsilon}{\partial z^4} \qquad (2.3.16)$$

For small deviations, the term proportional to $\frac{\partial^4 \varepsilon}{\partial z^4}$ may be neglected, so that Eq. (2.3.16) reduces to the wave equation. Here, the surface tension S is just the exchange energy density, $\frac{2A}{\Delta_B}$, and the local mass density m is given by Eq. (2.2.16). Deviations from a flat wall propagate along the surface as traveling waves with local phase velocities, $\sqrt{\frac{S}{m}}$. Hence, the wall surface may be treated as a flexible membrane with a nonuniform mass density.

The steady-state approach used here is only valid over a limited range in $\langle\phi\rangle$. Recent numerical calculations by Hubert [23] indicated that solutions to Eq. (2.3.14a) only exist for $|v| < 0.21\ v_w$ and $|\langle\phi\rangle| < 0.27$. For drive fields larger than $0.21\ H_w$, the wall cannot move with a flat surface and constant internal twist structure. This situation is analogous to the oscillatory motion in one-dimensional wall structures described earlier. Hence, while the steady-state approximation is useful in analyzing small deviations from static conditions, it cannot describe motion at higher drive fields.

Twisted Wall Motion in the Presence of Horizontal Bloch Lines

Twisted wall motion under higher drive field conditions is dominated by internal wall structure. If $\langle\phi\rangle$ rotates beyond the limit of steady-state motion, dynamic forces within the wall produce an internal

twist structure, called a horizontal Bloch line (HBL). This structure is a variation of ϕ along the z-direction, and constitutes a bridge between opposite senses of wall chirality. The region of rapid rotation [see Fig. (1.3)] extends horizontally along the wall surface As the HBL moves vertically, the dynamic properties of the wall are strongly affected. In the first part of this analysis, the dynamic forces which result in HBL nucleation and propagation are described. In the second part, the effects of the HBL on wall motion are estimated by using the HBL model. Finally, more accurate solutions of the equations of motion are obtained, and the results are compared with the qualitative analysis.

Horizontal Bloch Line Nucleation and Propagation

A qualitative understanding of the HBL nucleation process is obtained by considering local dynamic properties within the wall. Recall that the local properties are governed primarily by the steady-state velocity function, $v(\phi)=\gamma\Delta_B f(\phi)$ [see Eq.(2.3.12a)]. This function has been calculated at five different points through the film thickness, and the results are shown in Fig.(2.3.3). The static value of ϕ at each point is indicated by a large dot. The open circles indicate the values of ϕ in a wall with the opposite sense of chirality. The vertical scale, $2v_w$, is also indicated. It can be seen that the local dynamic properties are strongly influenced by the surface fields. Curve A was calculated for a point just above the upper critical point, at z/h=0.45.

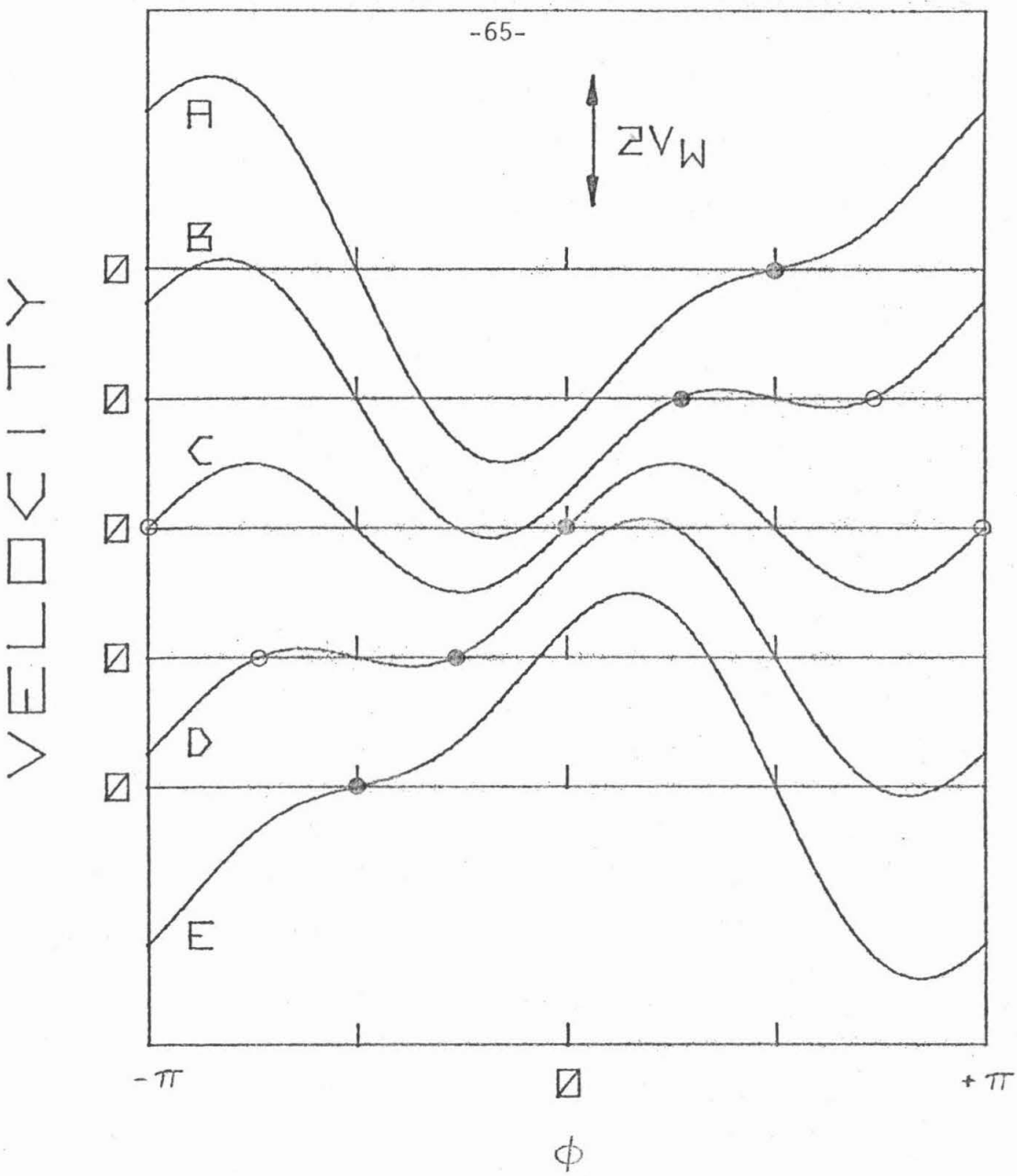

Fig. 2.3.3. Steady-State Velocity, $y = \gamma\Delta_B f(\phi)$, as a Function of ϕ at Five Different Points Through the Film Thickness. Curves A through E were calculated for z/h = 0.45, -.35, 0, -0.35, and -0.45, respectively. The surface fields from zero-bias stripes were used. The static value of ϕ at each location is indicated by a large dot for one of chirality and by an open circle for the other. The vertical scale is indicated by the velocity, $2v_w$.

The large surface field at this point (9.9 M_s) reorients the center spin perpendicular to the wall, so that the static value of ϕ is $+\frac{\pi}{2}$. Since point A is above the upper critical point, this value also applies to a wall with the opposite sense of chirality. The velocity curve reflects the 2π-periodicity associated with in-plane fields, rather than the π-periodicity associated with the demagnetizing energy in the Walker model. Note that the maximum steady-state velocity is increased by the surface field from v_w to 3.1 v_w. Curve B was calculated for a point just below the upper critical point, at z/h = 0.35. Here the surface field is somewhat smaller (6.0 M_s), so that the center spin is only partially aligned with the surface field. The static value of ϕ is 0.27π for one sense of chirality, and 0.73π for the other. The maximum velocity, 2.1 v_w, is lower, and the curve shows the influence of the demagnetizing energy, especially in the region near $\phi = \frac{\pi}{2}$. Curve C was calculated for a point at the film center, where the surface field is zero. Because no surface fields are present, the static value of ϕ is either zero, or π, depending on wall chirality. The maximum velocity here is just v_w. This same curve was discussed earlier in connection with the Walker model [see Fig. (2.1.2)]. Curves D and E were calculated for points just above and below the lower critical point, at z/h = -0.35 and -0.45, respectively. Since the surface fields are antisymmetric about the film center, these curves are just reflections of curves B and A about the line $\phi = 0$.

Horizontal Bloch line nucleation results from local dynamic

properties near the critical points. For example, consider the case in which a positive drive field is applied to a stationary wall. Initially, the wall has a flat surface ($q_z = 0$), and a static twist structure like those described earlier. Since both q_{zz} and $\dot{q}$ are initially zero, the initial rotation rate, $\dot{\phi} = \gamma H_z$, is the same everywhere [see Eq. (2.3.12b)]. It can be seen from Fig. (2.3.3) that points just below the upper critical point (e.g., point B) soon encounter a region in ϕ where $v(\phi)$ is essentially zero. Elsewhere, wall velocities are still increasing (e.g., at points A, C, D, and E), so that the wall section near point B eventually lags behind the rest of the wall. This produces a large, backward wall bulge in which q_{zz} is positive. This positive curvature significantly increases $\dot{\phi}$ in the wall section near point B, so that ϕ rotates rapidly toward higher angles. Once ϕ passes the magnetostatic orientation corresponding to the opposite sense of wall chirality (open circle), $v(\phi)$ becomes large and positive. The wall section at point B catches up the rest of the wall, and the bulge disappears, so that the local value of $\dot{\phi}$ is again the same as in the rest of the wall. The values of ϕ at points A and B correspond to the other sense of chirality, while the values at points C, D, and E still correspond to the original sense of chirality. Somewhere between points B and C, a bridge between opposite wall chiralities, an HBL, is formed. A similar analysis applies for negative drive fields, but in this case the HBL nucleates at the lower critical point. In this way, the wall bulge formed as a result of local dynamic properties provides the additional rotation necessary

to nucleate a horizontal Bloch line.

The additional rotation necessary to propagate the HBL toward the opposite film surface is also provided by the wall bulge. Again, assume that the drive field is positive. As rotation continues, new points closer to the lower surface rotate into regions where the average value of $v(\phi)$ is essentially zero. For example, when the local value of ϕ at point C reaches $\frac{\pi}{4}$, $v(\phi)$ decreases and becomes negative. At the same time, velocities at other points in the wall are relatively large and positive, so that eventually the wall section at point C lags behind the rest of the wall. This produces positive wall curvature, which increases the local values of $\dot{\phi}$, so that the center spin quickly rotates toward the opposite sense of chirality. When ϕ rotates beyond the magnetostatic value (open circle), $v(\phi)$ becomes large and positive again. The wall section at point C catches up to the rest of the wall, and the bulge moves on toward the lower surface. Now, only points D and E correspond to the original wall chirality, while points A, B, and C correspond to the opposite chirrality. The HBL is now somewhere between points C and D. In this way, the wall bulge propagates the HBL toward the lower surface.

This analysis indicates that HBL nucleation may not occur at higher drive fields. Nucleation depends on the formation of a wall bulge, which increases the local value of $\dot{\phi}$ through the effects of wall curvature. The size of the bulge, and hence, the size of the increase in $\dot{\phi}$, depends on how long ϕ remains within the region of low average velocity. For example, consider point B in Fig. (2.3.3). If

the drive field is small, $\dot{\phi} = \gamma H_z$ is small, and ϕ spends a relatively long time in the region where $v(\phi)$ is small, i.e., in the region between the dot and the open circle. During this time, the wall section at point B is almost stationary, while the rest of the wall is moving forward, so that a relatively large bulge is formed. The additional rotation from wall curvature is sufficient to nucleate the HBL. However, if the drive field is larger, ϕ spends a short time in the low velocity region, and a smaller bulge is formed. For sufficiently large drive fields, the additional rotation from the bulge may not be sufficient to nucleate an HBL. Therefore, it seems likely that the wall twist structure at high drive fields does not contain HBL's, but instead more closely resembles the initial static twist structure.

The Horizontal Bloch Line Model

An approximate model of twisted wall motion has been proposed by Argyle *et al.*[30], and by Slonczewski [27] in which wall motion is dominated by horizontal Bloch lines. Because wall motion is strongly affected by these structures, the steady-state approximation can no longer be used. Instead, the principles of energy and momentum conservation given in Eqs. (2.2.13) and (2.3.13) are used to estimate dynamic behavior. The HBL model was originally proposed in order to account for the average wall behavior associated with velocity saturation. Here, it is shown that the HBL strongly affects the instantaneous wall behavior as well.

The internal structure assumed in the HBL model is shown schematically in Fig. (2.3.4). It is assumed that $\phi(z)$ always lies near one of the magnetostatic solutions (dotted curves). Soon after H_z is applied, an HBL nucleates near the upper critical point z_{c1}, and travels toward z_{c2}. An example of such a twist structure is shown in curve (ABCDE). The total rotation within the HBL, $2\zeta^o$, depends on the HBL position z_L according to

$$\zeta^o = \arccos\left(\frac{H_s(z_L)}{8M_s}\right) \quad . \tag{2.3.17}$$

The average value of ϕ is related to z_L by

$$\langle\phi\rangle = \frac{2}{h}\int_{z_L}^{z_{c1}} dz\ \zeta^o(z) \quad , \tag{2.3.18}$$

By combining the results of Eqs. (2.3.17-18), it can be seen that as $\langle\phi\rangle$ increases, the HBL moves toward the bottom surface. The motion of the HBL is determined from H_z by relating $\langle\dot{\phi}\rangle$ from Eq. (2.3.13) to z_L through Eq. (2.3.18).

The wall velocity is determined by considering the distribution of energy within the magnetic system. The input power per unit wall length from the external field, $2M_sH_zh\langle\dot{q}\rangle$, must either be dissipated by viscous damping, or be stored by internal structure. For a typical saturation velocity of 10 m/sec, it is clear from Eq. (2.2.8) that unless that wall structure is drastically different from a Bloch wall structure, the wall can, at most, dissipate only a few percent of the input power. Therefore, the remaining energy must be stored

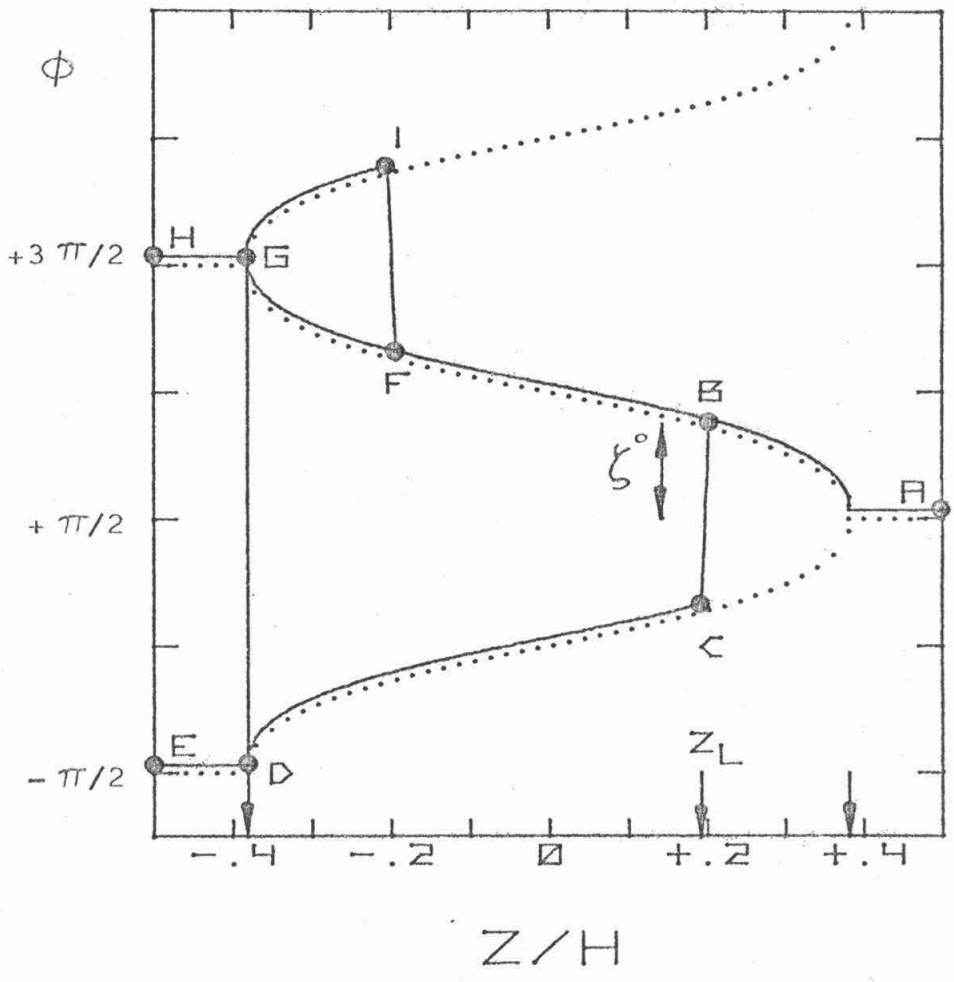

Fig. 2.3.4. Schematic Diagram of the Wall Twist Functions $\phi(z)$ assumed in the HBL Model. The dotted curves represent the static twist structure, while the solid curves represent various dynamic structures. The upper and lower critical points, and the HBL position z_L are indicated by arrows. The HBL twist angle ζ^o is also shown.

internally. Assuming that all of the energy goes into the HBL, the input power may be equated to $\dot{\varepsilon}_L$, the time rate of change of the HBL energy. By making use of momentum conservation, Eq. (2.3.13), the average wall velocity is given by

$$\dot{<q>} = \frac{\gamma}{2M_s h} \frac{\partial \varepsilon_L}{\partial <\phi>} \quad . \tag{2.3.19}$$

Here, $\dot{\varepsilon}_L = \frac{\partial \varepsilon_L}{\partial <\phi>} \dot{<\phi>}$ has been used. Just as with the one-dimensional structures, the velocity is not directly related to the external drive field. Instead, it is governed by changes in HBL energy as it moves through the film thickness.

The HBL energy is estimated by minimizing the local kinetic energy density. The kinetic energy in twisted walls is given approximately by

$$\sigma_{KE} = -2A\Delta_B \phi_z^2 - \pi H_s(z) M_s \Delta_B \sin\phi + 4\pi M_s^2 \Delta_B \sin^2\phi \quad , \tag{2.3.20}$$

where the effects of external in-plane fields and wall bulging have been neglected. It is assumed that H_s does not vary significantly across the HBL width, so that $H_s(z)$ may be approximated by the constant, $H_s(z_L)$. By making use of the substituting, $\zeta(z) = \pi - \phi(z)$, and the definition of the magnetostatic solution, Eq. (2.3.10), the kinetic energy may be written as

$$\sigma_{KE} = 2A\Delta_B \zeta_z^2 + 4\pi M_s^2 \Delta_B (\cos\zeta - \cos\zeta^o)^2 \quad . \tag{2.3.21}$$

The HBL structure minimizes this energy subject to the boundary con-

ditions, $\zeta \to \pm\zeta^o$ as $z \to \pm\infty$, where ζ^o is given by Eq. (2.3.17). This problem is similar to the one-dimensional wall structure calculation considered in Sec. 2.1. In a domain wall, which represents a continuous rotation between opposite orientations along the easy axis, the width is determined by a compromise between exchange and anisotropy energies. Similarly, an HBL represents a continuous rotation between opposite wall chiralities. The HBL width is mainly determined by a compromise between exchange and demagnetizing energies, but since the demagnetizing energy is smaller than K_u by a factor of Q^{-1}, the HBL width is expected to be wider than Δ_B by a factor $\sqrt{Q}$.

The HBL shape and energy are obtained by minimizing the energy in Eq. (2.3.21). The HBL shape satisfies the usual Euler equation that is obtained by using standard techniques from the calculus of variations. The first integral,

$$4\pi M_s^2 \Delta_B (\cos\zeta - \cos\zeta^o)^2 = 2A\Delta_B \zeta_z^2 \quad , \tag{2.3.22}$$

indicates that the exchange energy is everywhere equal to the sum of the demagnetizing and surface field energies. With this result, the HBL energy is given by [27]

$$\varepsilon_L = 2\int_{-\infty}^{\infty} dz (2A\Delta_B \zeta_z^2) = 8AM_s\sqrt{\frac{2\pi}{K_u}} \cdot (\sin\zeta^o - \zeta^o\cos\zeta^o) \, . \tag{2.3.23}$$

This represents the additional kinetic energy per unit wall length due to the presence of the HBL. From the first integral, the wall shape is given by

$$z(\zeta) - z_L = \sqrt{Q}\,\Delta_B \int_0^{\zeta} d\zeta' \,(\cos\zeta' - \cos\zeta^o)^{-1} \quad . \tag{2.3.24}$$

The characteristic width of the HBL is just $\sqrt{Q}\,\Delta_B$, as expected. The actual size of the HBL is estimated by approximating $\zeta(z)$ by a straight line with slope, $\zeta_z|_{z=z_L}$. The HBL width W_L is just the distance between points where ζ reaches $\pm\zeta^o$, or

$$W_L = \frac{2\zeta^o\sqrt{Q}\,\Delta_B}{1-\cos\zeta^o} \quad . \tag{2.3.25}$$

Note that W_L is infinite when $\zeta^o = 0$, i.e., at nucleation. This indicates that the HBL model cannot adequately describe the nucleation process.

The radius of wall curvature required to propagate the HBL along the wall may be estimated. When the HBL passes a fixed point, ϕ must rotate by $2\zeta^o$. The time available for this is $W_L/\dot{z}_L$, so that the average rotation rate is $2\zeta^o\,\dot{z}_L/W_L$. Assume that all of this rotation is supplied by the exchange term in Eq. (2.3.12b). By combining this result with Eqs. (2.3.25), (2.3.13), and (2.3.18), the required radius is given by

$$q_{zz}^{-1} = \frac{\zeta^o}{1-\cos\zeta^o} \cdot \frac{4A\sqrt{Q}}{M_s H_z h} \quad . \tag{2.3.26}$$

In most bubble materials, this corresponds to a radius of curvature that is roughly the same size as the film thickness.

The wall velocity may now be determined from ε_L. By combining the results from Eqs. (2.3.17-19) and Eq. (2.3.23), $\dot{q}$ is related to the surface demagnetizing field by

$$\langle \dot{q} \rangle = - \frac{\gamma A}{4M_s} \sqrt{\frac{2\pi}{K_u}} \left(\frac{\partial H_s}{\partial z} \bigg|_{z_L} \right) \quad . \tag{2.3.27}$$

This average velocity has been calculated as a function of z_L for the demagnetizing fields from zero-bias stripes, and the results are shown in Fig. (2.3.5). The magnetic parameters used in this calculation were taken from the sample investigated in Ch. 3. When the HBL is nucleated, the velocity is at its peak value, v_p = 19 m/sec. As it moves toward the bottom surface, the velocity decreases, reaching its minimum value when the HBL is at the film center. As the HBL continues, the velocity rises again, and reaches v_p at z_{c2}. The peak velocity can be calculated analytically for the surface fields in an isolated wall, and the result is [27]

$$v_p = \frac{23.8\gamma A}{h\sqrt{K_u}} \quad . \tag{2.3.28}$$

Since v_p depends on $\frac{\partial H_s}{\partial z}$, the peak velocity is sensitive to the domain configuration.

Equations of motion are obtained by assuming that an HBL is always present somewhere between z_{c1} and z_{c2}. By combining Eqs. (2.3.13,17,18) and (2.3.27), these equations may be written as

$$\dot{z}_L = \frac{\gamma h H_z}{2} \left[\arccos\left(\frac{H_s(z_L)}{8M_s}\right) \right]^{-1} \quad , \tag{2.3.29a}$$

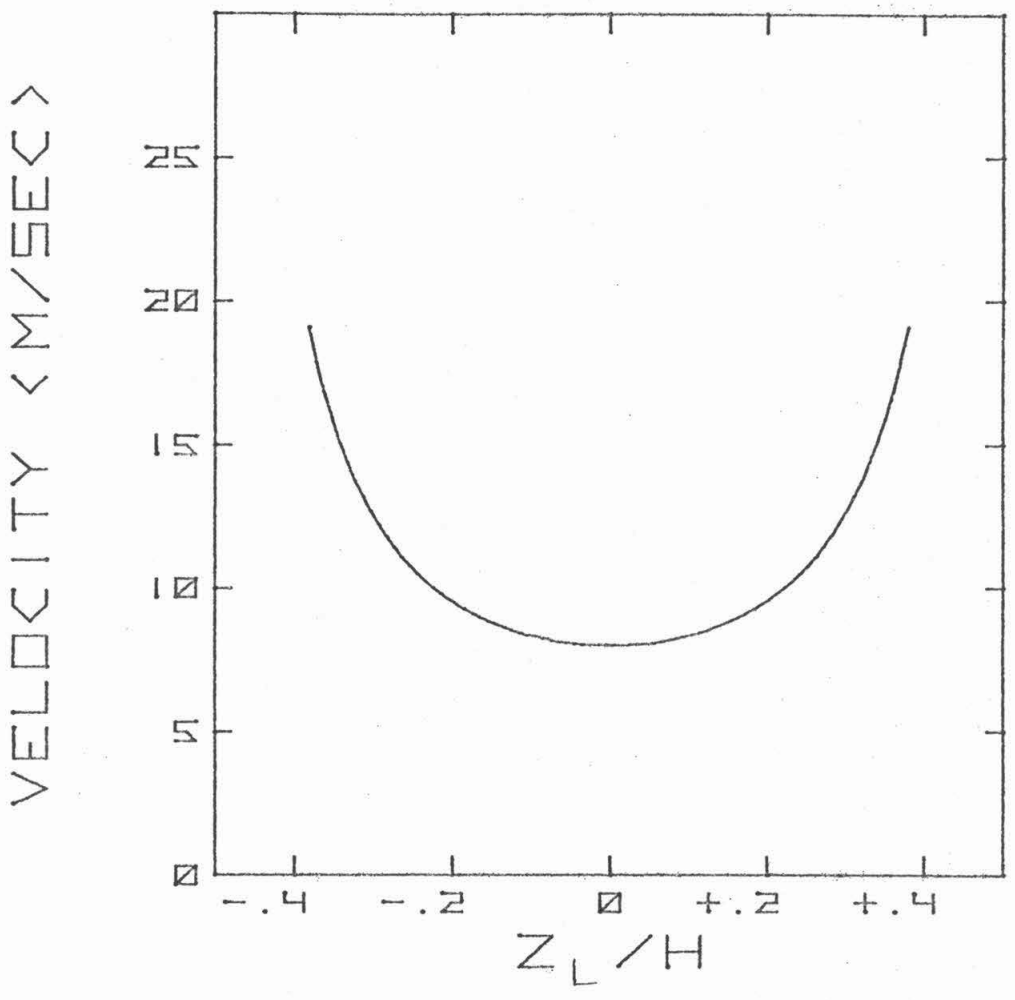

Fig. 2.3.5. Average Wall Velocity <q> (m/sec) as a Function of HBL Position, z_L/h, in Zero-Bias Stripes. The material parameters used in the calculation were taken from the material investigated in Ch. 3.

and

$$\langle \dot{q} \rangle = \frac{-\gamma A}{4M_s}\sqrt{\frac{2\pi}{K_u}}\left(\left.\frac{\partial H_s}{\partial z}\right|_{z_L}\right) \quad . \tag{2.3.29b}$$

Similar results, which include the effects of damping, have been obtained by Hagedorn [29]. However, in low-loss materials the effects of HBL damping are small. The first equation states that the HBL moves in response to H_z, as required by momentum conservation. The second equation, which comes from conservation of energy, relates the motion of the wall to the HBL position.

The twist in the HBL cannot increase indefinitely. When it reaches the lower critical point, i.e., when ζ^o reaches π, one of the two things can happen; either the HBL moves below z_{c2} and remains pinned near the surface, or it becomes unstable and disappears in a process called punch-through. It can be seen in Fig. (2.3.4) that if the HBL is pinned in region (HGDE), a second HBL can nucleate at z_{c2} and travel back toward the top surface. Such a structure can be seen in curve (ABFIGDE). This second HBL can also be pinned at the top surface, in which case a third HBL nucleates, and so on. This mechanism, known as HBL stacking [29], allows $\langle\phi\rangle$ to increase well beyond π by generating a number of HBL's. Note that the momentum stored in the stacked HBL's can be recovered by reversing this process, and returning the wall to its original chirality. According to the punch-through mechanism, the twist structure becomes unstable just before $\langle\phi\rangle$ reaches π. The exchange torque near the bottom surface is large enough to

rotate the spins in the region (ED) by 2π. After this rotation is completed, the twist structure, curve (ABFGH), is essentially the same as a static twist structure, but with the opposite sense of wall chirality. A second HBL, shown in curve (ABFIGH), nucleates at z_{c2}, and moves toward the top surface. Unlike the HBL stacking mechanism, punch-through causes irreversible changes in the wall structure; the momentum and energy associated with the HBL are lost, and the wall chirality is reversed. Which, if either, of these mechanism actually occurs must be determined experimentally.

Velocity Saturation

Wall velocities independent of drive field result when the HBL punches through each time it reaches the film surfaces. When punch-through occurs, it is assumed the stored kinetic energy is dissipated. When the HBL reaches either critical point, its energy is $8\pi AM_s\sqrt{2\pi/K_u}$, from Eq. (2.3.23). The time required to build up this energy is just the time required to rotate $\langle\phi\rangle$ by π, $\frac{\pi}{\gamma H_z}$ from Eq. (2.3.13). Hence, the average power absorbed by the HBL is $8AM_s\gamma H_z\sqrt{\frac{2\pi}{K_u}}$. By equating this to the average input power from the external field, $2\ M_s H_z h v_o$, the following expression for the time-averaged wall velocity v_o is obtained:

$$v_o = \frac{4\sqrt{2\pi}\ \gamma A}{h\sqrt{K_u}} \quad . \tag{2.3.30}$$

This average velocity is saturated, i.e., independent of the external

drive field. Incidentally, since v_o only depends on the HBL energy at the critical points, and since $H_s(z)$ is 8 M_s at these points by definition, the value of v_o does not depend on the domain configuration. The saturation velocity only depends on the energy dissipated during punch-through.

It can be seen from this analysis that velocity saturation does not require the existence of HBL's as a specific, micromagnetic structure. Velocity saturation comes from the assumption that a fixed amount of energy is dissipated during each π-rotation of $\langle\phi\rangle$. Other internal structures would serve equally well. For example, suppose the kinetic energy of a one-dimensional structure is lost each time it reaches its maximum value, when ϕ reaches $\frac{\pi}{2}$. Then from Eq. (2.2.13), the average input power is $\frac{\sigma_B \gamma H_z}{2\pi Q}$ so that the saturation velocity is

$$v_o = \frac{v_W}{\pi} \tag{2.3.31}$$

In most bubble materials, this is only about twice the saturation velocity expected from the HBL model. In a recent review, de Leeuw [31] reports that the average ratio of the experimental saturation velocity to v_o in Eq. (2.3.30) is 3.3±2.6, with extremes of 12.3 and 0.5. Clearly, the HBL model cannot account for the experimental data to within an order of magnitude. It seems clear that the factor-of-two difference between Eqs. (2.3.30,31), which results from assuming different internal wall structures, is not significant. Hence, the existence of velocity saturation does not, in any sense, imply the

existence of horizontal Bloch lines as specific structures. Instead it is only a rough indication of average power dissipation.

Section 2.4 Numerical Simulation of Twisted Wall Motion

More rigorous, numerical solutions of the equations of motion, Eqs. (2.3.12a-b), have been obtained by using the Dufort-Frankel method [12]. In this finite difference technique, the solutions $\phi(z,t)$ and $q(z,t)$ are calculated at regular time intervals for a set of points spaced equally through the film thickness. For a particular grid point (i) and time step (n), the spatial derivatives are replaced by

$$g_{zz} = \frac{g_{i-1,n} - g_{i,n+1} - g_{i,n-1} + g_{i+1,n}}{(\Delta z)^2} \quad , \qquad (2.4.1)$$

where g can be either ϕ or q. Here, Δz is the grid point spacing. The time derivatives are replaced by a similar expression,

$$\dot{g} = \frac{g_{i,n+1} - g_{i,n-1}}{2\Delta t} \quad , \qquad (2.4.2)$$

where Δt is the time step interval. The force-free boundary conditions, $\phi_z = 0$ and $q_z = 0$, are imposed at the surfaces. In the discussion of twisted wall motion presented in Sec. 2.3, approximations were made in describing solutions to the equations of motion. The solutions presented here represent more accurate descriptions of twisted wall motion, because their accuracy is only limited by the error associated with the numerical technique.

The equations of motion were solved for the particular case in which a constant drive field, H_z = 2 Oe, is suddenly applied to a stationary wall. For initial conditions, it was assumed that the wall slope q_z was zero everywhere, and that $\phi(z,t=0)$ was given by the static twist structure shown in Fig. (2.3.2) as a solid curve. The effective field gradient was zero, so that there was no restoring force acting on the wall. The material parameters used in the calculation were taken from the sample investigated in Ch. 3 (see Table 3.1). The grid spacing, h/51, was chosen so that internal wall structures were represented by several points, and the time step, Δt=0.1 nsec, was chosen so that changes in internal structure take place slowly in comparison with this time. The accuracy of the solution was verified by comparing results with those obtained by solving the equations with a completely different numerical algorithm, called the Crank-Nicolson method [12]. The values of $\langle\phi\rangle$ from these two solutions agree within 0.3%, and the values of $\langle q\rangle$ agree within 4%.

Results from this calculation are shown in Figs. (2.4.1-4). In Fig. (2.4.1), the average wall position, $\langle q\rangle/\Delta_B$ (solid), and the average angle, $\langle\phi\rangle$ (dotted), are shown as functions of time. The average angle is zero at t=0, and increases linearly with time. The behavior of $\langle q\rangle/\Delta_B$ is more complicated due to the presence of internal wall structure. Examples of the internal wall structure at various times during the motion are shown in Figs. (2.4.2-4). In each case, the angle ϕ is shown in the upper figure as a function of position through the film thickness, z/h. The dotted curve represents

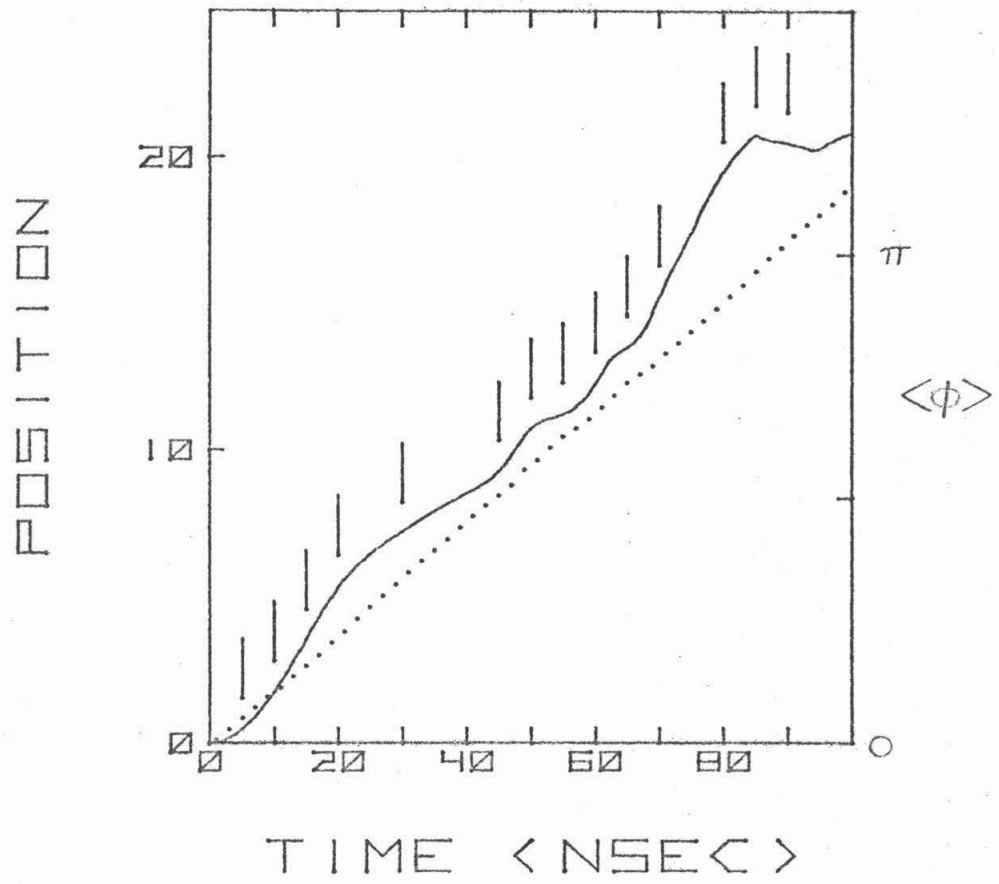

Fig. 2.4.1. Average Wall Position, $\langle q \rangle / \Delta_B$ (solid), and Average Azimuthal Angle, $\langle \phi \rangle$ (dotted), as Functions of Time (nsec) from a Numerical Solution of the Equations of Motion, Eqs. (2.3.12a-c). The drive field was constant, H_z = 2 Oe. Material parameters were taken from the sample investigated in Ch. 3. The times for which internal structures are shown in Figs. (2.4.2-4) are indicated by short line segments.

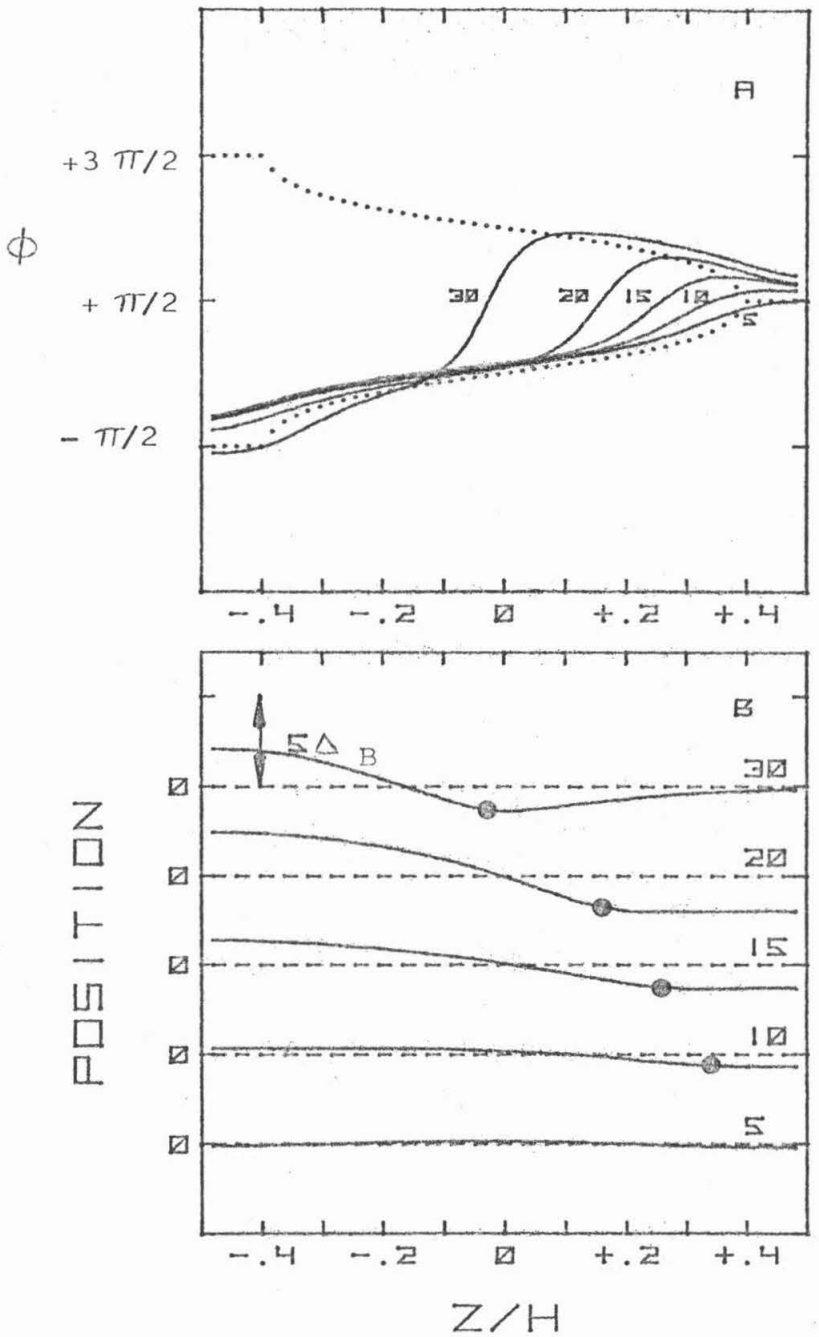

Fig. 2.4.2. Azimuthal Angle ϕ(A) and Wall Surface (q-<q>) (B) as Functions of Position Through the Film Thickness, z/h, for t = 5, 10, 15, 20 and 30 nsec. The dotted curve is the magnetostatic solution, Eq. (2.3.10). The dashed curve represents the average wall position at each time. The large dots indicate the position of the HBL.

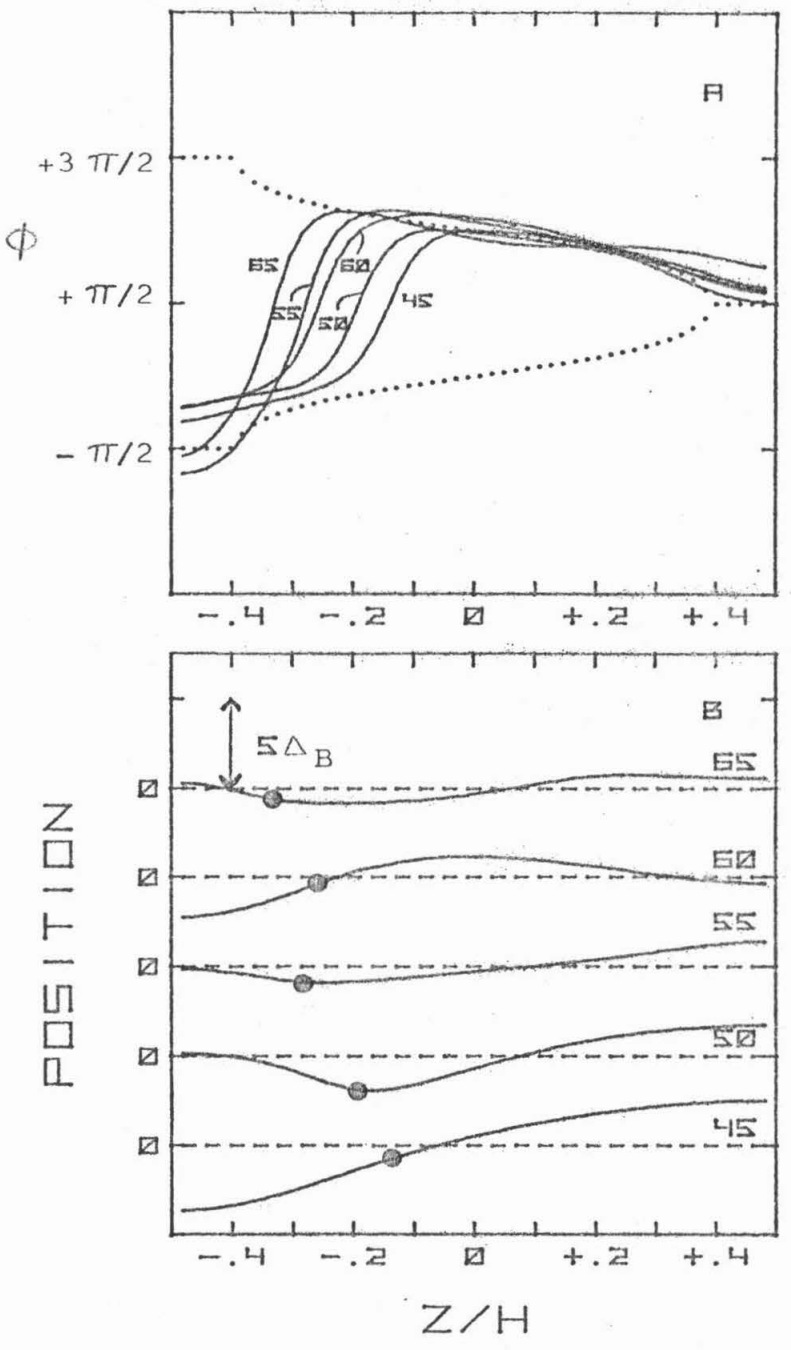

Fig. 2.4.3. Azimuthal Angle ϕ(A) and Wall Surface ($q-\langle q\rangle$) (B) as Functions of Position Through the Film Thickness, z/h, for t = 45, 50, 55, 60, and 65 nsec. The dotted curve is the magnetostatic solution, Eq. (2.3.10). The dashed curve represents the average wall position at each time. The large dots indicate the position of the HBL.

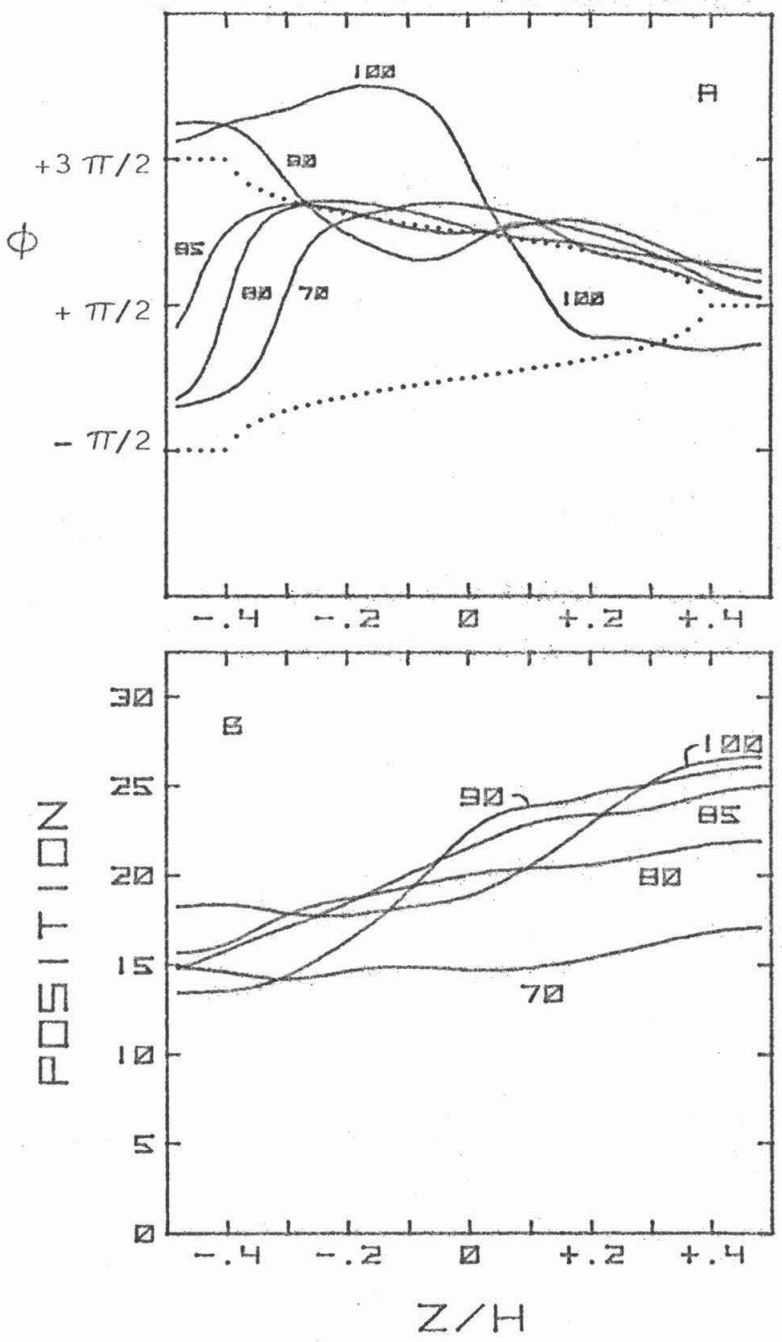

Fig. 2.4.4. Azimuthal Angle ϕ(A) and Wall Surface q(B) as Functions of Position Through the Film Thickness, z/h, for t = 70, 80, 85, 90, and 100 nsec. The dotted curve represents the magnetostatic solution, Eq. (2.3.10). The wall surfaces are shown relative to the initial starting position, q = 0.

the magnetostatic solution, Eq. (2.3.10), for both senses of wall chirality. In Figs. (2.4.2-3), the lower figures show the wall position q as a function of z/h relative to the average wall position $\langle q \rangle$, which is indicated by a dashed line. The large dots indicate the positions of the HBL's (i.e., where $\phi = \frac{\pi}{2}$) shown in the upper figures. The vertical scale is indicated by the distance $5\Delta_B$. To aid the discussion, the wall surfaces in Fig. (2.4.4) are shown relative to their initial position, q(z)=0, and the large dots have been omitted. In order to emphasize changes in the wall surface, the wall slopes $\frac{\partial q}{\partial z} = q_z$, have been exaggerated by a factor of 2.3. The times for which internal structures are shown in these figures are indicated in Fig. (2.4.1) by short vertical lines next to the solid curve.

During the initial wall response, a horizontal Bloch line is formed at the upper film surface. This nucleation process is shown in Fig. (2.4.2). Initially, the wall has a flat surface, and a relatively simple, static twist structure. When the drive field is applied, at t=0, the wall responds by increasing ϕ at a uniform rate, while maintaining a flat surface. After 5 nsec, the wall twist structure has moved up by a small amount, about 0.05π, with no significant change in shape. By t = 10 nsec, the wall surface has a small backward bend at the upper surface. The curvature in this region increases $\dot{\phi}$ locally, and causes the twist structure to rotate toward the opposite sense of chirality, as can be seen in the upper figure. As time continues, a bridge between opposite chiralities, an HBL, is gradually

formed. By t = 15 nsec, a small HBL can be seen at z = +0.26 h. Since $\langle\phi\rangle$ increases with time, the amount of twist in the HBL must also increase, and it moves toward the film center. By t = 20 nsec, the HBL is at z = +0.17 h. Note that as the twist in the HBL increases, the size of the bulge also increases in order to provide the required rotation necessary to propagate the HBL. By t = 30 nsec, the HBL has moved just beyond the film center, to z = -0.03 h. It must be emphasized that, while the structures shown here closely resemble those assumed in the HBL model, no a priori assumptions were made about the nature of these structures; the HBL structures shown here come directly from the equations of motion.

The presence of the HBL has a significant effect on the average wall behavior at the beginning of the motion, as can be seen in Fig. (2.4.1). This behavior results from two competing effects. Initially, the wall has a relatively simple structure, so that it tends to accelerate to a high velocity. As the HBL is formed, the wall absorbs less energy per unit increase in $\langle\phi\rangle$, so that the wall tends to decelerate. As a result, the wall accelerates to a maximum velocity of 21 m/sec at t = 16 nsec and then decelerates, reaching a minimum velocity of 6 m/sec at t = 39 nsec. Hence, the behavior of the average wall position is characterized by an initial fast response in which the wall is relatively structure-free, followed by HBL-dominated motion.

Internal vibrations of the wall surface, which can be seen in Fig. (2.4.3), produce the two small bumps in <q> shown in Fig. (2.4.1). Eqs. (2.3.29a) and (2.3.17) show that the HBL velocity is inversely proportional to the total twist contained in the HBL, $2\zeta^o$. As a result, the HBL slows significantly as it moves toward the lower film surface. The curvature required to propagate the HBL decreases so that the bulge separates from the HBL, and moves on toward the lower surface. At t = 45 nsec, the wall bulge has just reached the lower surface. Between t = 45 nsec and t = 50 nsec, the bulge reflects off of the lower film surface without change in sign, because of the force-free boundary condition. Because the wall surface has a nonuniform mass density, the bulge changes shape as it travels along the surface, so that, by t = 65 nsec, the bulge has broken up into a number of small undulations. Because ϕ and q are coupled dynamically, HBL motion is somewhat irregular due to variations in wall curvature associated with the internal vibrations. Recall that the presence of a wall twist increases the effective wall mass. With an HBL present, almost all of the wall mass is concentrated in the region of the HBL, so that the center of mass coincides with the HBL position. The effects of vibrations on the average wall position can be seen most clearly by considering the first bump. For t = 45 nsec, it can be seen in Fig. (2.4.3) that the center of mass is slightly behind the average wall position (dashed line). Between t = 45 nsec and t = 50 nsec,

the average wall position moves well ahead of the center of mass, so that the average velocity in this interval is relatively high, as can be seen in Fig. (2.4.1). Between t = 50 nsec and t = 55 nsec, the average position moves back toward the center of mass, which results in the relatively low velocity seen during this interval. The same analysis also applies to the second bump, but by this time, the vibrations are breaking up, so that the second bump is smaller than the first. For larger times, the vibrations have broken up, and the average position is no longer effected.

Punch-through occurs when the HBL reaches the lower film surface. Examples of the internal wall structures during this process are shown in Fig. (2.4.4). The twist functions are shown in the top figure just as in Figs. (2.4.2-3), but the wall surfaces q(z) are plotted relative to the initial starting position, q = 0, rather than relative to the average wall position. At t = 70 nsec, before punch-through begins, the HBL is at z = -0.31 h, and the wall surface is relatively flat, though small undulations from internal vibrations can still be seen. Between t = 70 nsec and t = 80 nsec, the wall moves forward, but the lower half moves more slowly than the upper half. This produces the deceleration of the average wall position shown in Fig. (2.4.1). During punch-through, between t = 85 nsec and t = 95 nsec, the upper half of the wall moves forward slightly, while the lower half moves backward by a relatively large amount.

As a result, the average wall position shown in Fig. (2.4.1) moves backward during this interval. Note that punch-through begins when $\langle\phi\rangle$ is 0.97π. Between t = 80 nsec and t = 85 nsec, the upper wall section still moves forward, while the section below z = -0.28 h moves backward slightly. During punch-through, the center spins near the lower surface rotate rapidly from about -0.13π toward $+3\pi/2$, as can be seen in the upper figure. The reason this produces the backward motion found near the lower film surface can be seen by considering Fig. (2.3.3e). Recall that this curve represents the local wall velocity, $\gamma\Delta_B f(\phi)$, as a function of ϕ for a point just below the lower critical point, at z = -0.45 h. Between t = 85 nsec and t = 95 nsec, when ϕ rotates between $+\pi/2$ and $3\pi/2$, Fig. (2.3.3e) shows that the local velocity is large and negative. This produces the large backward motion near the lower film surface. During punch-through, the HBL disappears due to rapid rotation of the center spins near the lower film surface. At the same time, local dynamic properties cause the wall section in this same region to move backwards. As a result, the average wall position remains constant during punch-through.

Kinetic energy from the HBL is transferred to the wall surface during punch-through, and stored as elastic and potential energy. The wall section near the lower surface moves backward, thereby increasing the wall's surface area, and returning energy to the external field. When the wall rebounds, energy is coupled into internal vibra-

tion modes. This produces very large fluctuations in both the wall surface and the wall twist function, which can be seen in Fig. (2.4.4) for t = 100 nsec. Presumably [27], the energy stored in the modes is eventually dissipated by viscous damping, and the wall is left with the opposite sense of chirality. If the drive field is maintained, a second HBL is formed at the lower critical point, and the process is repeated. However, the presence of vibrations makes the wall structure different from the initial static structure, so that a fast response like that found at the beginning of the calculations is not observed. In the example considered here, where the damping is very small, the vibrations persist, and the calculation diverges for t = 100 nsec. In other examples with higher damping, the periodic formation and punch-through of HBL's is observed.

In one sense, HBL propagation is analogous to domain wall motion. In the absense of surface demagnetizing fields, the magnetostatic curves shown in Fig. (2.4.2) would be horizontal lines, $\phi = 0$ and $\phi = \pi$. In order to change wall chirality, the center spins would have to rotate uniformly by π throughout the film thickness. The main effect of the surface fields is to move the magnetostatic curves closer together in the upper half of the wall, and farther apart in the lower half. Instead of changing chirality uniformly, it becomes much easier for the wall to change sequentially through HBL motion. In the same sense that wall motion represents sequential rotation between opposite orientations along the easy anisotropy axis, HBL

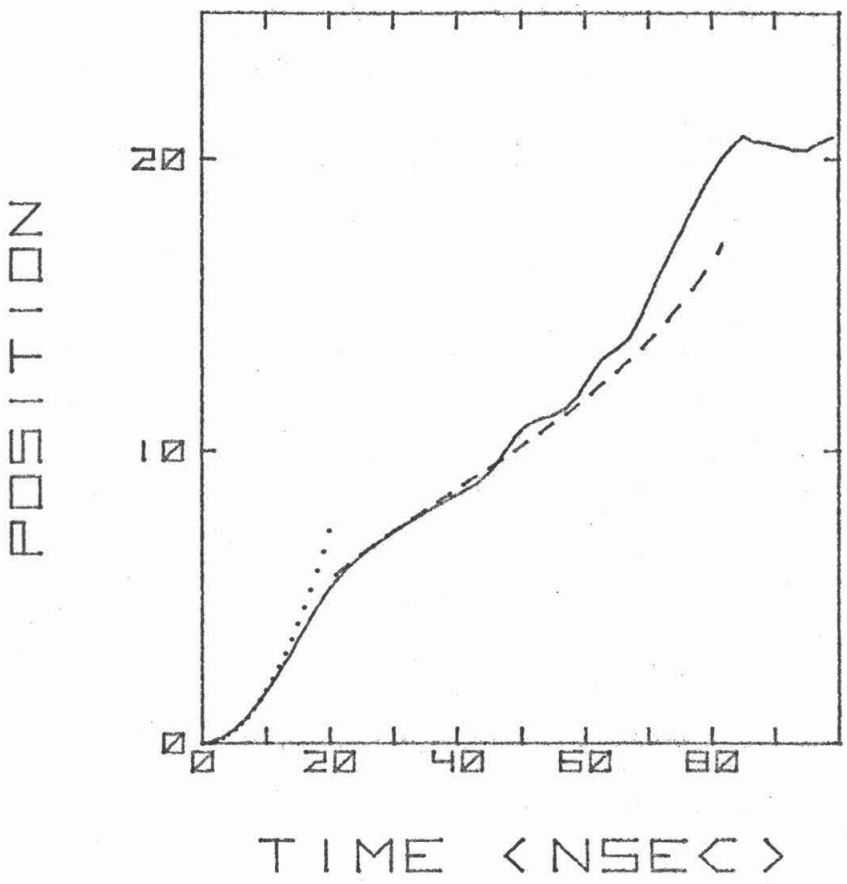

Fig. 2.4.5. Calculated Wall Position, q/Δ_B, from the Horizontal Bloch Line (dashed) and Simple Harmonic Oscillator (dotted) Models. The drive field conditions and material parameters are the same as those used in Fig. (2.4.1-4). For reference, the average wall position from Fig. (2.4.1) is shown as a solid curve.

motion represents sequential rotation between opposite wall chiralities. Hence, the analogy drawn earlier between static HBL's and static domain walls also applies when these structures are moving.

Results from this numerical solution of the full equations of motion may be compared with the more approximate analysis presented in Sec. 2.3. Fig. (2.4.5) compares the motion expected from the harmonic oscillatory model (dotted) and the HBL model (dashed) with the average wall motion obtained in the numerical solution (solid). It was shown earlier that the wall has a relatively simple wall structure during the first few nanoseconds of motion, so that the initial response should resemble a wall moving with a constant effective mass. In the presence of a constant restoring force, the initial response should resemble simple harmonic motion [see Eq. (2.2.18)]. However, in the example shown in Fig.[2.4.5], the restoring force is zero, and $\dot{q}/\mu$ is never significant, so that the initial response is parabolic, $q(t) = H_a M_s t^2/m$, rather than sinusoidal. The mass used in this expression, $m = 1.75\ m_D$, is just the effective mass of the static twist structure that was used as initial conditions in the numerical solution. It can be seen that these two curves are in good agreement for the first few nanoseconds. As expected, deviations occur after about t = 16 nsec, when the HBL begins to affect the wall motion.

The equations of motion from the HBL model, Eqs. (2.3.29a,b), have been solved numerically for the same conditions, and the results are shown in Fig. (2.4.5) as a dashed curve. Since the model assumes that the HBL is always present, the calculation begins at t = 16 nsec, with an HBL located at the upper critical point, and ends at t = 79 nsec, when the HBL reaches the lower critical point. The position of the dashed curve has been adjusted to match the solid curve at t = 16 nsec. It can be seen that the two solutions are in good agreement up to about t = 45 nsec. In the time interval, $45 < t < 65$ nsec, the solid curve shows two bumps which are not seen in the HBL model. However, agreement is not expected in this region, since the bumps are due to vibrations of the wall surface that are not treated by the HBL model. As the HBL approaches the lower surface, for $t \gtrsim 60$ nsec, the HBL model underestimates the actual wall velocity. This is due to the assumption made in the HBL model, that the field gradient $\partial H_s/\partial z$ is uniform across the HBL width. As can be seen in Fig. (2.3.1), the surface fields from zero-bias stripes are fairly uniform near the film center. Hence, the approximation is most yalid when the HBL is in this region. The surface fields are quite non-uniform near the film surfaces, so the model does not accurately describe wall motion when the HBL is in this region. The average field gradient on the HBL is somewhat higher than the value assumed by the model, $\partial H_s/\partial z\Big|_{z=z_L}$, so that the actual wall velocity is higher [see Eq. (2.3.29b)]. Since the HBL reaches the lower critical point

at about the same time in both solutions, this comparison shows that the HBL model accurately describes the motion of the HBL.

The numerical solution of the full equations of motion may also be compared with other aspects of the discussion in Sec. 2.3. Momentum conservation requires that $\langle\dot{\phi}\rangle$ be proportional to H_z regardless of the internal wall structure [see Eq. (2.3.13)]. Since H_z is constant in the numerical solution, $\langle\dot{\phi}\rangle$ increases linearly with time [see Fig. (2.4.1)], and the slope, $3.59\times10^{7}\,\mathrm{sec}^{-1}$, is in good agreement with the expected value, $\gamma H_z = 3.70\times10^{7}\,\mathrm{sec}^{-1}$. The 2% difference between these values is attributed to the effects of damping. The HBL widths given in Eq. (2.3.25) have been compared with the structures shown in Figs. (2.4.2-3). Since internal vibrations produce significant changes in $\phi(z)$, an accurate comparison can only be made with structures for $t < 50$ nsec. While the HBL width shown in these structures varies by nearly 40%, the average difference between the HBL width shown here and W_L is only 4%, so that the HBL width is given accurately by Eq. (2.3.25). The wall curvature q_{zz}^{-1} has been calculated numerically from the structure shown in Fig. (2.4.2) for $t = 30$ nsec, and the results have been compared with q_{zz}^{-1} from Eq. (2.3.26). The average radius of curvature in the numerical solution, 3.8 μm, is in good agreement with the value given by the HBL model, 4.0 μm. The peak velocity from Eq. (2.3.28), $v_p = 19.6$ m/sec, is in good agreement with the maximum velocity attained during the initial response shown in Fig. (2.4.1), $\langle\dot{q}\rangle = 21$ m/sec

at t = 16 nsec. According to the HBL model, the wall should also reach this velocity when the HBL reaches the lower critical point, but the maximum velocity attained in the numerical solution, $\langle \dot{q} \rangle$ = 25.5 m/sec at t = 76 nsec, is about 30% higher than v_p. This discrepancy is due to the approximation used in the HBL model to estimate $\partial H_s/\partial z$. The saturation velocity given in Eq. (2.3.30), v_o = 8.2 m/sec, is much smaller than the average velocity shown in Fig. (2.4.1), 11.5 m/sec. This difference is due in part to the fast initial response found in the numerical solution. Since the HBL model assumes that an HBL is always present, it is more appropriate to compare v_o with the average velocity during the interval when an HBL is actually present, 16 < t < 76 nsec. The average velocity during this interval, 9.4 m/sec, is only 15% higher than v_o.

Section 2.5. Conclusions

In treating domain wall motion in magnetic bubble materials, both the wall center q and azimuthal angle ϕ must be allowed to vary with position along the wall surface. In the more approximate HBL model, only the azimuthal angle varies with position, while the wall surface remains flat, and perpendicular to the film surfaces. This model is able, within limits, to account for some properties of wall

motion. However, numerical solutions of the full equations of motion show that changes in the wall surface can also be important. For example, HBL nucleation, which cannot be treated in the HBL model, results from the formation of a bulge in the wall surface. The bulge accompanies the HBL as it moves along the wall, and supplies the added rotation necessary to propagate the HBL. Internal vibrations are excited, when the bulge is reflected from the film surface. Because of the nonuniform wall mass density, these vibrations produce small fluctuations in the average wall position. When the HBL disappears at one of the film surfaces, the wall section in the same region travels backwards. As a result, the average wall position remains stationary during punch-through. Hence, while the HBL model is useful in describing some aspects of twisted wall motion, a complete analysis of horizontal Bloch line dynamics requires that variations in wall surface also be taken into account. This is accomplished here by solving the equations of motion numerically.

References

1. L. Landau, and E. Lifschitz, Physic. A. Sowjetunion 8, 153 (1935).
2. W. F. Brown, Micromagnetics, (Interscience, New York, 1963).
3. See, for example, L. I. Schiff, Quantum Mechanics,(McGraw Hill, New York, 1968).
4. T. L. Gilbert, Phys. Rev. 100, 1243 (1955). This is an abstract only. A short discussion of this work is given in reference 2.
5. See, for example, H. Goldstein, Classical Mechanics, (Addison-Wesley, Reading, 1965).
6. See, for example, Jon Mathews, and R. L. Walker, Mathematical Methods of Physics (W. A. Benjamin, Inc., Menlo Park, 1970).
7. L. Neél, Compt. Rend. Acad. Sci. Paris 241, 533 (1955).
8. L. R. Walker, unpublished. An account of this work is given in J. F. Dillion, Magnetism, ed. Rado and Suhl (Academic Press, New York, 1963).
9. H. C. Bourne, and D. S. Bartran, IEEE Trans. MAG-8, 741 (1972).
10. N. L. Schryer, and L. R. Walker, J. Appl. Phys. 45, 5406 (1974).
11. W. F. Brown and S. Shtrikman, Phys. Rev. 125, 825 (1962).
12. B. Carnahan, H. A. Luther, and J. O. Wilkes, Applied Numerical Methods (John Wiley and Sons, New York, 1969).
13. J. W. F. Dorleijn, E. F. Druyvesteyn, G. Bartels, and W. Tolksdorf, Philips Res. Repts. 28, 133 (1973).

14. S. Chikazumi, Physics of Magnetism (John Wiley and Sons, New York, 1964).

15. A. Hubert, Theorie der Domänenwände in Geordneten Medien, Lecture Notes in Physics, 26 (Springer Verlag, Berlin, 1974).

16. J. C. Slonczewski, Intern. J. Magnetism 2, 85 (1972).

17. A. Emura, T. Fugii, S. Shiomi, and S. Uchiyama, IEEE Trans. MAG-13, 1169 (1977).

18. W. Döring, A. Naturforsch. 3a, 373 (1948).

19. C. Kittel, and J. D. Galt, Solid State Physics, ed. F. Seitz and D. Turnbull (Academic Press, New York, 1956).

20. G. T. Rado, Phys. Rev. 83, 821 (1951).

21. E. Schlöman, J. Appl. Phys. 44, 1837 (1973).

22. E. Schlöman, J. Appl. Phys. 45, 369 (1974).

23. Alex Hubert, J. Appl. Phys. 46, 2276 (1975).

24. E. Schlöman, J. Appl. Phys. 44, 1850 (1973).

25. A. A. Thiele, Bell Syst. Tech. J. 48, 3287 (1969).

26. W. J. DeBonte, IEEE Trans. MAG-11, 3 (1975).

27. J. C. Slonczewski, J. Appl. Phys. 44, 1759 (1973).

28. E. Schlöman, AIP Conf. Proc. 10, 478 (1972).

29. F. B. Hagedorn, J. Appl. Phys. 45, 3129 (1974).

30. B. E. Argyle, J. C. Slonczewski, and A. F. Mayadas, AIP Conf. Proc. 5, 175 (1971).

31. F. H. de Leeuw, IEEE Trans. MAG-14, 596 (1978).

Chapter 3

HBL Motion in a Low-loss Magnetic Bubble Material

The bias pulse technique [1,2,3] has been used to investigate domain wall motion in magnetic bubble materials. Because the equilibrium sizes of bubble and stripe domains depend on the magnitude of the external bias field, a bias field pulse can be used to produce a step change in equilibrium wall position. As the wall moves to its new equilibrium position, its response is measured by using either the optical sampling [1], photometric [2] or stroboscopic method [4]. The response can also be measured indirectly by using the bubble collapse method [5], but in situations where the response is relatively complex this method can give erroneous results. Other techniques have also been used to investigate wall motion. In wall resonance [6], the equilibrium position varies sinusoidally with time, and the amplitude and phase of the wall response are measured as a function of the excitation frequency. However, the resonance curves are usually quite complicated and difficult to interpret in terms of the underlying mechanical properties of the domain wall. Gradient propagation [7] of bubble domains has also been used because it more closely reproduces the conditions found in bubble devices. In this technique, bubbles translate along a bias field gradient that is produced by a pair of current conductors. Unfortunately, results from this method are com-

plicated by nonuniform drive field conditions and by the presence of vertical Bloch line structures. Of the experimental techniques currently in use, the bias pulse technique provides the simplest means of studying wall motion in bubble materials.

Wall oscillation is observed during bias pulse experiments in some low-loss materials. In most materials, the wall stops when it reaches its new equilibrium position, and no inertial effects are observed [1]. However, in some low-damping materials [8-11] the wall moves well past equilibrium, and oscillates around this position with decreasing amplitude until the oscillations damp out. Oscillations have been found in bubbles [9], stripe domains [11-13] and in isolated domain walls [10,14]. The shape and frequency of these oscillations depend on the internal wall structure, while the damping rate depends on the energy dissipated by the wall as it moves through the material. Wall oscillation is used here as a sensitive means of observing the effects of internal wall structure on domain wall motion.

Wall motion will be analyzed by using the model presented in Ch. 2. In comparing experimental results with those from the model, it is necessary to make several simplifying assumptions. Bubble and stripe walls are treated as isolated, straight domain walls. It is assumed that internal structures are uniform along the length of the wall, and that nonuniform twist structures, such as vertical Bloch lines, are not present. The restoring forces produced by the surrounding domains are taken into account with a constant effective

field gradient H' [see Eq. (2.2.18)]. In principle, this gradient may be calculated from the static properties of bubble and stripe domains, but it is usually more accurate to calculate it from the measured change in equilibrium wall position, and from the bias pulse amplitude. Surface demagnetizing fields, which produce the horizontal twist structures, are taken into account, but the slight variations in these fields with domain size are neglected. Hence, the fields for a 4.7 μm bubble and zero-bias stripe domains will be used.

A sampling optical microscope system, which is described in detail in Appendix B, was used to investigate wall oscillation. In this system, a pulsed dye laser and polarizing microscope are used to obtain transient pictures of isolated bubble domains as they respond to a bias field pulse. The laser, which illuminates the sample with a 10 nsec light pulse, is always triggered at a fixed time relative to the bias field pulse. The relative time can be adjusted manually, or automatically incremented after each pulse. For convenience, the origin, t = 0, is defined as the time when the pulse reaches half of its maximum amplitude. The Faraday effect is used to produce real images of the domains on the target of a TV camera. These images are then recorded on video tape. Later, the transient bubble radius is measured frame by frame with a computer controlled digitizer. The resolution in wall position is limited by diffraction effects to about 0.2 μm. If the motion is reproducible from one pulse to the next, the wall motion is obtained by

plotting the sampled bubble radius as a function of the relative time.

A photometric technique was sometimes used in parallel stripe domains to obtain greater spatial resolution. Instead of measuring wall position from transient pictures, the wall position is determined by measuring image intensity. An electrical signal proportional to the average intensity over the field of view is obtained from a photodiode. The signal is amplified and averaged over many pulse repetitions by a lock-in amplifier. Since the changes in image intensity are proportional to changes in stripe width, the output from the detector is directly proportional to wall displacement. The wall motion is displayed by plotting the output signal as a function of the relative time between the bias pulse and laser flash on an x-y chart recorder. This method was calibrated by comparing results with those obtained by optical sampling under identical circumstances. The effective spatial resolution obtained here, 0.03 μm, is nearly an order of magnitude better than with the optical sampling method. Since the image intensity is sensitive to domain configuration, it is necessary to keep the configuration constant during the experiment. For this reason, the method is usually used on stripe domains[2,11,12,15] and isolated straight walls [10], though the method can also be used with isolated bubble domains by taking advantage of laser heating effects [9]. This method is described in more detail in Appendix B.

The results reported here are for a single, very low-loss magnetic bubble material. The material parameters are shown in Table 3.I. By concentrating on a single material under a variety of experimental conditions, a more thorough understanding of wall motion can be achieved. However, many of these results have also been confirmed in more conventional materials. These results will be indicated by reference to the literature. The first three material parameters, γ, $H_k - 4\pi M_s$, and α, were obtained from resonance measurements, while the rest come from measurements of static domains. The uncertainty in H' for bubbles represents the variation over the range of stable bias fields. The uncertainty at a single static bias field is typically 0.1 Oe/μm. There is much less variation in H' in stripe domains. Derived parameters, along with their definitions, are listed in the second part of the table. Note that the uncertainty in some parameters, particularly those involving α, can be quite large, because the uncertainty in α is nearly 30%.

The investigation of horizontal Bloch line motion in magnetic bubble materials is divided into three parts. In Sec. 3.1, it is shown that the presence of horizontal Bloch lines produces the unusual dynamic behavior found during wall oscillation. In Sec. 3.2, it is shown that HBL punch-through produces a series of transitions to overdamped motion, which are accompanied by changes in wall chirality. Finally, wall oscillation in the presence of the external in-plane fields is investigated in Sec. 3.3. For sufficiently

TABLE 3.I

Material Parameters

γ	$= 1.85 \pm 0.02 \times 10^{7}$ Oe^{-1} sec^{-1}
$H_k - 4\pi M_s$	$= 1005 \pm 10$ Oe
α	$= 0.0032 \pm 0.0009$
$4\pi M_s$	$= 95 \pm 3$ Oe
h	$= 4.1 \pm 0.2$ μm
λ	$= 0.30 \pm 0.02$
ℓ	$= 1.23 \pm 0.14$ μm
H_k	$= 1100 \pm 13$ Oe
H'	$= 2.2 \pm 0.3$ Oe/μm (bubbles)
H'	$= 6.4 \pm 0.4$ Oe/μm (stripes)

Derived Parameters

Q	$= H_k/4\pi M_s$	$= 11.6 \pm 0.5$
K_u	$= H_k M_s/2$	$= 4158 \pm 170$ erg/cm^3
Δ_B	$= \ell/2Q$	$= .053 \pm 0.008$ μm
A	$= \Delta_B^2 K_u$	$= 1.17 \pm 0.40$ erg/cm
σ_B	$= 4\pi M_s^2 \ell$	$= 0.088 \pm 0.015$ erg/cm^2
μ	$= \gamma\Delta_B/\alpha$	$= 306 \pm 140$ m/sec-Oe
V_w	$= 2\pi M_s \gamma \Delta_B/(1+\frac{1}{2Q})$	$= 44.6 \pm 8$ m/sec
V_p	$= 24\gamma\Delta_B\sqrt{A}/h$	$= 19.6 \pm 7$ m/sec
v_o	$= 4\sqrt{2\pi}\gamma\Delta_B\sqrt{A}/h$	$= 8.2 \pm 3$ m/sec
H_w	$= 2\pi M_s \alpha$	$= 0.15 \pm 0.05$ Oe
H_p	$= 24\alpha\sqrt{A}/h$	$= 0.064 \pm 0.03$ Oe
m_D	$= (2\pi\gamma^2\Delta_B)^{-1}$	$= 8.8 \pm 1.5 \times 10^{-11}$ gm/cm^2

large in-plane fields, the dynamic wall structure is essentially one-dimensional, resulting in the sinusoidal oscillations expected from the harmonic oscillator model. The onset of unusual dynamic behavior at reduced in-plane fields is then identified with HBL nucleation.

Section 3.1. Wall Oscillation and HBL Motion

Past studies indicate that the dynamic properties associated with wall oscillation are quite unusual. In the simplest approximation, the harmonic oscillator model, a wall with a one-dimensional structure oscillates with a constant frequency, ν, which is characteristic of the material. However, attempts to model wall oscillation as simple harmonic motion [10,16] have failed for two reasons. First, the experimental frequency is usually many times lower than the value expected from Eq. (2.2.19), and second, the frequency changes rapidly with the bias pulse amplitude. Instead, there is some evidence [9,11,14,17], which suggests that the wall velocity is saturated, i.e., independent of the instantaneous drive field. It has been suggested that this behavior is due to the presence of hard wall sections, containing many vertical Bloch lines [10], or multiple horizontal Bloch lines [11], but no quantitative analysis has been reported. The purpose here is to investigate wall oscillation in bubble domains, and to show that the unusual behavior is due to the

presence of a single HBL.

An example of wall oscillation during radial expansion is shown in Fig. (3.1.1). Here, the sampled bubble radius is plotted as a function of time in response to a 2.13 Oe step change in bias field. When the pulse is applied at t = 0, the bubble expands from its initial equilibrium radius, 4.7 μm, toward its new equilibrium radius, 5.7 μm. The wall moves well beyond equilibrium and oscillates with decreasing amplitude until the oscillations damp out. Similar behavior is also seen at the end of the bias pulse (not shown) when the bubble returns to its original size. Several features indicate that this is not simple harmonic motion. The wall velocity is nearly constant during the initial expansion at 5.0 m/sec. The velocities during the subsequent return and second expansion are also constant, with values of 4.1 m/sec and 5.0 msec respectively. The frequency associated with the first half-period, 1.6 MHz, is much smaller than the value predicted by the harmonic oscillator model, 9.8 MHz. It can also be seen that the frequency increases as the size of the oscillations decrease; the frequencies associated with the second and third half-periods, 2.0 MHz and 3.2 MHz, are much higher. Immediately after the pulse is applied, the bubble expands rapidly for the first 20 nsec, and then assumes a lower, constant velocity. The wall moves backwards slightly, just before it reaches the first extremum. This effect, which is called initial rapid motion,has been seen previously under a variety of circumstances[12,14,15,18]. This behavior is investigated in more detail in Sec. 3.3. All of these features indicate that the oscillations cannot be modelled as

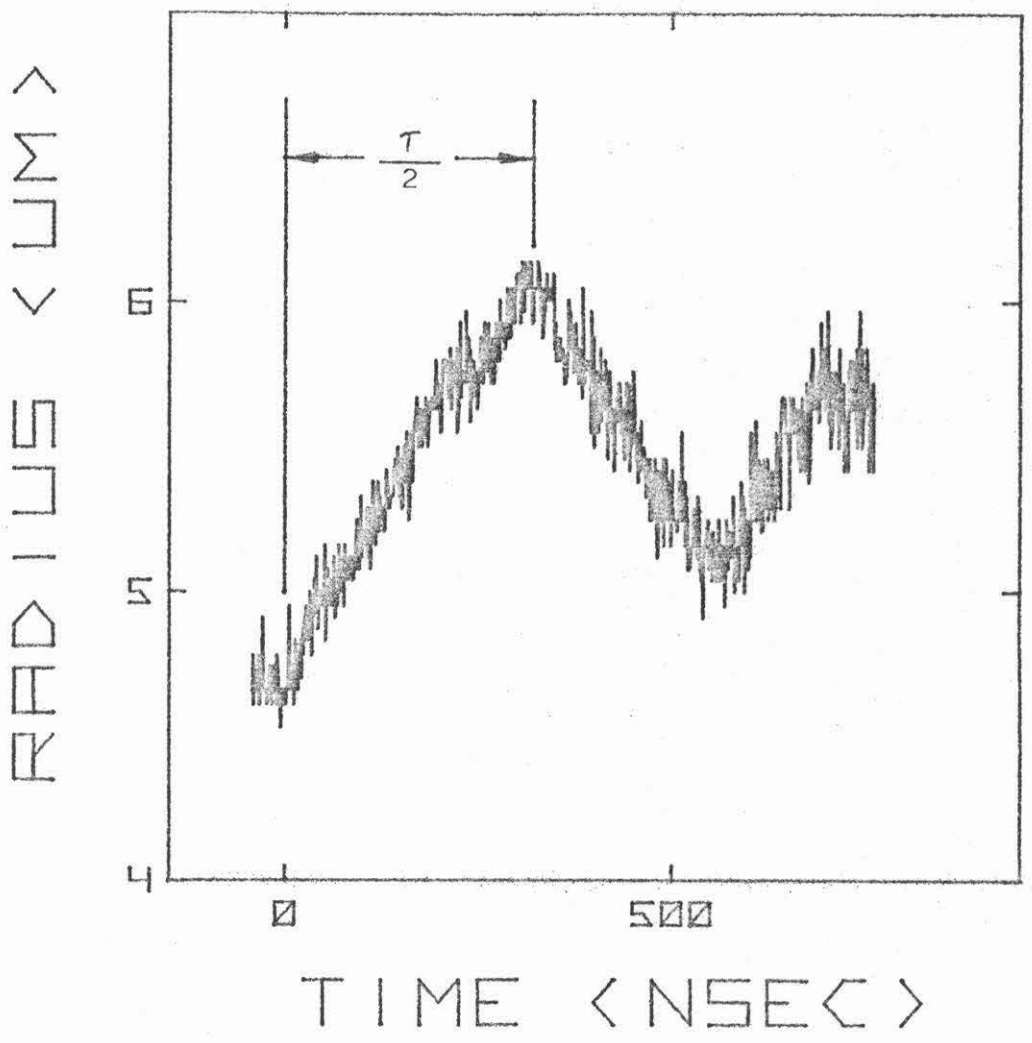

Fig. 3.1.1. Bubble Radius (μm) as a Function of Time (nsec) in Response to a 2.13 Oe Bias Field Pulse. The static bias field was 24.1 Oe. The half-period, $\tau/2$, is indicated.

simple harmonic motion.

The first half-period, $\tau/2$, has been measured as a function of pulse amplitude, and the results are shown in Fig. (3.1.2). Measurements were made by using both expanding (+) and collapsing (□) bias field pulses. To eliminate possible bubble size effects, the static bias field H_B was adjusted so that the average bias field, $H_B+H_a/2$, was constant at 23.5 Oe. The half-period was determined by manually adjusting the laser position until the first extremum was located. The relative time between the beginning of the bias pulse and the laser flash is then $\tau/2$. It can be seen that $\tau/2$ increases rapidly with increasing H_a. Beginning at H_a = 1.0 Oe, the smallest amplitude for which oscillations can be seen, $\tau/2$ increases from 130 nsec to 280 nsec at H_a = 2.0 Oe. The oscillation frequency is not constant, as would be expected from the harmonic oscillator model, but increases with bias pulse amplitude.

These results can be analyzed by assuming that the wall velocity is constant, $\langle\dot{q}\rangle = v_s$ (19). With this assumption, the average value of $\dot{\phi}$ may be written from Eq. (2.3.12b) as

$$\langle\dot{\phi}\rangle = \gamma[H_z - H_{sv}] \quad , \tag{3.1.1}$$

where $H_{sv} = v_s/\mu$ is an effective damping field. Since v_s is less than 8 m/sec, H_{sv} is less than 0.03 Oe. Equation (3.1.1) may be integrated to obtain $\langle\phi\rangle$ as a function of time:

$$\langle\phi(t)\rangle = \gamma \int_0^t dt' \, [H_z(t') - H_{sv}] \quad . \tag{3.1.2}$$

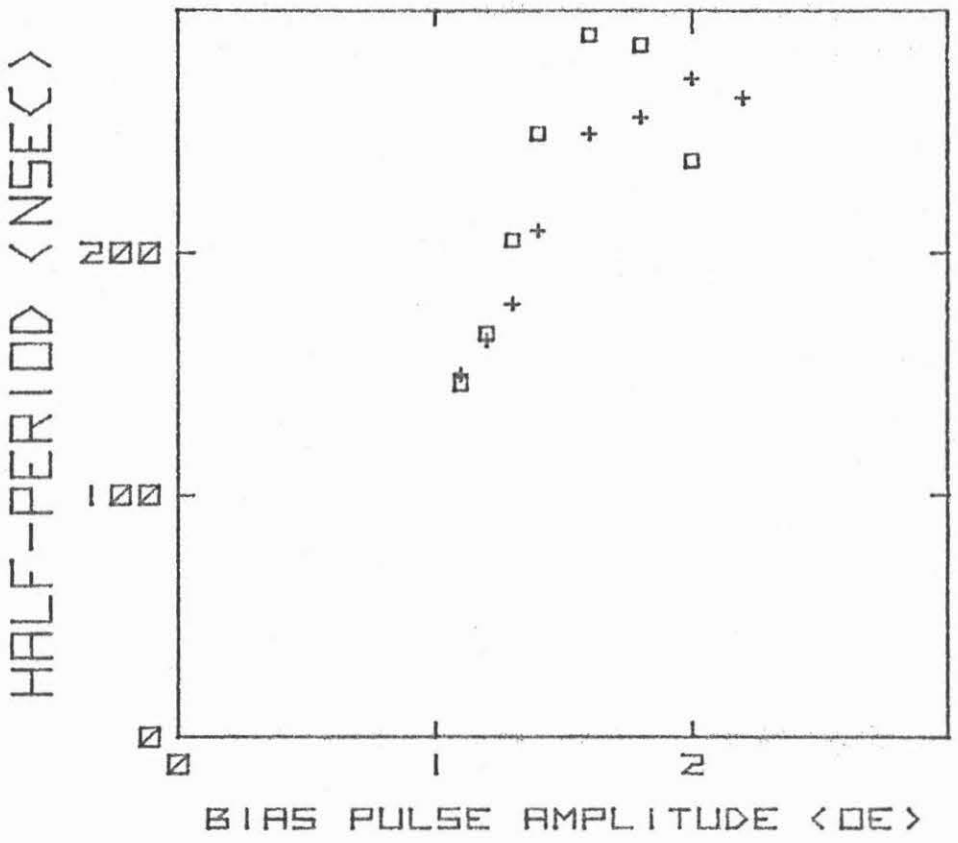

Fig. 3.1.2. The Half-Period, $\tau/2$ (nsec), as a Function of Bias Pulse Amplitude (Oe). Results are shown for both expanding (+) and collapsing (□) motion. The average bias field, $H_B + \frac{1}{2}H_a$, is held constant at 23.5 Oe. Each point, which represents the average value of 6 experiments, has an uncertainty of about 20 nsec.

Since the bias pulse rise time is short compared with $\tau/2$, the pulse shape may be approximated by a step function, so that $H_z(t')$ is given by $H_z(t') = H_a - H'v_s t'$. Under this assumption, $\langle\phi(t)\rangle$ is a parabolic function of time. When the pulse is applied, $\langle\phi\rangle$ increases from zero, and reaches a maximum value of

$$\langle\phi\rangle_{max} = \frac{\gamma}{2v_s H'} (H_a - H_{sv})^2 \quad . \tag{3.1.3}$$

It then decreases, and reaches zero again at a time,

$$\frac{\tau}{2} = \frac{2(H_a - H_{sv})}{v_s H'} \quad . \tag{3.1.4}$$

With a constant wall velocity, the half-period increases linearly with H_a. It must be emphasized that this simplified model does not indicate why the velocity is constant. It is only a simple way of calculating the internal rotation based on the experimental fact that the wall velocity is approximately constant.

Average velocities obtained from measurements of $\frac{\tau}{2}$ have been compared with more direct measurements, and the results are shown in Fig. (3.1.3). Here, the velocities are plotted as a function of H_a. Note the suppressed zero in the pulse amplitude scale. Points obtained from radius vs time data similar to those shown in Fig. (3.1.1) are indicated by □ , while points calculated from $\frac{\tau}{2}$ vs H_a data by using Eq. (3.1.4) are indicated by +. The point ■ was calculated by using the model from Ch. 2 and will be discussed later. The theoretical value of v_o from Eq. (2.3.30) and the minimum velocity v_{min}, which occurs when the HBL reaches the film center, are

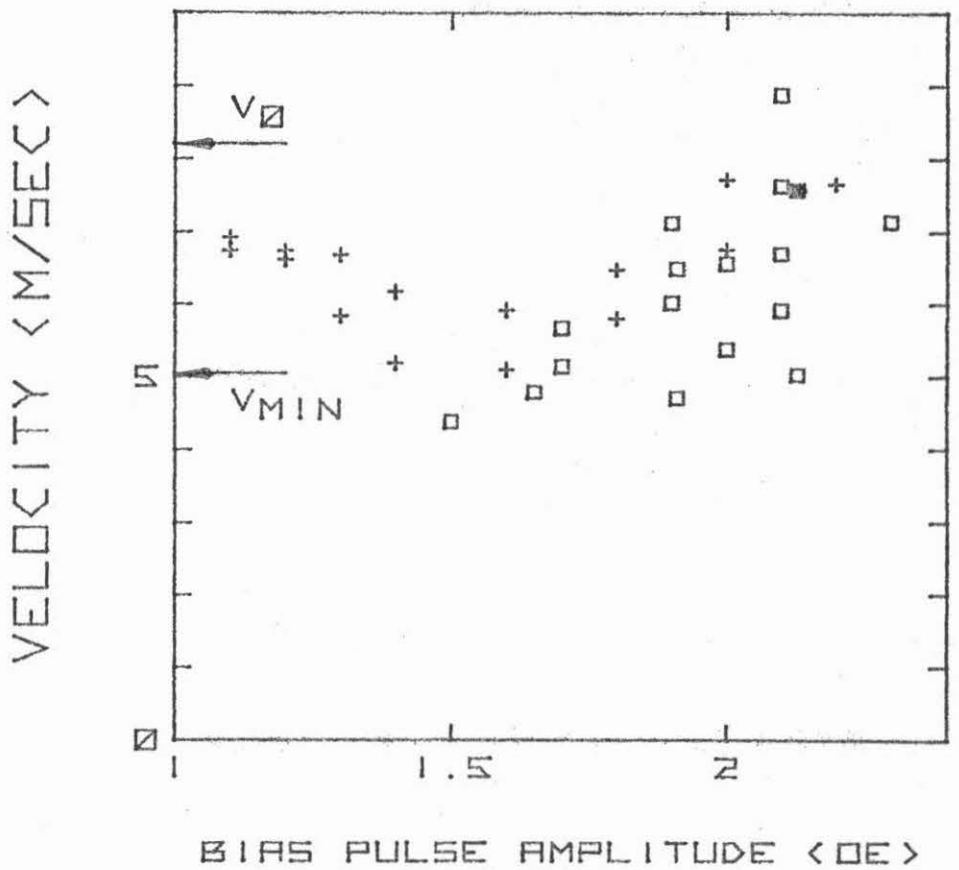

Fig. 3.1.3. The Average Wall Velocity (m/sec) as a Function of Bias Pulse Amplitude (Oe). The points □ were obtained from direct measurements, while the points + were obtained from measurement of $\tau/2$. The uncertainty in each velocity is about 1 m/sec. The point ■ was calculated by using the theoretical model presented in Ch. 2. The theoretical value of V_0 and the minimum velocity V_{min} for bubble domains are shown for comparison.

indicated. The uncertainty in the data is about 1 m/sec. It can be seen that the velocities measured by using these two different techniques agree within experimental error. It can also be seen that the average velocity is not strictly constant, but varies slightly with pulse amplitude. The velocity is about 7.0 m/sec at H_a=1 Oe, and decreases to about 5.5 m/sec at H_a=1.5 Oe. It then increases, reaching 7.5 m/sec at H_a=2.2 Oe. Measurements cannot be performed at higher pulse amplitudes due to HBL punch-through.

The unusual dynamic behavior found during wall oscillation results from the presence of an HBL during wall oscillation. Before the bias pulse, the stationary wall has a simple twist structure like the one shown in Fig. (2.3.2) as a solid curve. When the pulse is applied, the wall accelerates rapidly while maintaining this structure. This results in the initial rapid motion shown in Fig. (3.1.1). Soon, however, an HBL is formed and moves toward the film center. The velocity drops and remains roughly constant. When the bubble reaches its new equilibrium radius at 5.7 μm, the effective drive field changes sign, so that $\langle\dot{\phi}\rangle$ becomes negative, and the HBL moves back toward the original critical point. When the HBL reaches this point, it disappears, leaving the wall with a static twist structure. The effective drive field is negative, so that the wall moves back toward equilibrium and a second HBL is formed at the opposite critical point. Each time the wall reverses direction, an HBL of the opposite sense is formed, and the process is repeated.

Oscillation results from a redistribution of energy within the magnetic system. In the limit $\alpha \to 0$, the total energy, which is a con-

stant of the motion, is divided between kinetic energy, which is stored in the HBL, and potential energy due to the external field, $-2M_s H_z h\langle q\rangle$. Just after the bias pulse is applied, the energy is all in the form of potential energy. Since H_z is positive, $\langle\phi\rangle$ must increase [see Eq. (2.3.13)]. As $\langle\phi\rangle$ increases, an HBL forms, and absorbs potential energy from the external field. This causes the wall to move forward until, when the wall reaches its new equilibrium position (H_z=0), the energy is all stored as kinetic energy. If the wall were to move backward slightly, H_z would be positive again, and $\langle\phi\rangle$ would increase. This would increase the HBL energy at the expense of potential energy, and the wall would return to equilibrium. However, if the wall moves forward slightly, H_z is negative, and $\langle\phi\rangle$ decreases. The HBL energy decreases,and the wall moves forward,which further decreases H_z. Hence, a wall containing an HBL at equilibrium is unstable, and must move forward even though H_z becomes negative. As $\langle\phi\rangle$ decreases, the HBL energy decreases until, when the wall reaches its first extremum, the energy is all stored as potential energy, and the wall is left with its original static twist structure. Since H_z is still negative, $\langle\phi\rangle$ decreases and becomes negative. A second HBL is formed at the opposite critical point, and the process is repeated. In the presence of damping, energy is slowly dissipated, and the oscillations damp out. Oscillation occurs only if the HBL is stable during the process. If, as in the case of HBL punch-through, it becomes unstable, the HBL energy is immediately dissipated, and the wall does not overshoot equilibrium. This process is described further in Sec. 3.2.

The equations of motion have been solved numerically for the conditions associated with Fig. (3.1.1), and the results are shown in Fig. (3.1.4). Here, the average wall position <q> is plotted as a function of time. The rise time of the 2.13 Oe bias field pulse was approximated by a 20 nsec ramp with its center at t = 0. The averaging effects of the laser flash were simulated by passing the results through a 10 nsec averaging window. The conditions considered here are somewhat different than those considered in Sec. 2.4. There, a constant drive field of 2 Oe was used, while here, the drive field decreases as the wall moves toward equilibrium. In general, the motion of the HBL here is much slower due to the smaller drive fields. The calculated motion closely resembles the experimental data shown in Fig. (3.1.1). The calculation shows that the initial rapid motion, which can be seen in both figures, represents wall motion before an HBL is formed. After the initial response, an HBL structure, like those shown in Fig. (2.4.2), is formed. The presence of the HBL produces a relatively low, constant wall velocity of about 7.5 m/sec. The irregular motion shown in the calculation is produced by internal wall vibrations like those described in Sec. 2.4. It is tempting to associate the reverse motion in the interval, 153 < t < 174 nsec, with a similar feature in the data; however, it is an artifact of the numerical technique since it does not appear in the Crank-Nicolson solutions of the same problem. Though the average velocity is 35% higher than the value shown in Fig. (3.1.1), it is in good agreement with other measurements shown in Fig. (3.1.3), where the calculated velocity is indi-

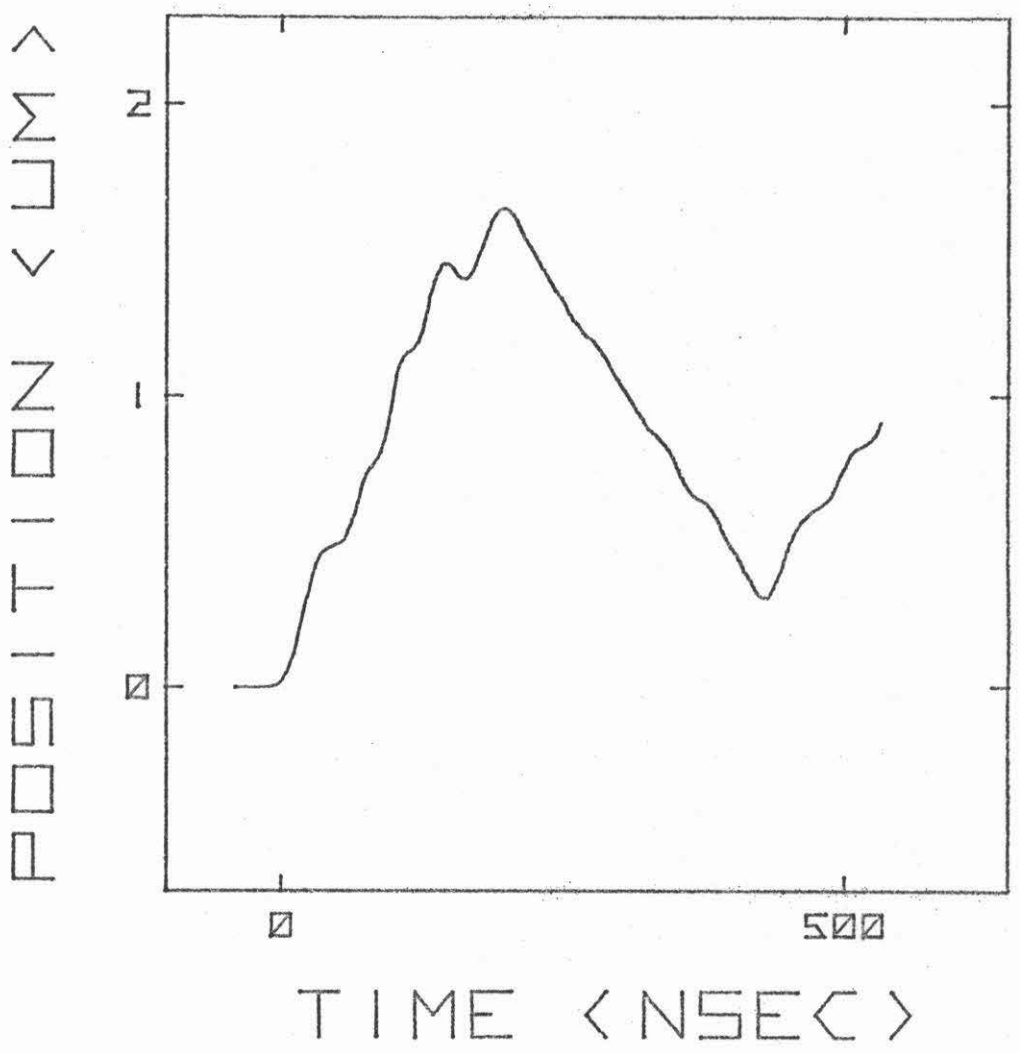

Fig. 3.1.4 The Calculated Average Wall Position, <q> (μm), as a Function of Time (sec) for the same experimental conditions shown in Fig. (3.1.1).

cated by ■. When the wall passes equilibrium, at $\langle q \rangle = 0.96$ μm, the drive field becomes negative, and the HBL moves back toward the film surface where it originally formed. As the wall reaches its first extremum, at t = 207 nsec, the HBL disappears, and the wall structure resembles the original static structure. The drive field at this point is -1.5 Oe, so the wall moves back toward equilibrium. A second HBL is formed at the opposite film surface, and the process is repeated. Since the wall vibrations are still present, initial rapid motion is not observed.

The small changes in average velocity shown in Fig. (3.1.3) can be explained by considering HBL motion. The instantaneous wall velocity depends on the HBL position [see Fig. (2.3.5)], so that the average wall velocity depends on how far the HBL penetrates into the film. For small pulse amplitudes, only a small HBL is formed near the film surface, and the average wall velocity is relatively large. As the pulse amplitude is increased, the HBL approaches the film center, where the instantaneous wall velocity is smaller. This causes a slight drop in average velocity, which can be seen in Fig. (3.1.3) in the region $1.0 < H_a < 1.7$ Oe. The value of $\langle \phi \rangle_{max}$ corresponding to this velocity is 0.68π [see Eq. (3.1.3)]. This shows that the minimum average velocity occurs when the HBL penetrates just beyond the film center. For higher amplitudes, the HBL approaches the opposite film surface, and the instantaneous velocity increases. This produces an increase in the average velocity, which can be seen in the region $1.7 \text{ Oe} < H_a < 2.5$ Oe. For larger amplitudes than those used

here, the HBL reaches the opposite surface and punches through.

Section 3.2. Horizontal Bloch Line Punch-Through

Horizontal Bloch line punch-through takes place for sufficiently large pulse amplitudes. If the pulse amplitude is somewhat larger than those used in Sec. 3.1, the HBL reaches the opposite critical point before the wall reaches its new equilibrium position. When the HBL punches through, the momentum and energy stored in the HBL are dissipated, and the wall is left with a simple, static twist structure, but with the opposite sense of chirality. Some evidence for momentum dissipation has been reported by de Leeuw and Robertson [10,14]. They found large wall oscillations at some pulse amplitudes, while for larger amplitudes, oscillations were completely absent; however, this transition to overdamped motion was not investigated further. Independent evidence for chirality changes has been obtained by using an indirect, automotion technique [20,21]. This technique was used to investigate changes in bubble chirality as a function of bias pulse rise time with the pulse amplitude held constant. Changes in chirality were analyzed in terms of HBL punch-through, but poor quantitative agreement was found for rise times less than 100 nsec. Hence, while there is some experimental evidence for momentum dissipation and for changes in wall chirality, the relationship between these two phenomena has not been established. The purpose here is to investigate transitions to overdamped motion and chirality changes in the same material, and to show that these two related effects are, in fact, due to HBL punch-through.

Transitions to Overdamped Motion

Wall oscillations have been measured during radial expansion, using larger pulse amplitudes, and the results are shown in Fig. (3.2.1). Here, the sampled bubble radius is plotted as a function of time with pulse amplitude as a parameter. Each point represents an average of from 3 to 5 independent measurements. In each case, the static bias field was 23.0 Oe. Two distinct types of behavior can be seen. For the case, H_a = 2.1 Oe, the bubble expands from its initial equilibrium radius, 5.0 μm, when the pulse is applied at t = 0. The wall moves past equilibrium, and large oscillations can be seen. The oscillations damp out, and the wall remains stationary at the new equilibrium radius, 6.1 μm, until the pulse ends at t = 2 μsec. Large oscillations can also be seen when the bubble returns to its original radius. These oscillations are similar to those shown in Fig. (3.1.1). Overdamped motion can be seen in the case, H_a = 4.0 Oe. When the pulse is applied, the wall moves smoothly toward equilibrium and no oscillation is observed. Similar behavior can be seen at the end of the pulse, when the wall returns to its original position.

Transitions between wall oscillation and overdamped motion can be seen for intermediate pulse amplitudes. Consider the motion at the end of the pulse. When H_a is 2.1 Oe, oscillations are present, but when H_a is increased to 2.6 Oe, overdamped motion is observed. When H_a is increased to 2.8 Oe, oscillations return. Wall oscil-

lation is also seen when H_a is 3.4 Oe, but when H_a is increased to 4.0 Oe, overdamped motion returns. Hence, two distinct transitions from oscillatory motion to overdamped motion can be seen. Two such transitions can also be seen in the motion at the beginning of the pulse; however, the pulse amplitudes at which these transitions occur are somewhat higher. Similar results have been obtained in other materials [8].

The pulse amplitude at which overdamped motion first occurs can be measured by monitoring the transient bubble size at a fixed time. With the laser flash positioned at the first extremum, which is indicated by an arrow in Fig. (3.2.1), the bubble size indicates the type of motion. If oscillation occurs, the bubble is relatively large, but if overdamped motion occurs, the bubble diameter is about 0.8 μm smaller. Measurements are performed by repeating the bias pulse experiment at a 15 Hz repetition rate. The pulse amplitude is slowly increased until size fluctuations are observed. These fluctuations represent a mixture of oscillatory and overdamped motion during different pulses. The pulse amplitude where fluctuations first occur is the transition field H_I. Above this region, all bubbles are small, and the motion is always overdamped. As H_a increases, the size increases, and oscillatory motion gradually returns, until a second transition is observed at H_{II}.

The first and second transition fields are shown in Fig. (3.2.2) as a function of static bias field. Points indicated by + are for expanding motion, while those indicated by □ are for collapsing

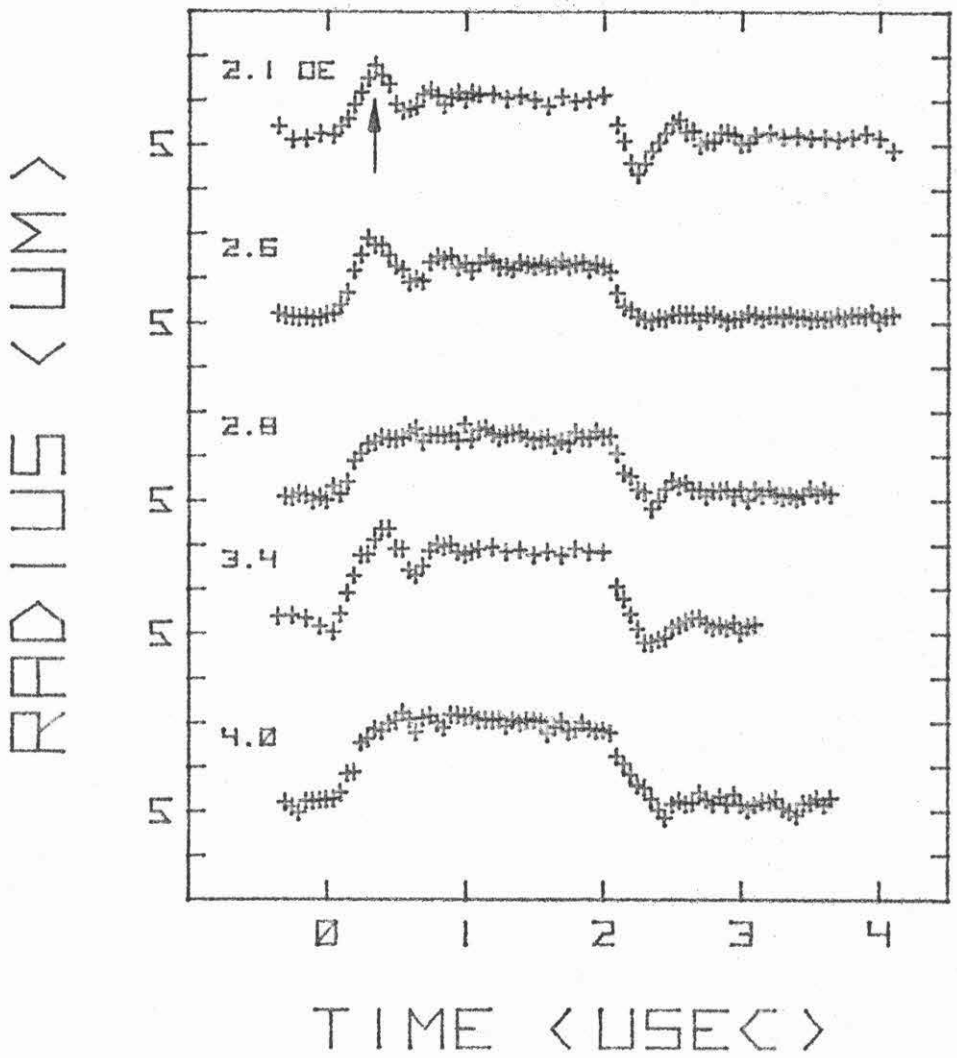

Fig. 3.2.1. Bubble Radius (μm) as a Function of Time (μsec) with Bias Pulse Amplitude as a Parameter. The pulse begins at t = 0 and ends at t = 2 μsec. The amplitude is indicated in each case. The arrow is explained in the text.

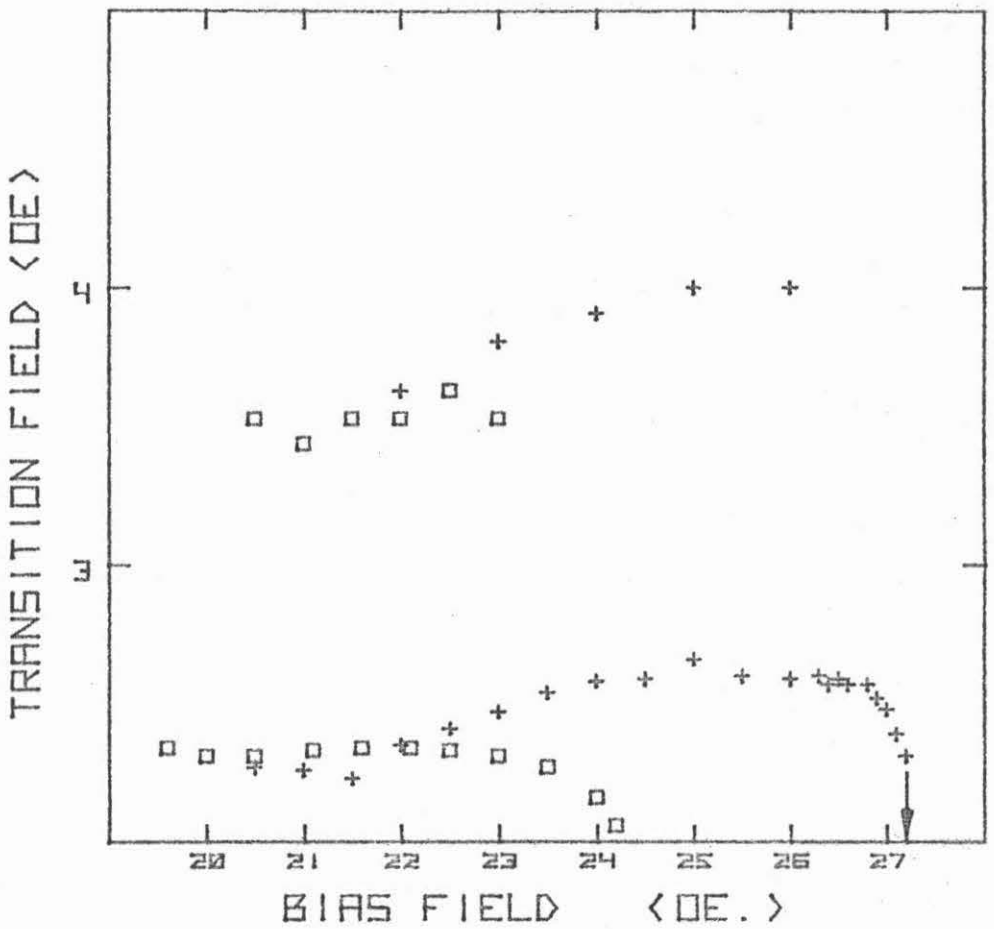

Fig. 3.2.2. First and Second Transition Fields, H_I and H_{II} (Oe), as a Function of Static Bias Field (Oe). Points indicated by + are for expanding motion, while points indicated by □ are for collapsing motion. The arrow indicates the bubble collapse field.

motion. Note the suppressed zeroes in both scales. The arrow indicates the bubble collapse field. Though the size fluctuation regions extend 0.5 Oe above H_I and H_{II}, the beginning of these transitions regions may be determined within 0.04 Oe. It can be seen that the transition fields vary slightly with bias field. The values of H_I for expanding motion are relatively small at H_B = 21 Oe, reach a maximum around H_B = 25 Oe, and then decrease sharply near the bubble collapse field. These variations are due to changes in H' with bias field. Similar variations in H_I can also be seen for collapsing motion. Note that during collapsing motion, the bias field pulse adds to the static bias field, so that bubbles collapse at a static bias field that is about 3 Oe smaller than for expanding motion. The values of H_{II} also vary somewhat with bias field. In comparing these results with changes in bubble chirality, variations in H_I and H_{II} with bias field will be ignored. Hence, the average transition fields for expanding motion are $H_I = 2.47 \pm 0.14$ Oe, and $H_{II} = 3.87 \pm 0.15$ Oe, while for collapsing motion, $H_I = 2.30 \pm 0.06$ Oe, and $H_{II} = 3.53 \pm 0.06$ Oe. Note that the transition fields for expanding motion are generally higher than for collapsing motion. This accounts for the differences between expanding and collapsing motion shown in Fig. (3.2.1).

Changes in Bubble Chirality

Changes in bubble chirality have been observed, using a technique

recently developed by Gallagher, Ju, and Humphrey [22]. In this technique, bubbles are expanded with a small bias pulse in the presence of a small in-plane field. This situation is shown schematically in Fig. (3.2.3) for two bubbles with opposite wall chiralities, designated X^+ and X^-. The direction of $\overline{M}$ in the center of the wall, and in the center of the film, is indicated by arrow heads. They found that the wall section with the center moment antiparallel to the in-plane field moves much more slowly than other wall sections. This behavior can be seen most easily by comparing the static bubble shape, which is indicated by the smaller circles, with the transient shape taken some time after the pulse is applied, which is indicated by the larger circles. For the X^+ bubble, the slow section is on the right, so the bubble expands asymmetrically to the left, while for the X^- bubble, the asymmetry is reversed. Since the pulse amplitude is small, this method does not change the bubble chirality. For this reason, it is preferred over the destructive automotion technique used previously [20,21].

An example of the large differences in dynamic behavior is shown in Fig. (3.2.3). The sampled displacements of the parallel and antiparallel sections, which are shown as A and B in the inset, are plotted here as a function of time in response to a 1.78 Oe bias field pulse. The in-plane field was 4.1 Oe, and the static bias field was 22.9 Oe. For case A, the wall moves rapidly when the pulse is applied at t = 0, with an average velocity of 9.4 m/sec. The wall moves past equilibrium, and returns with an average velocity of 10.4 m/sec. The

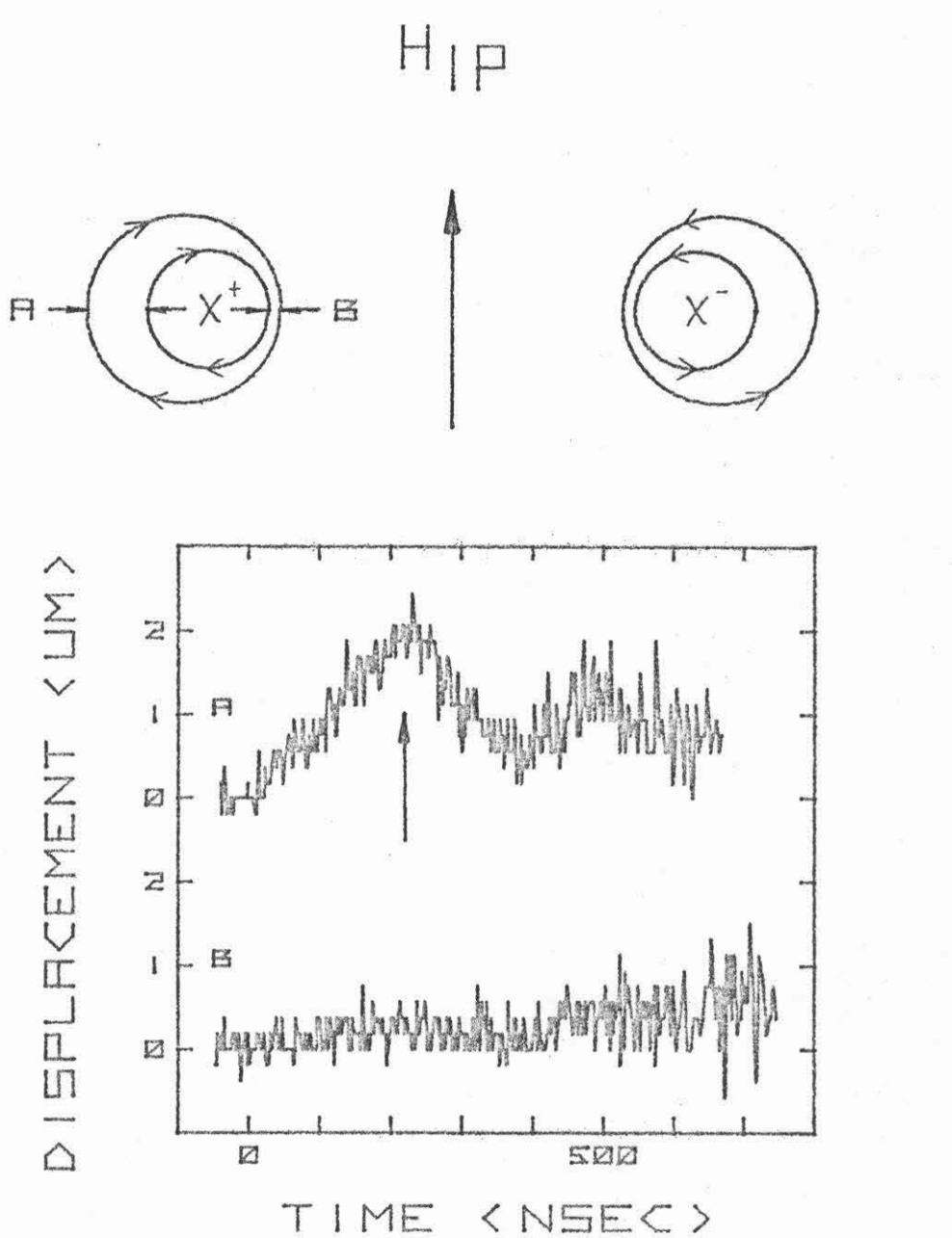

Fig. 3.2.3. Sampled Wall Displacement (μm) + for the Parallel (A) and Antiparallel (B) Wall Sections. In both cases, H_a = 1.78 Oe, H_{ip} = 4.1 Oe, and H_B = 22.9 Oe. The direction of the center spins in the X^+ and X^- chirality, the direction of the in-plane field, and the displacements A and B are shown in the inset.

oscillations shown here are similar to those described in Sec. 3.1, but the average velocities are significantly higher. This is due to the in-plane field, and is investigated further in Sec. 3.3. The behavior of the antiparallel sections, shown in case B, is quite different. When the bias pulse is applied, the wall hardly moves. The reason for this [23] is that the in-plane field nucleates a static HBL structure. Calculations indicate that the effective mass of this structure, which is obtained from Eq. (2.3.15), is more than 100 times larger than m_D. Hence, the antiparallel wall section is effectively pinned. Bubble chirality is determined by placing the laser flash at the first extremum, indicated by the arrow, and then observing the asymmetry in radial expansion shape.

This technique has been used to investigate changes in bubble chirality during collapsing motion. Since transitions to overdamped motion occur both at the beginning and the end of the pulse, changes in chirality may also occur in both places. To eliminate this possibility, the bias field is first lowered quasistatically by an amount H_a over a 10 μsec period, and then abruptly returned to its original value with a 12 nsec rise time. Any changes in chirality may be attributed to a single step change in bias field with amplitude H_a. If the experiment is repeated N times with M changes, the probability of changing chirality is M/N, with an uncertainty of

$$\sigma_p = \left[\frac{M(N-M)}{N^3}\right]^{\frac{1}{2}} \quad . \tag{3.2.1}$$

Though the results reported here are for collapsing motion, similar

results have also been obtained with expanding motion [24].

The probability of changing chirality has been measured as a function of H_a, and the results are shown in Fig. (3.2.4). The error bars, $\pm\sigma_P$, are typically less than 6%. Note the suppressed zero in the H_a scale. For H_a less than 2.0 Oe, P is zero. In the region, 2.0 Oe < H_a < 3.0 Oe, P changes from 0% to nearly 100%. In the region, 3.0 Oe < H_a < 3.5 Oe, the bubble changes chirality almost every time the pulse is applied. Between H_a = 3.5 Oe, and H_a=4.0 Oe, P changes to 0%. This cyclic behavior in P is repeated three times for pulse amplitudes up to 7 Oe. Note that as H_a increases, the changes in P become smaller, and P approaches the random result, P = 50%. The behavior shown here may be characterized by the values of H_a where P crosses 50% for the n^{th} time H_n. The first seven values of H_n are 2.5, 3.8, 4.7, 5.3, 5.7, 6.6 and 6.6 Oe, each with an uncertainty of about 0.2 Oe.

By comparing these results with those shown in Fig. (3.2.2), it can be seen that the transitions to overdamped motion described earlier coincide with changes in bubble chirality. Recall that H_I and H_{II} represent the beginning of the transition region, and that transitions occur in a 0.5 Oe region above these values. For example, the first transition region for collapsing motion takes place between H_a = 2.30 and H_a = 2.80 Oe. It can be seen in Fig. (3.2.4) that this coincides with a region in which P changes abruptly from 0% to 100%. Similarly, the second transition region, between 3.53 and 4.03 Oe, coincides with an abrupt change in P from 100% to 0%. Clearly, since

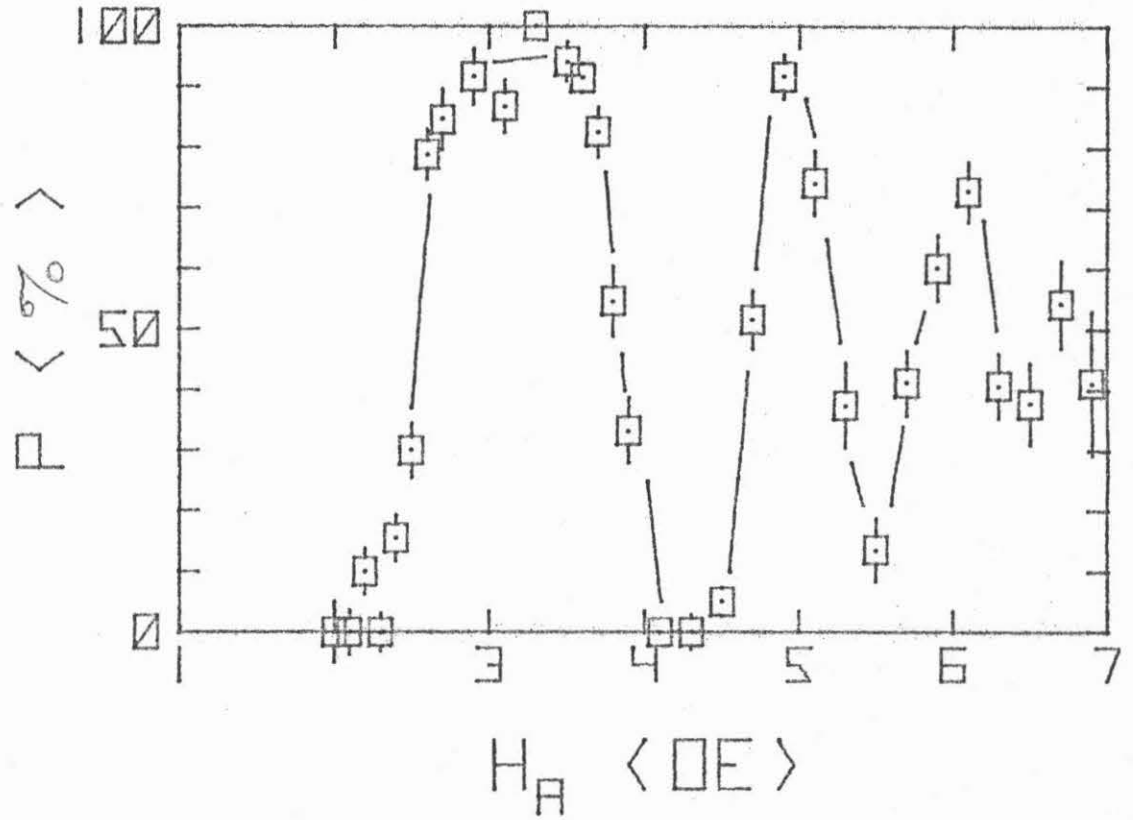

Fig. 3.2.4. The Probability P(%) of Changing Chirality as a Function of Bias Pulse Amplitude, H_a (Oe). The error bars are $\pm\sigma_p$. The line segments are only intended to guide the eye.

behavior at the second overdamped transition is similar to the first, the second abrupt change in P must correspond to a second chirality change during the same step change in bias field. Therefore, the fields H_n correspond to the minimum pulse amplitude required to produce n chirality changes during a single step change in bias field.

Transitions to overdamped motion, which are accompanied by changes in bubble chirality, result from HBL punch-through. Recall from Sec. 2.3 that when the HBL reaches the opposite critical point, it punches-through, leaving the wall with its original, static twist structure. If punch-through occurs just before the wall reaches equilibrium, the wall remains there, and no oscillation is observed. This produces the transitions to overdamped motion described earlier. For larger values of H_z, punch-through occurs earlier, well before the wall reaches equilibrium. This gives the wall the opportunity to nucleate a second HBL during the same bias pulse, so that the oscillations return. If the second HBL punches through before the wall reaches equilibrium, a second transition is observed, and so on. The wall changes chirality each time punch-through occurs, so that, as was shown in Fig. (3.2.4), several changes can occur during a single bias field pulse.

The effects of punch-through on wall motion can be seen in Fig. (3.2.5). The sampled bubble radius is plotted as a function of time in response to a collapsing bias field pulse. In case A, H_a was 2.0 Oe, so that HBL punch-through never occurs, while in Case B,

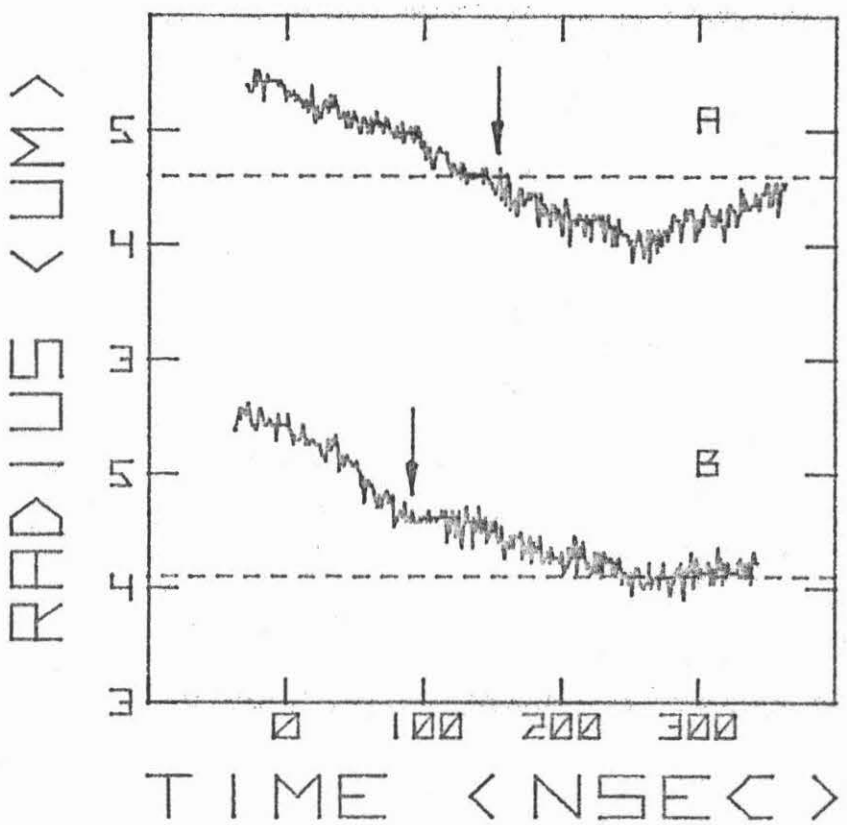

Fig. 3.2.5. Sampled Bubble Radius (μm) as a Function of Time (nsec) in Response to Collapsing Bias Field Pulses. For case A, H_a = 2.0 Oe, and for case B, H_a = 3.0 Oe. Static bias field was 22.0 Oe. The arrows are explained in the text.

3.2.5
3-31

H_a was 3.0 Oe, and punch-through always occurs. In case A, the bubble collapses with a nearly constant velocity of 5.6 m/sec after the pulse is applied at t = 0. The wall moves well beyond equilibrium (at 4.6 μm), and reaches maximum excursion at t = 253 nsec. It then returns to equilibrium with a slightly smaller constant velocity, 4.6 m/sec. The oscillation shown here is similar to those discussed in Sec. 3.1. The motion shown in case B is quite different. The wall moves toward equilibrium, and reaches a maximum velocity of 14 m/sec at about t = 85 nsec. There is a 30 nsec pause in the motion, and then the wall moves toward equilibrium with a 4.0 m/sec average velocity. In this case, no oscillation is observed. Note that the pause occurs well before the wall reaches equilibrium. Similar behavior was found in the numerical solutions of the equations of motion presented in Fig. (2.4.1). There, it was shown that $\langle \dot{q} \rangle$ increases as the HBL approaches the opposite critical point. When punch-through occurs, the calculation shows that the wall stops due to the rapid rotation of ϕ near the film surface. Hence, it seems clear that increased wall velocity and 30 nsec pause shown in case B are due to HBL punch-through. At higher pulse amplitudes, there is some evidence for a second plateau corresponding to a second HBL punch-through, but this feature is at the limit of experimental resolution.

The internal rotation $\langle \phi \rangle$ required to produce HBL punch-through can be calculated from these results. The instantaneous drive field may be calculated from $H_z = H_a u(t) - H'(r_o - r(t))$, where u(t) takes into account the pulse rise time; r_o is the initial equilibrium radius,

and r(t) is the experimental bubble radius as a function of time. This result has been used in Eq. (3.1.2) to estimate $\langle\dot{\phi}(t)\rangle$ from the experimental data shown in Fig. (3.2.5). In case A, the maximum rotation, $\langle\phi\rangle_{max} = 0.71\pi$, is attained when the wall reaches equilibrium at t = 154 nsec. This time is indicated by an arrow. From the HBL model, this amount of rotation is not sufficient to cause punch-through, so that wall oscillation should be seen without changes in wall chirality. This is, in fact, the case, as can be seen in Figs. (3.2.2) and (3.2.4). In case B, $\langle\phi\rangle$ reaches π at t = 92 nsec, just at the beginning of the 30 nsec pause (see arrow). This shows that the beginning of the pause corresponds to the amount of rotation required for punch-through, as expected. Incidentally, these results are inconsistent with the Walker breakdown mechanism associated with one-dimensional structures. As was shown in Sec. 2.1, the wall reverses direction when ϕ reaches $\frac{\pi}{2}$. If this occurs before the wall reaches equilibrium, rotation continues, and the wall changes chirality. However, Fig. (3.2.5a) shows an example in which the maximum rotation is much larger than $\frac{\pi}{2}$, but in which chirality never changes. Note also that the wall motion predicted by the Walker model is inconsistent with the motion shown in this figure.

Cases where more than one punch-through occurs may be analyzed by, again, assuming that the wall velocity is constant, $\langle\dot{q}\rangle = v_s$. Assume that punch-through occurs each time $\langle\phi\rangle$ reaches an integer multiple of π. Then, from Eq. (3.1.3), the pulse amplitude required just to produce a maximum rotation of $n\pi$ is

$$H_n = \sqrt{\frac{2v_s H'}{\gamma}} \cdot \sqrt{n\pi} + H_{sv} \quad , \qquad (3.2.2)$$

Note that since H_z decreases as the wall approaches equilibrium, this simple model predicts that H_n is proportional to $\sqrt{n\pi}$.

The experimental values of H_n from Fig. (3.2.4) have been plotted in Fig. (3.2.6) as a function of $\sqrt{n\pi}$. The uncertainty in H_n is about the size of the symbols. The straight line is a least squares fit to the data. It can be seen that the points all lie on a straight line, within experimental error, which indicates that H_n is proportional to $\sqrt{n\pi}$, as expected. The fitted slope, 1.38 Oe, is in good agreement with the value calculated from Eq. (3.2.2), $\sqrt{\frac{2v_s H'}{\gamma}} = 1.38$ Oe. The value of v_s used here was extrapolated from Fig. (3.1.3) for $H_a = 2.30$ Oe, $v_s = 7.9$ m/sec. The fitted intercept, +0.28 Oe, is much larger than the expected value, $H_{sv} = 0.03$ Oe. However, since H_{sv} is much less than the uncertainty in H_n, agreement is not expected. These results indicate that punch-through occurs each time $\langle\phi\rangle$ reaches an integer multiple of π and are clearly inconsistent with the HBL stacking mechanism.

Section 3.3. Wall Oscillation in the Presence of In-Plane Fields

Past studies of wall oscillation indicate that the dynamic wall structure is influenced by the presence of external in-plane fields. There is some indication that with large in-plane fields present, the dynamic wall structure is essentially one-dimensional. With this structure, wall motion is described by the harmonic oscillator model.

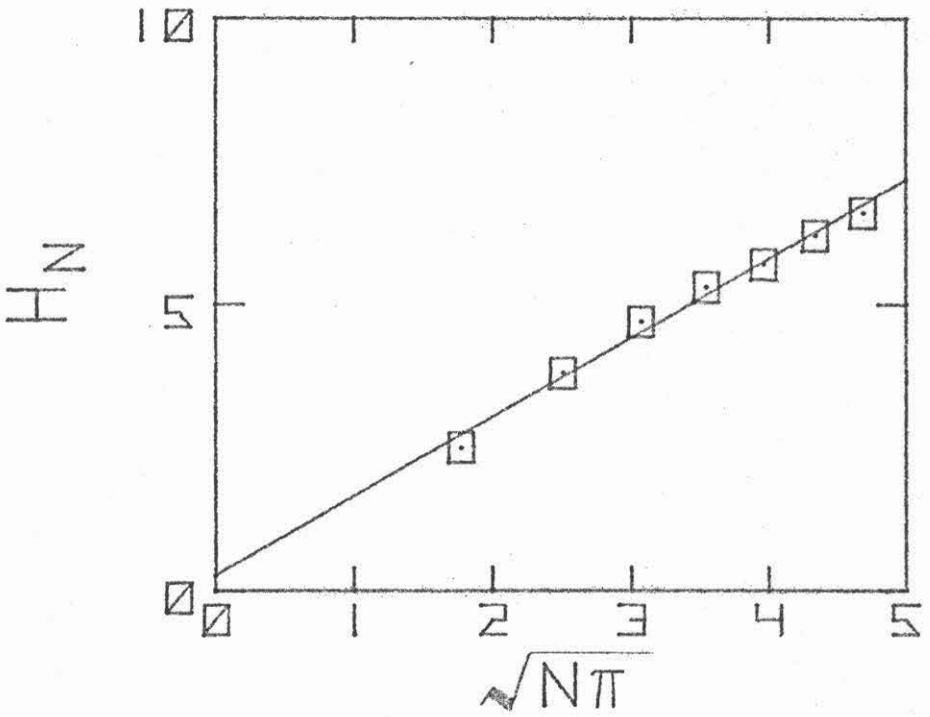

Fig. 3.2.6 Experimental Values of H_θ (Oe) from Fig. (3.2.4) as a Function of $\sqrt{n\pi}$. Uncertainty, 0.2 Oe, is about the size of the symbols. The straight line is a least-squares fit to the data.

In this model, the oscillation frequency ν, which is given in Eq. (2.2.19), is strongly influenced by in-plane fields. The first measurements of ν as a function of H_x gave ambiguous results, which did not agree with the model. In one case [12], ν was independent of H_x, while in another [11], ν was proportional to H_x. More recent measurements [10] made with large in-plane fields perpendicular to the wall indicate that ν^2 is proportional to H_y, in agreement with the model. However, in all cases, strong deviations from simple harmonic motion were observed at reduced in-plane fields. Low-frequency oscillations were observed in low-loss materials [9-11], while in higher-loss materials the oscillations disappear completely [12,13]. The purpose here is to show that large in-plane fields do, in fact, produce one-dimensional dynamic wall structures during wall oscillation. Having established this structure, it is then shown that the onset of nonlinear behavior at reduced in-plane fields is due to HBL nucleation. Finally, by observing initial rapid motion in this region of in-plane fields, it is shown that prior to HBL nucleation, the wall has a simple dynamic twist structure.

Parallel stripe domains are used here instead of bubbles because of the in-plane field. Past studies [25] indicate that dynamic behavior can depend on both the magnitude and direction of the in-plane field. In this situation, the behavior of bubble domains would represent a complicated mixture of all possible orientations. This makes bubbles less suitable for in-plane field studies. Instead, parallel stripe domains are used here since the walls make a constant

angle with respect to the in-plane field. In this domain configuration, direction and magnitude effects can be studied independently. As can be seen in Fig. (2.3.1), the surface demagnetizing fields in bubble and zero-bias stripe domains are similar, so that the twist structures produced by these two configurations are not significantly different. However, the effective field gradient in zero-bias stripes, 6.4 Oe/μm, is nearly three times higher than in bubble domains. This produces much higher oscillating frequencies.

Wall Oscillation with Large In-plane Fields

Wall oscillation has been observed with large in-plane fields parallel to the domain wall (H_x), and the results are shown in Fig. (3.3.1). Half of the sampled stripe width, which corresponds to wall position, is shown here as a function of time with H_x as a parameter. The pulse amplitude was the same in each case, H_a = 4.33 Oe, and the static bias field was zero. Note that the time scales are different in each case in order to show the oscillations more clearly. The smooth curves are fits to the harmonic oscillator model, and will be discussed later. The oscillations in case A, for H_x = 41 Oe, are sinusoidal rather than triangular, and four complete oscillations can be seen. The frequency, ν = 18.1 ± 1.4 MHz, is approximately constant from one cycle to the next. In fact, more detailed measurements indicate that ν is independent of H_a over the range, 2.0 Oe < H_a < 6.5 Oe [25]. Sinusoidal oscillations can also be seen in case B, where H_x is 80 Oe. Again, four complete oscillations can be seen, but the frequency, ν = 25.1 ± 2.6 MHz, is 40% higher than in case A. When

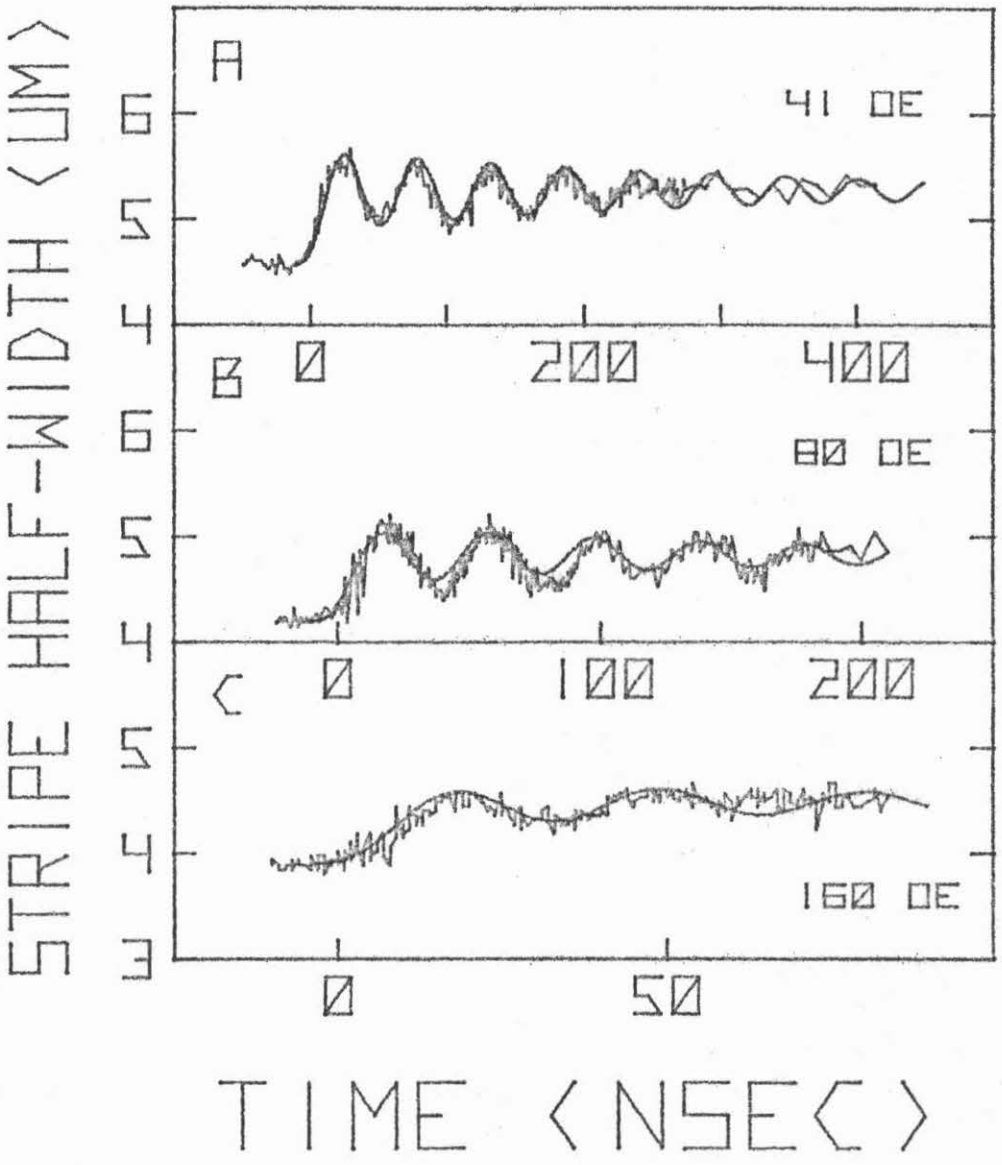

Fig. 3.3.1. Sampled Stripe Half-Width (μm) as a Function of Time (nsec) with In-plane Field, H_x (Oe), as a Parameter. The magnitudes (angles between in-plane field and wall) for cases A, B, and C are 41 Oe (0°), 80 Oe (20°), and 160 Oe (15°), respectively. In each case the pulse amplitude was 4.33 Oe, and the static bias field was zero. The smooth curves are solutions of the harmonic oscillator model and are discussed in the text.

H_x is raised to 160 Oe in case C, the frequency increases to 36 MHz. Note that only one oscillation can be seen in this case even though the pulse amplitude is the same. It will be shown that this is due to the nonzero rise time of the bias pulse. Over the range of H_x shown here, the in-plane field produces sinusoidal oscillations in which the frequency increases with increasing in-plane field.

The wall twist structure is strongly affected by large external in-plane fields. For example, with the in-plane field parallel to the wall (H_x), the twist is reduced as each center spin reorients toward the +x-axis. For large in-plane fields, the surface demagnetizing fields become insignificant, and the static twist function assumes the one-dimensional form, $\phi(z) = 0$. The dynamic effects of the in-plane field have been estimated by calculating the effective wall mass given in Eq. (2.3.15) as a function of H_x, and the results are shown in Fig. (3.3.2). For comparison, the dotted curve shows the wall mass for one-dimensional structures, $m/m_D = (1 + H_x/8M_s)^{-1}$, from Eq. (2.2.16). When H_x is zero, the twisted wall mass is 75% larger than m_D. As H_x increases, the twisted wall mass decreases, and asymptotically approaches the curve for one-dimensional wall structures. In fact, for H_x = 41 Oe, (see arrow) the smallest field used in Fig. (3.3.1), the twisted wall mass is only 6% larger than the one-dimensional value. For other orientations, the twist is reduced as the spins reorient toward the direction of the in-plane field, and the effective mass, again, approaches the one-dimensional value.

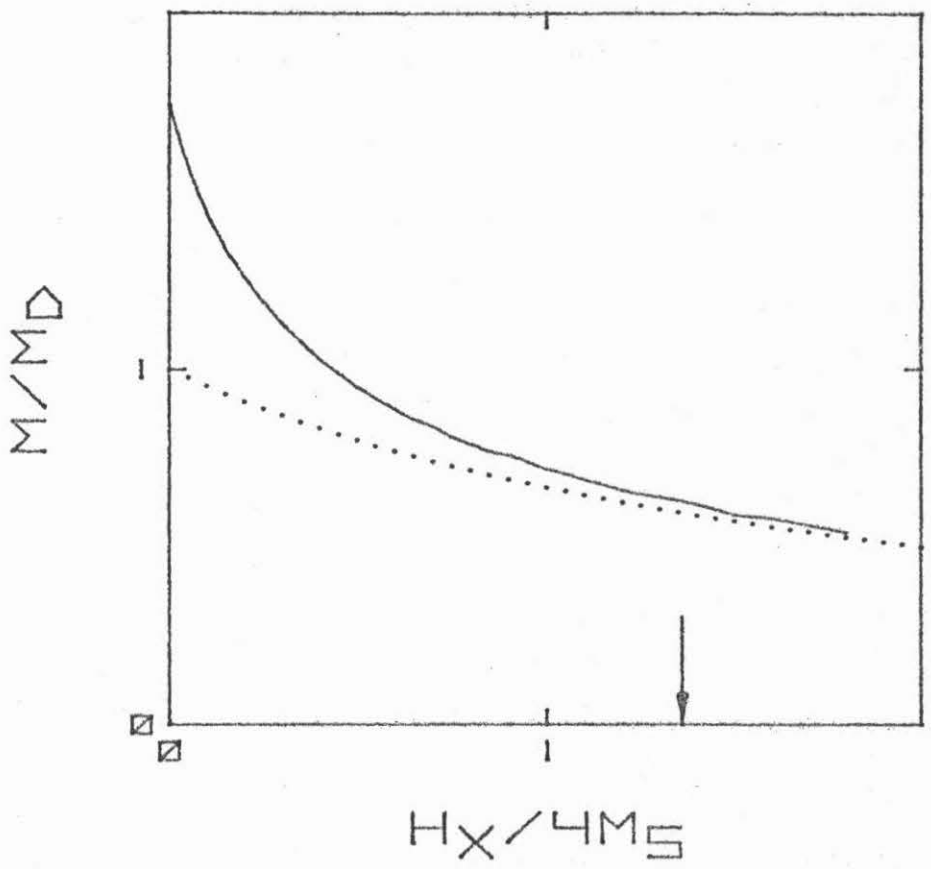

Fig. 3.3.2. Calculated Effective Wall Mass (m/m_D) as a Function of In-plane Field Parallel to the Wall ($H_x/4M_s$) for Twisted (solid) and One-dimensional (dotted) Wall Structures. The arrow indicates the field 41 Oe/$4M_s$ = 1.36.

The results shown in Fig. (3.3.1) have been fitted to the harmonic oscillator model, and the results are shown as smooth curves. Analytic solutions of Eq. (2.2.18) have been fitted by using f_0', which is related to the wall mass [see Eq. (2.2.16)], as an adjustable parameter. Theoretical values of f_0' were calculated from Eqs. (2.2.6a) and (2.2.9d). The fitted (calculated) values of f_0' for cases A, B, and C are 115 Oe (156 Oe), 206 Oe (210 Oe), and 342 Oe (337 Oe), respectively. In all three cases, the shape of the oscillations is in good agreement with the shapes calculated from the model. In cases B and C, the fitted values of f_0' are in good agreement with the theoretical values, which indicate that the wall mass is correctly given by Eq. (2.2.16). In case A, the fitted mass is 35% larger than the theoretical value. This difference is due to the close proximity of HBL-dominated motion at slightly lower in-plane fields. Note that the reduced amplitudes shown in case C is also found in the calculated motion. The reason for this reduction is that as H_x increases, the mass decreases, and the initial wall response becomes faster. In the limit of large H_x, the 12-nsec-rise-time bias field pulse represents a quasistatic change in bias field, and no oscillation is observed. Case C represents an intermediate case in which some oscillation can still be seen, but with a somewhat reduced amplitude. Note also that the damping shown in Fig. (3.3.1) is consistent with the resonance value of α, 0.003, used in the calculation. A comparison of the motion shown in Fig. (3.3.1) with the harmonic oscillator model shows that the dynamic wall structure is essentially

one-dimensional for in-plane fields H_x larger than 41 Oe.

The oscillation frequency has been measured as a function of both the magnitude and direction of the in-plane field, and the results are shown in Fig. (3.3.3). It can be seen from Eq. (2.2.19) that ν depends on a single independent variable, f_o', which may be calculated from experimental values of $\overline{H}_{ip}$ and $4M_s$. Hence, the combined dependence of ν on both the magnitude and direction of $\overline{H}_{ip}$ is shown here in a single plot of ν as a function of $\sqrt{f_o'}$. The minimum in-plane field magnitude used was 30 Oe, due to the HBL-dominated motion at lower values, while the highest magnitude was limited to 180 Oe by reductions in oscillation amplitude. The largest acute angle between the wall and the in-plane field was 80°, because at higher angles, the parallel stripe array tends to buckle severely. The typical uncertainty in ν, which is indicated by a few error bars, is 15%. The relationship predicted by the harmonic oscillator model, Eq. (2.2.19), is indicated by a straight line. It can be seen that about 80% of the points lie along this line, within experimental error. This indicates that ν is correctly given by the harmonic oscillator model over a wide range of in-plane field conditions. This result has also been verified for specific examples [24]. The inset shows a histogram of the ratios of the experimental wall mass, $m_E = H'f_o'/(2\pi)^3\nu^2$, to m_D. The strong peak at $m_E/m_D = 1$ indicates that the wall mass is correctly given by the harmonic oscillator model for most of the data. The remaining points, which correspond to points well below

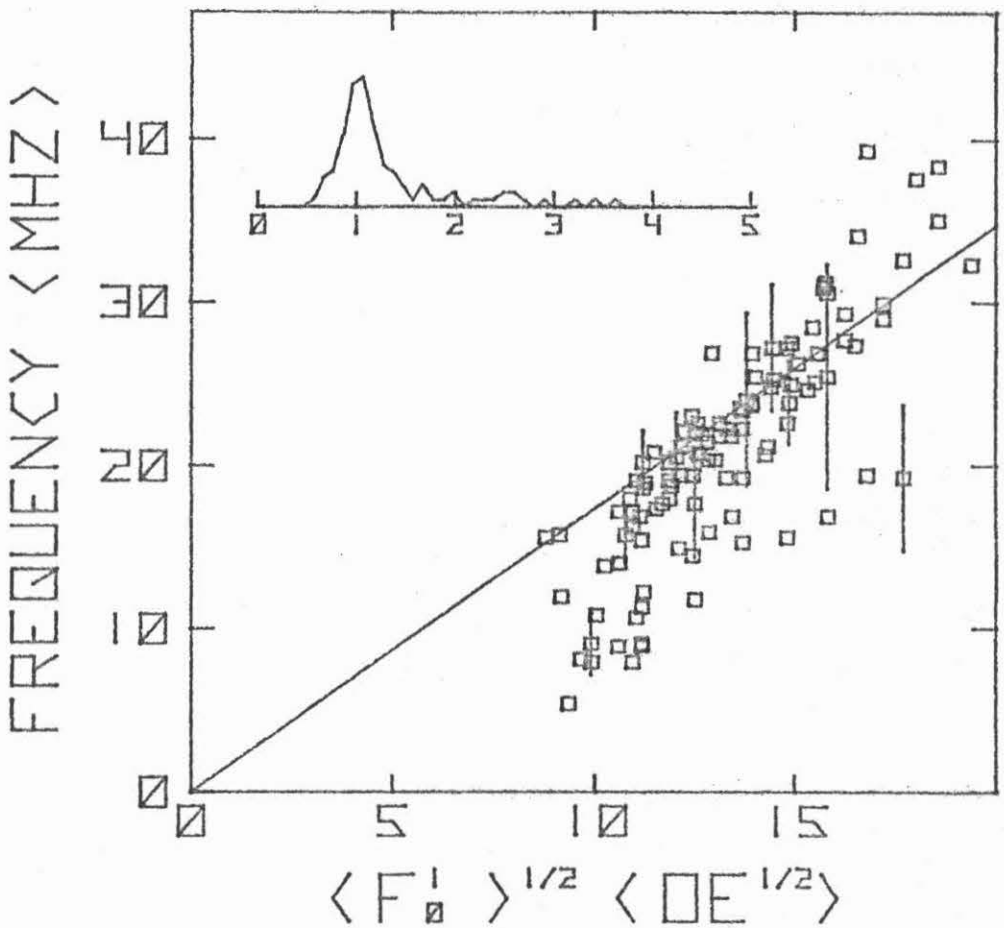

Fig. 3.3.3. Oscillation Frequency ν (MHz) as a Function of the Derived Independent Variable, $\sqrt{f_0'}\ \sqrt{(\ 0e)}$. The significance of f_0' is explained in the text. The straight line is the theoretical relationship based on the harmonic oscillator model. The inset is a histogram of the experimental mass divided by its theoretical value.

the line in the main figure, represent higher masses. The reason for these anomalously heavy walls is unknown at the present time. These results show that, regardless of the in-plane field direction, the dynamic wall structure is essentially one-dimensional for sufficiently large in-plane field magnitudes.

HBL Nucleation and Initial Rapid Motion at Reduced In-plane Fields

A gradual transition to HBL-dominated wall motion with decreasing in-plane field is shown in Fig. (3.3.4). Wall displacement in zero-bias stripes is shown here as a function of time with H_x as a parameter. In each case, H_a was 3.00 Oe. Greater spatial resolution is obtained by using the photometric technique described earlier. The new equilibrium wall positions are indicated by arrows. The curves are analytic solutions of Eq. (2.2.18), and are discussed later. The initial rapid motion described earlier can be seen quite clearly in all three cases. When the pulse is applied at t=0 in case A (H_x=0), the stripe domains expand rapidly for about 22 nsec, and reach a maximum velocity of about 18 m/sec. The total displacement during this time is 0.29 μm. After this initial rapid motion, there is a short pause, and then the wall moves with a much lower average velocity, 6.4 m/sec. After reaching its maximum displacement at t=114 nsec, the wall moves back toward equilibrium. The behavior shown here is similar to that found earlier in bubble domains [see Fig. (3.1.1)]. The behavior shown in case B (H_x = 4 Oe) is somewhat different. Again, initial rapid

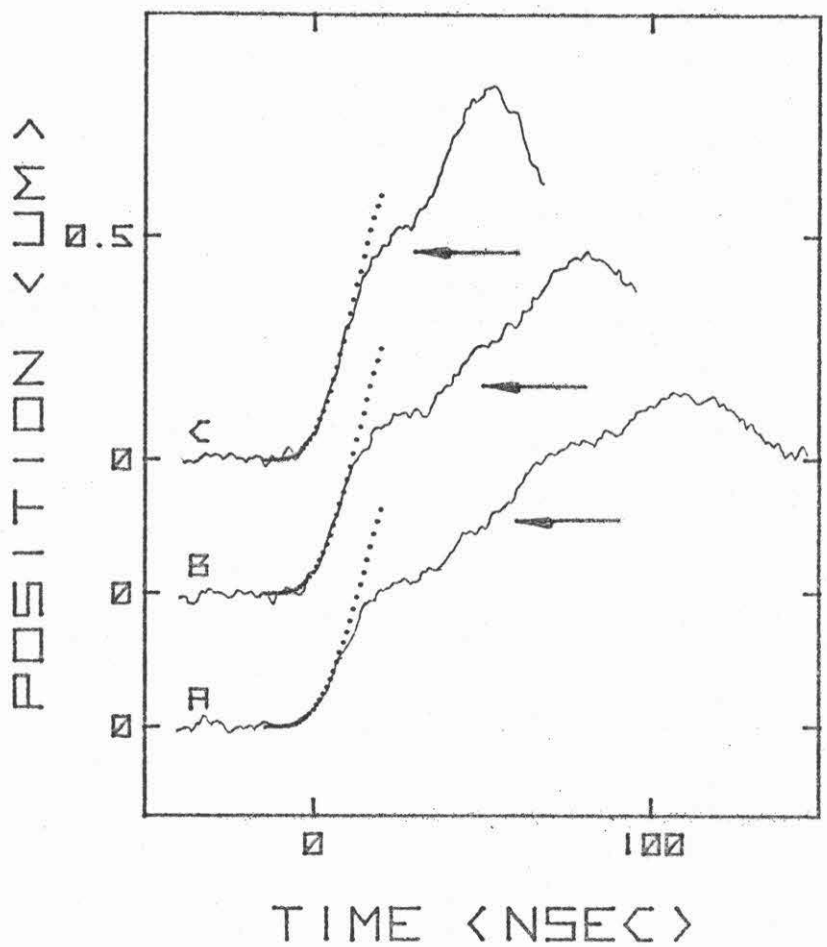

Fig. 3.3.4. Wall Displacement (μm) in Zero-bias Stripes, Obtained by Using the Photometric Technique, as a Function of Time (nsec) with In-plane Field H_x as a Parameter. The values of H_x for cases A, B, and C are 0 Oe, 4 Oe, and 10 Oe, respectively. In each case, the pulse amplitude was 3.00 Oe. The dotted curves are solutions of the harmonic oscillator model and are discussed in the text. The new equilibrium wall positions are indicated by arrows.

motion is seen for the first 22 nsec, but the maximum velocity, 23 m/sec, and total displacement, 0.39 μm, are both significantly greater than in case A. After a short pause, the wall moves with a lower velocity, 8.2 m/sec, and reaches maximum displacement after 87 nsec. In case C (H_x = 10 Oe), the wall reaches a maximum velocity of 26 m/sec during initial rapid motion. After a displacement of 0.44 μm, initial rapid motion ends just before the wall reaches equilibrium, at 0.48 μm. After a short slow section, the wall moves past equilibrium with a relatively high velocity, 19 m/sec, and reaches maximum displacement after 54 nsec. For higher values of H_x, the slow section disappears, and the motion is sinusoidal, as described earlier.

The extent of the low velocity sections shown in Fig. (3.3.4) depends on where the wall is when the HBL is formed. Case A (lowest curve) represents a situation in which the HBL is formed well before the wall reaches equilibrium. When nucleation occurs, H_z is still relatively large, so that the HBL moves well into the film center, producing a long slow section with a relatively low average velocity. In case B, the HBL is formed somewhat closer to equilibrium, so that H_z is smaller. The HBL only moves part way into the film, so that the slow wall velocity is higher than in case A, and the slow section is shorter. Case C represents a situation in which the HBL forms just as the wall reaches equilibrium. The HBL remains near the film surface and produces only a slight drop in wall velocity. When the wall passes equilibrium, H_z reverses sign, and the HBL disappears, leaving the wall with a simple twist structure. Because of the small mass

associated with this structure, the subsequent motion resembles initial rapid motion. For larger in-plane fields, the wall reaches equilibrium before the HBL is formed, resulting in sinusoidal motion.

Changes in initial rapid motion with in-plane field shown in Fig. (3.3.4) are due to reduced effective wall masses. The dotted curves shown here are analytic solutions of the harmonic oscillator equation, Eq. (2.2.18). The effective masses used in these calculations were taken from the results shown in Fig. (3.3.2) for simple twisted walls in the presence of an in-plane field H_x. The values for cases A, B, and C are 1.75 m_D, 1.38 m_D, and 1.12 m_D, respectively. It can be seen that in each case, the calculated motion is in good agreement with the experimental results up to the point where the HBL is formed. Of course, beyond this point, the twist structure is no longer of the simple type, and agreement is not expected. As can be seen, the time at which the HBL forms is about the same in each case, 22 nsec, so that as the effective mass decreases with increasing H_x, the displacement during initial rapid motion increases, and the HBL nucleates closer to equilibrium. Hence, the transition to sinusoidal motion with increasing H_x shown here is due to a reduction in effective wall mass, and the corresponding increase in displacement during initial rapid motion.

The equations of motion, Eqs. (2.3.12a-c), have been solved numerically for the specific examples shown in Fig. (3.3.4), and the results are shown in Fig. (3.3.5). The motion shown in case A closely resembles the data. The calculation shows that the twist structure during initial rapid motion is similar to the original, static twist

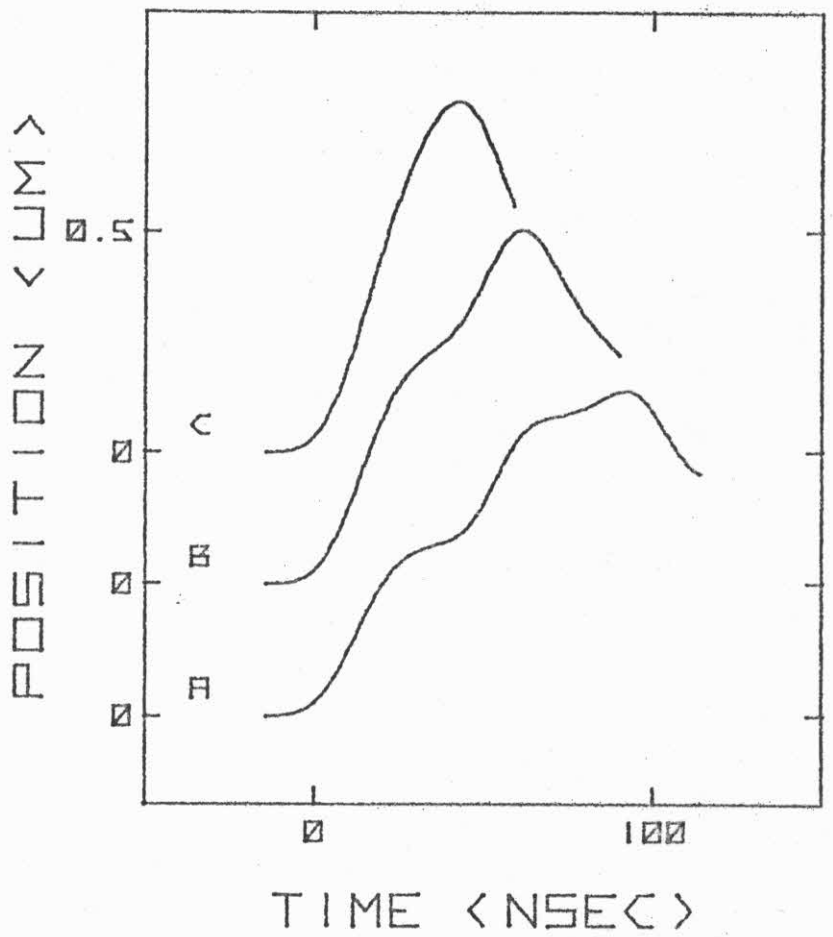

Fig. 3.3.5. Calculated Wall Displacement, (μm), as a Function of Time (nsec) with In-plane Field H_x as a Parameter. The pulse amplitude and in-plane fields used in the calculation are the same as those used in Fig. (3.3.4).

structure, as expected, and that the onset of slower wall velocities does, in fact, correspond to the formation of an HBL. The irregular motion, which in the calculation is due to internal vibrations is also found in the experimental data. This indicates that the wall may actually deviate from a flat surface as it moves. The calculated velocities shown here are about 20% higher than the experimental values. Recall that a similar discrepancy was also found in the numerical simulation of wall motion in bubble domains [see Figs. (3.1.1) and (3.1.4)]. This may be due to slight differences between the form of $H_s(z)$ used in the calculation, and the actual surface demagnetizing fields. Because of the long calculation times involved, no attempt has been made to adjust H_s in order to fit the data more closely. In case B, the HBL forms when the wall is closer to equilibrium, and the HBL stays closer to the film surface. Since velocities are somewhat higher in the calculation, the motion corresponds more closely to an experimental situation with a somewhat higher in-plane field, $H_x \simeq 8$ Oe. In case C, the initial rapid motion is so fast that the HBL never forms, and the resulting motion is nearly sinusoidal. Again, the calculated result corresponds to an experimental situation with a slightly higher in-plane field, $H_x \simeq 14$ Oe.

Section 3.4. Conclusions

The presence of horizontal Bloch lines during domain wall motion has been established by comparing results from wall oscillation

experiments with the model of domain wall motion presented in Ch. 2. During the initial response to a bias field pulse, the dynamic wall structure is similar to the original static structure. Since the effective mass is relatively small, the wall accelerates quickly, resulting in the initial rapid motion shown in Figs. (3.1.1) and (3.3.4). An HBL gradually forms near one of the film surfaces as a result of local dynamic properties. As the HBL moves toward the opposite surface, it significantly decreases the wall velocity, and, in wall oscillation experiments, produces the low frequency, triangular-shaped oscillations shown in Fig. (3.1.1). If the HBL reaches the opposite film surface, it becomes unstable, and disappears in a process called punch-through. During punch-through, the energy and momentum stored in the HBL are dissipated, and the wall changes chirality. If punch-through occurs just before the wall reaches its new equilibrium position, an abrupt transition to overdamped motion is observed [see Fig. (3.2.1)]. Chirality changes, which occur each time the average azimuthal angle reaches an integer multiple of π, have also been observed [see Fig. (3.2.5)]. These results show for the first time that changes in wall chirality coincide with a loss of stored momentum. An external in-plane field reduces the effective wall mass of the initial static twist structure so that the wall travels further before the HBL is formed. If the wall reaches equilibrium before an HBL is formed, sinusoidal oscillations, which are associated with structure-free domain walls, are observed [see Fig. (3.3.1)]. At reduced in-plane fields, the onset of reduced wall

velocities shown in Fig. (3.3.4) is associated with HBL formation. These results clearly establish the existence of horizontal Bloch lines as specific internal wall structures.

REFERENCES

1. G. J. Zimmer, L. Gal, K. Vural, and F. B. Humphrey, J. Appl. Phys. 46, 4976 (1975).
2. J. A. Seitchik, W. D. Doyle, and G. K. Goldberg, J. Appl. Phys. 42, 1272 (1971).
3. P. W. Shumate, Jr., J. Appl. Phys. 42, 5770 (1971).
4. G. P. Vella-Coleiro, Appl. Phys. Lett. 29, 445 (1976).
5. A. H. Bobeck, IEEE Trans. MAG-6, 445 (1970).
6. F. C. Rossol, J. Appl. Phys. 40, 1082 (1969).
7. G. P. Vella-Coleiro, and W. J. Tabor, Appl. Phys. Lett. 21, 7 (1972).
8. B. E. MacNeal and F. B. Humphrey, J. Appl. Phys. 48, 3869 (1977).
9. B. R. Brown, G. R. Henry, R. W. Koepcke, and C. E. Wieman, IEEE Trans. MAG-11, 1391 (1975).
10. F. H. de Leeuw and J.M. Robertson, J. Appl. Phys. 46, 3182 (1975).
11. R. W. Shaw, J. W. Moody, and R. M. Sandfort, J. Appl. Phys. 45, 2672 (1974).
12. B. E. Argyle, and A. P. Malozemoff, AIP Conf. Proc. 10, 344 (1972).
13. J. W. Moody, Roger W. Shaw, Robert M. Sandfort, and R. L. Stermer, IEEE Trans. MAG-9, 377 (1973).
14. F. H. de Leeuw, R. van den Doel, and J. M. Robertson, J. Appl. Phys. 49, 768 (1978).
15. G. J. Zimmer, L. Gal, and F. B. Humphrey, AIP Conf. Proc. 29, 85 (1975).

16. G. R. Woolhouse, and P. Chaudhari, AIP Conf. Proc. 18, 247 (1973).

17. B. E. Argyle, and A. Halperin, IEEE Trans. MAG-9, 238 (1973).

18. F. H. de Leeuw, J. Appl. Phys. 45, 3106 (1974).

19. A. P. Malozemoff, J. Magn. and Magnetic Mat. 3, 234 (1976).

20. P. Dekker, and J. C. Slonczewski, Appl. Phys. Lett. 29, 753 (1976).

21. B. E. Argyle, S. Maekawa, P. Dekker, and J. C. Slonczewski, AIP Conf. Proc. 34, 131 (1976).

22. T. J. Gallagher, K. Ju, and F. B. Humphrey, to be published in J. Appl. Phys.

23. T. J. Gallagher, and F. B. Humphrey (unpublished).

24. B. E. MacNeal, and F. B. Humphrey, to be published in J. Appl. Phys.

25. Floyd B. Humphrey, IEEE Trans. MAG-11, 1679 (1975).

Appendix A. Static Properties of Stripe and Bubble Domains

Statically stable domain configurations are determined by minimizing the total energy with respect to the domain dimensions. First, the total domain energy E_T is calculated as a function of adjustable parameters, which describes the domain geometry. Equilibrium conditions are obtained by setting the first derivatives of E_T, which represent generalized forces, equal to zero. Finally, it is necessary to demonstrate stability, since, as will be shown later, not all force-free geometries represent stable configurations. Contributions to E_T come from three sources: domain walls, external magnetic fields, and demagnetizing sources. It is assumed here that the wall energy (per unit area) σ_w is constant, i.e., independent of the domain geometry. Though internal wall structures are important in wall dynamics, it was shown in Ch. 2 that such structures do not significantly alter σ_w in high-Q materials. The wall energy E_w produces a constant surface tension, which always tends to minimize wall area. The external bias field energy E_B, which is just the integral of $-\bar{M} \cdot \bar{H}_B$ over the sample volume, always tends to expand those domains with $\bar{M}$ parallel to $\bar{H}_B$ at the expense of the antiparallel domains. The effects of in-plane fields are not considered here. Energy contributions from interactions between the sources $\nabla \cdot \bar{M}$ at the film surfaces are calculated by using Eq. (2.i.6d). This demagnetizing energy E_d tends to return the sample to its demagnetized state, with up and down domains occupying equal surface area. It is assumed here that $\bar{M}$

in the domain interiors is always parallel to the easy axis and that energy contributions from exchange and anisotropy occur only in the vicinity of the domain walls. The purpose of this appendix is to present a brief summary of the static properties of stripe and bubble domains as a function of the bias field, and to present examples calculated for the sample studied in Ch. 3.

Parallel Stripe Array

A schematic diagram of the simplified model of stripe domains used here [1] is shown in Fig. (1.2a). The origin of a coordinate system (x,y,z) is located in the center of a domain that has $\overline{M}$ parallel to $\overline{H}_B$, with the stripes all parallel to the x-axis. For the sake of consistency, $\overline{H}_B$ points along the +z-axis. The widths of domains with $\overline{M}$ parallel and antiparallel to $\overline{H}_B$ are indicated by d_1 and d_2 respectively. It is assumed that the walls are always parallel to the z-axis and that any wall bulging, which may occur when $\overline{H}_B$ is not zero, may be neglected. It will be convenient to specify the domain configuration by two dimensionless parameters s and q, which are defined by

$$q = \frac{h}{d_1+d_2} \quad , \tag{A.1a}$$

and

$$s = d_1-d_2/d_1+d_2 \quad . \tag{A.1b}$$

This model presents a simplified picture of the actual domain configura-

tion, but the results of this analysis are in good agreement with the experimental properties of stripe domains.

The total stripe energy (per unit area of the material) E_T may be calculated as a function of s and q. The wall energy is just σ_w times the total wall area contained per unit area of the material. The wall area per unit stripe length in a pair of stripes is 2h, so that E_w is just

$$E_w = 2\sigma_w q \quad . \tag{A.2}$$

The bias field energy per unit stripe length of a domain with $\overline{M}$ along $\overline{H}_B$ is $-M_s H_B d_1 h$, and the energy for a domain with the opposite orientation is $+M_s H_B d_2 h$, so that the bias field energy is

$$E_B = -M_s H_B h s \quad . \tag{A.3}$$

The demagnetizing energy is obtained from Eq. (2.i.6d) as

$$E_d = \frac{1}{2} \iint_{\substack{\text{unit} \\ \text{area}}} dxdy \; V(\overline{r}) \; \rho(\overline{r}) \quad , \tag{A.4}$$

where the magnetostatic charge density $\rho(\overline{r})$ originates from $\nabla \cdot \overline{M}$ at the film surfaces and the potential V is obtained by solving Poisson's equation with standard techniques. The integral in Eq. (A.4) is evaluated, and the result is [1]

$$E_d = 2\pi M_s^2 h s^2 +$$

$$\frac{8}{\pi^2} M_s^2 \frac{h}{q} \left\{ \sum_{n=1}^{\infty} \frac{\sin^2(\frac{n\pi}{2}(1+s))}{n^3} (1-e^{-2n\pi q}) \right\} \quad . \qquad (A.5)$$

By combining the results of Eq. (A.3-5), the total energy per unit area of the material may be expressed in terms of s and q.

The equilibrium conditions for the stripe array are obtained by setting the first derivatives of E_T equal to zero. The first condition, which is obtained by equating $\frac{\partial E_T}{\partial s}/4\pi M_s^2 h$ to zero is

$$-\beta + s + \frac{1}{\pi^2 q} \sum_{n=1}^{\infty} \frac{\sin(n\pi(1+s))}{n^2}(1-e^{-2n\pi q}) = 0 \quad , \qquad (A.6)$$

where $\beta = H_B/4\pi M_s$. The first term represents a force due to the external bias field and the second and third terms represent surface tension and demagnetizing forces respectively. By using a similar procedure with $\partial E_T/\partial q$, the second equilibrium condition may be written as

$$\lambda - \frac{1}{\pi^3 q^2} \left(\sum_{n=1}^{\infty} \frac{\sin^2(\frac{n\pi}{2}(1+s))}{n^3} \cdot \right.$$

$$\left. \left[1 - e^{-2n\pi q}(1+2n\pi q)\right] \right) = 0 \quad , \qquad (A.7)$$

where $\lambda = \ell/h$, and $\ell = \frac{\sigma_w}{4\pi M_s^2}$. The first term represents surface tension, while the second term represents the demagnetizing force. The equilibrium values of d_1 and d_2 are determined by solving Eqs. (A.6-7)

simultaneously for the equilibrium values of s and q.

The stability conditions for a stripe array are obtained by expanding E_T around equilibrium and by making the quadratic terms positive definite functions of Δs and Δq. The domain configuration is stable if E_T satisfies

$$\frac{\partial^2 E_T}{\partial s^2} > 0 \quad , \tag{A.8a}$$

and

$$\left(\frac{\partial^2 E_T}{\partial s^2}\right)\left(\frac{\partial^2 E_T}{\partial q^2}\right) - \frac{\partial^2 E_T}{\partial s \partial q} > 0 \quad . \tag{A.8b}$$

Numerical calculations indicate [1] that these conditions are satisfied for all meaningful values of s and q.

The equilibrium conditions have been solved numerically by using material parameters from the sample investigated in Ch. 3 (see Table (3.I)), and the results are shown in Fig. (A.1). The equilibrium values of s and q were used to calculate the equilibrium values of d_1/h, d_2/h, and $\frac{d_1+d_2}{h}$ as functions of $H_B/4\pi M_s$. It can be seen that when H_B is zero, the net magnetization is zero, since $d_1=d_2$. By setting s to zero in Eq. (A.7), λ is given in terms of q by

$$\lambda = \frac{1}{n^3 q^2} \sum_{n=1}^{\infty} \frac{1 - e^{-2n\pi q}(1+2n\pi q)}{n^3} \quad . \tag{A.9}$$

This relationship is often used to determine λ experimentally from

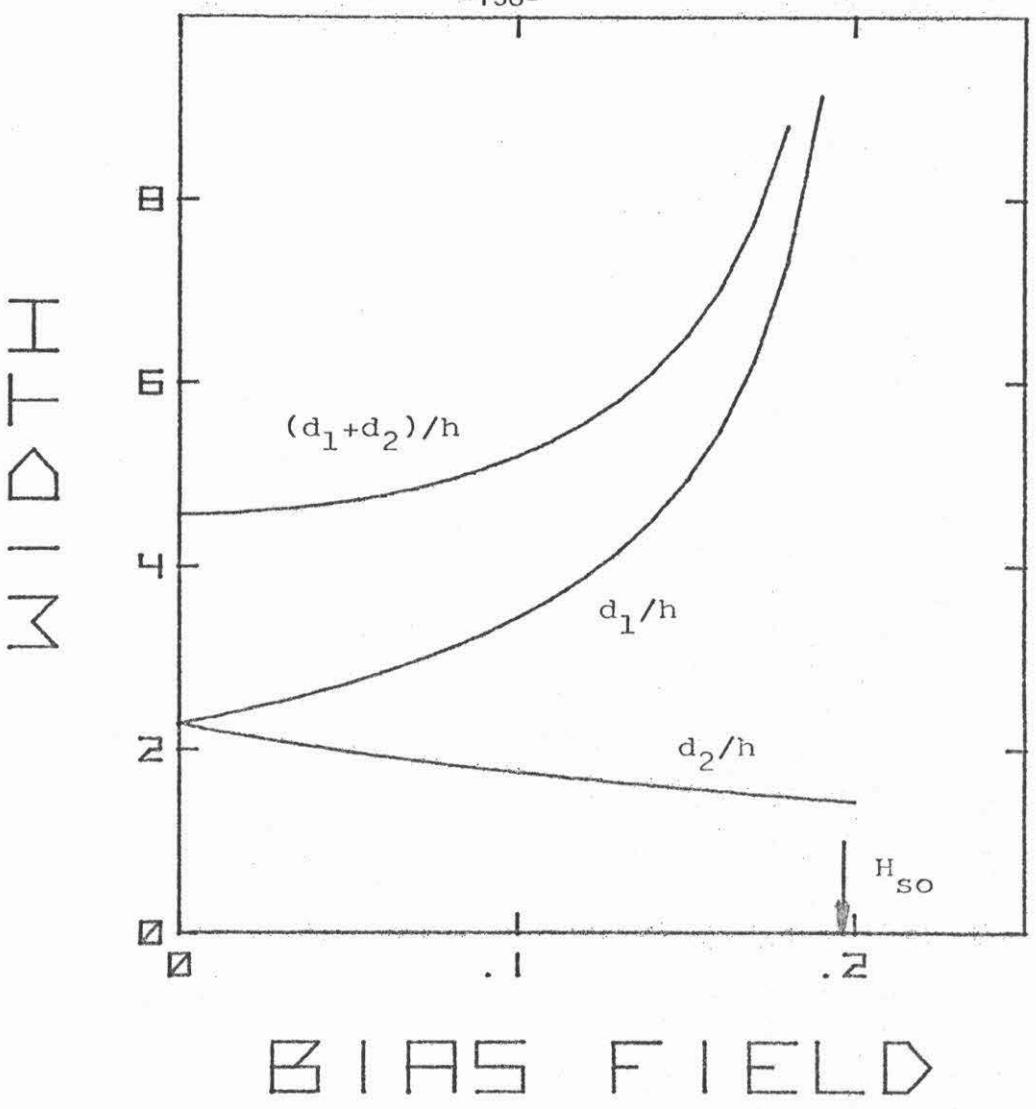

Fig. (A.1): Equilibrium Stripe Width and Period, d_1/h, d_2/h, and d_1+d_2/h, as Functions of Bias Field, $H_B/4\pi M_s$, Calculated for the Case $\lambda = 0.3$. The bubble stripe-out field H_{so} is indicated.

measurements of the zero-bias stripe width and h. As H_B increases, those domains with $\overline{M}$ parallel to $\overline{H}_B$ expand, so that d_1 increases and d_2 decreases while d_1+d_2 remains roughly constant. The effective field gradient H' for zero-bias stripes is just the slope of either curve at the origin. In this example, the value 6.69 Oe/ μm is in good agreement with the experimental value, 6.4 ± 0.4 Oe/μm. As H_B increases further, the force balance required by Eq. (A.7) can only be achieved for larger values of d_1+d_2. Eventually, when H_B approaches the bubble stripe-out field H_{so}, the remaining stripes contract and form bubble domains.

Bubble Domains

The static properties of an isolated bubble domain were first calculated by Bobeck [2] for a strictly circular cross section. In the more general approach used here, due to Thiele [3,4], the bubble is allowed to deviate slightly from a circular cross section. A cylindrical coordinate system (r, ψ, z) is located in the center of the bubble with the z-axis perpendicular to the plane. The magnetization points along the -z-axis inside, and a along +z outside (see Fig. (1.2b)). The radius r is given as a function of ψ by the Fourier series

$$r(\psi) = r_o + \sum_{n=1}^{\infty} r_n \cos(n(\psi-\psi_n)) \quad . \tag{A.10}$$

Here, the expansion coefficients $\{r_n\}$ are small compared to r_o, and

wall bulging, i.e., $r(\psi,z)$, has been neglected. Though these assumptions are fairly restrictive, the results obtained here are in good agreement with experimental properties.

The equilibrium and stability conditions are obtained by expanding E_T in powers of r_n and ψ_n around the cylindrical reference state $r = a$, a constant. This expansion may be written as

$$E_T(r_o,\{r_n\},\{\psi_n\}) = E_T(a,o,o) +$$

$$+ \sum_{n=0}^{\infty}\left[\left(\frac{\partial E_T}{\partial r_n}\right)_a \Delta r_n + \left(\frac{\partial E_T}{\partial \psi_n}\right)_a \Delta\psi_n\right] +$$

$$+ \frac{1}{2}\sum_{n=0}^{\infty}\sum_{m=0}^{\infty}\left[\left(\frac{\partial^2 E_T}{\partial r_n \partial r_m}\right)_a \Delta r_n \Delta r_m + 2\left(\frac{\partial E_T}{\partial r_n \partial\psi_n}\right)_a \Delta r_n \Delta\psi_n\right.$$

$$\left. + \left(\frac{\partial^2 E_T}{\partial\psi_n \partial\psi_m}\right)_a \Delta\psi_n \Delta\psi_m\right] + \ldots \qquad \text{(A.11)}$$

For the domain to be in equilibrium, the first order terms must be zero. The domain is stable if the quadratic terms are a positive-definite function of the increments Δr_n and $\Delta\psi_n$. Many of the terms in Eq. (A.11) can be eliminated without calculating the necessary derivatives by making use of the symmetry properties of E_T for a cylindrical bubble. The term $r_1 \cos(\psi-\psi_n)$ corresponds to a translation of the bubble without changing shape. Since E_T does not depend on bubble location, all terms in Eq. (A.11) proportional to Δr_1 are zero. Furthermore, since E_T does not change when the domain is rotated, all terms proportional to ψ_n are also zero. This can also be shown

by direct calculation [3]. The only nonzero terms are proportional to either Δr_n or $\Delta r_n \Delta r_m$, and will be evaluated separately for the three components of E_T.

The first and second derivatives of E_W are obtained from $E_W = \sigma_w$ x (wall area). Since the wall area is h times the domain perimeter, E_W is given by

$$E_W = \sigma_w h \int_0^{2\pi} d\psi \left[r^2(\psi) + \left(\frac{dr}{d\psi}\right)^2 \right]^{\frac{1}{2}} \quad . \tag{A.12}$$

The only nonzero first derivative is

$$\left(\frac{\partial E_W}{\partial r_o} \right)_a = 2\pi\sigma_w h \quad . \tag{A.13}$$

This represents a uniform surface tension which tends to collapse the bubble. The only nonzero second derivatives are the diagonal terms,

$$\left(\frac{\partial^2 E_W}{\partial r_n^2} \right)_a = \frac{\pi\sigma_w h}{a} n^2 \text{ for } \quad n \geq 2 \quad . \tag{A.14}$$

The wall energy always increases when the shape of a circular bubble is perturbed, so that surface tension enhances bubble stability with respect to shape distortion.

The first and second derivatives of E_B are obtained from the expression,

$$E_B = M_S H_B h \int_0^{2\pi} d\psi \; r^2(\psi) \quad . \tag{A.15}$$

The only nonzero first derivative is

$$\left(\frac{\partial E_B}{\partial r_o}\right)_a = 4\pi a M_s H_B h \quad . \tag{A.16}$$

Since $\overline{H}_B$ opposes $\overline{M}$ inside the bubble, the bubble experiences a uniform pressure which tends to collapse the bubble. The only nonzero second derivatives are

$$\left(\frac{\partial^2 E_B}{\partial r_o^2}\right)_a = 4\pi M_s H_B h \quad , \tag{A.17a}$$

and

$$\left(\frac{\partial^2 E_B}{\partial r_n^2}\right) = 2\pi M_s H_B h \quad (n \geq 2) \quad . \tag{A.17b}$$

Like surface tension, the external bias field also enhances bubble stability against shape distortion.

The derivatives of E_d are obtained by evaluating the integral in Eq. (2.i.6d) for the surface charge distribution specified by $r(\psi)$. This energy has only one nonzero first derivative,

$$\left(\frac{\partial E_d}{\partial r_o}\right)_a = -(2\pi h^2)(4\pi M_s^2)\, G\left(\frac{2a}{h}\right) \quad , \tag{A.18}$$

where

$$G(x) = \frac{2x^2}{\pi}\left[\sqrt{1+x^{-2}}\, E\left(\frac{x^2}{1+x^2}\right) - 1\right] \quad .$$

Here, E is a complete elliptic integral of the first kind. Since G(x) is greater than zero for all x, the demagnetizing energy tends to expand the bubble, and return the sample to its demagnetized state,

as expected. The nonzero second derivatives are

$$\left(\frac{\partial^2 E_d}{\partial r_o^2}\right)_a = -(4\pi h)(4\pi M_s^2)\, G'(d) \quad , \tag{A.19a}$$

where $d = 2a/h$ is the dimensionless bubble diameter, and

$$\left(\frac{\partial^2 E_d}{\partial r_n^2}\right)_a = -(2\pi h)(4\pi M_s^2)\, G'(d)$$

$$+ \quad dh \quad (4\pi M_s^2)\left[L_n(d^{-2}) - L_n(o)\right] \quad , \tag{A.19b}$$

where $L_n(x)$ is given by

$$L_n(x) = \int_o^{\pi} d\alpha \quad \frac{1 - \cos n\alpha}{[x + \frac{1}{2}(1-\cos\alpha)]^{\frac{1}{2}}} \quad . \tag{A.19c}$$

These terms always decrease bubble stability against shape distortion.

Equilibrium conditions are obtained by setting the sum of the generalized forces for each independent perturbation equal to zero. Fortunately, all are associated with a uniform radius change, so that there is only one equilibrium condition. By combining the results from Eqs. (A.13), (A.16), and (A.18), and after dividing by $(2\pi h^2) \cdot (4\pi M_s^2)$, this condition may be written as

$$\lambda + \beta d - G(d) = 0 \quad . \tag{A.20}$$

This equation requires a force balance between surface tension and $\overline{H}_B$, which tends to collapse the bubble, and the demagnetizing force, which

tends to expand it.

Since all nondiagonal second derivatives are zero, the stability of the domain may be determined by separately considering each Fourier component. By combining the results of Eqs. (A.17a), and (A.19a), the stability condition for uniform changes in bubble radius may be written as

$$s_o > \lambda \quad , \tag{A.21a}$$

where

$$s_o(d) = G(d) - dG'(d) \quad . \tag{A.21b}$$

By combining the results of Eqs. (A.14), (A.17b), and (A.19b), the stability condition for n-fold shape distortion is

$$s_n < \lambda \quad , \tag{A.22a}$$

where

$$s_n(d) = -\frac{1}{n^2-1}\left[s_o(d) + \frac{d^2}{\pi}(L_n(d^{-2}) + L_n(o)\right] \quad . \tag{A.22b}$$

The overall stability of a bubble is achieved if the radial stability condition and each of the shape distortion conditions are satisfied by the force-free bubble geometry.

The equilibrium and stability conditions may be solved by using a relatively simple graphical technique. The functions G, s_o and s_2 are shown in Fig. (A.2) as a function of d. These functions are quite general, and do not depend on material parameters. The other

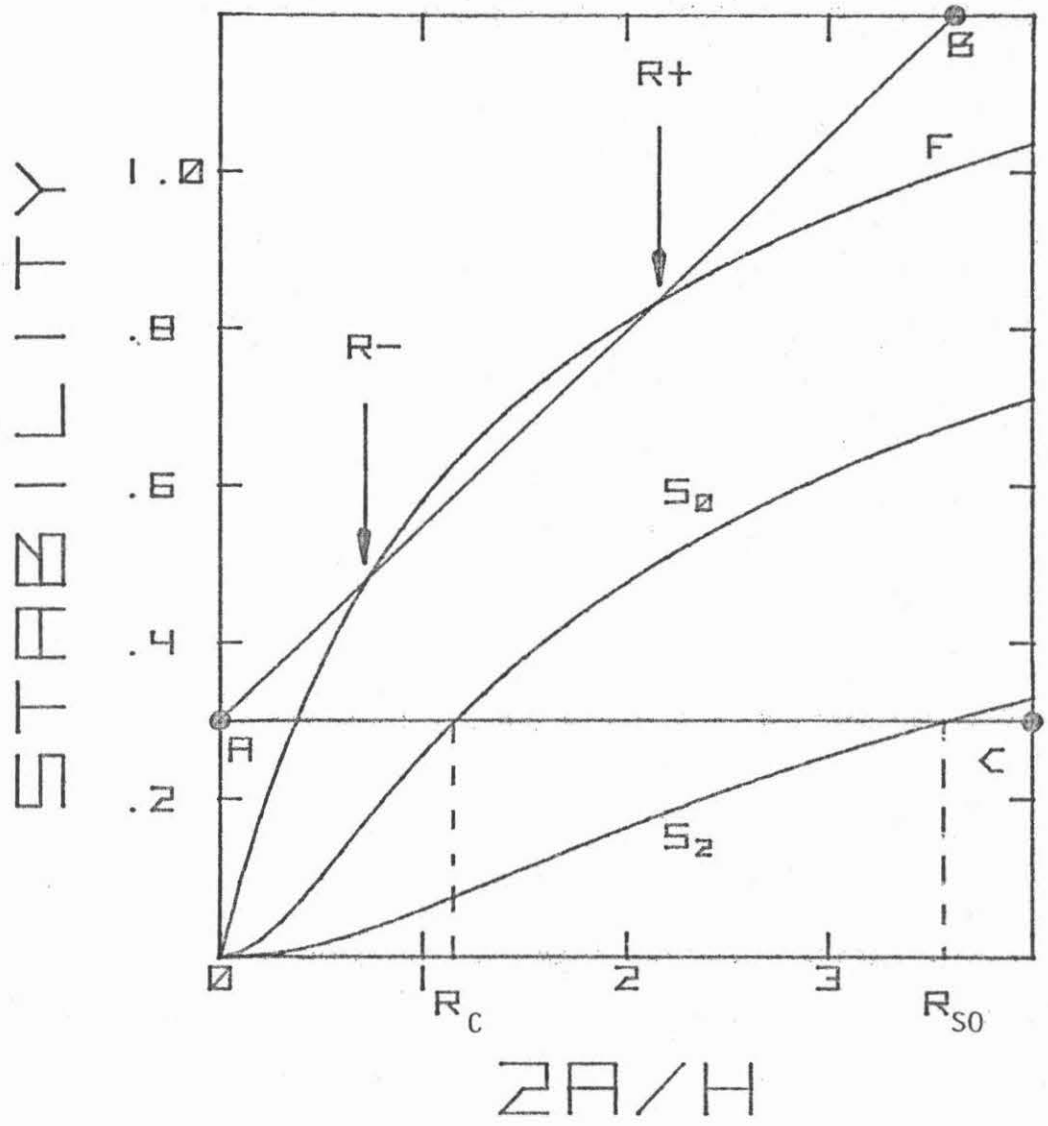

Fig. (A.2): Bubble Force Function G and Stability Functions s_o and s_2 as Functions of Bubble Diameter 2a/h. These functions are used in a graphical determination of bubble size and stability discussed in the text. The stripe-out radius r_{so} and collapse radius r_c are indicated. The radii r^+ and r^- represent force-free domain geometries. The lines $\overline{AB}$ and $\overline{AC}$ are constructed for $\lambda = 0.3$ and $H_B/4\pi M_s = 0.25$.

stability functions for $n > 2$ lie below s_2 and are not shown. Given h, $4\pi M_s$, ℓ, and H_B the equilibrium bubble radius may be determined by constructing a line $\overline{AB}$ with slope β, and y-intercept λ. The points where $\overline{AB}$ crosses G(d) correspond to solutions of the equilibrium condition. In general, there can be two equilibrium radii, r^+ and r^-. The stability of these solutions is determined by constructing a horizontal line $\overline{AC}$ with y-intercept λ. The point where $\overline{AC}$ crosses s_o determines the minimum bubble radius, called the collapse radius r_c, that can satisfy the radial stability condition. Since the equilibrium solution r^- is smaller than r_c, it always represents an unstable solution, and is usually not seen experimentally. Since r^+ is greater than r_c, it represents a stable solution, at least with respect to uniform radius changes. When H_B increases, the slope of $\overline{AB}$ increases, and r^+ and r^- move closer together. When H_B reaches the collapse field H_c, $\overline{AB}$ is tangent to G with $r^+=r^-=r_c$. For larger values of H_B, there are no equilibrium solutions. It is found experimentally that the bubble collapses, leaving the material saturated with $\overline{M}$ along $\overline{H}_B$. The point where $\overline{AC}$ crosses s_2 determines the maximum radius that can satisfy Eq. (A.22a) for n=2. This is called the stripe-out radius r_{so}. As H_B decreases, the slope of $\overline{AB}$ decreases, and r^+ increases. When r^+ reaches r_{so}, the bubble becomes unstable with respect to elliptical distortion. It is found experimentally that the bubble stripes-out, and forms a stripe domain.

The equilibrium radius is determined implicitly from Eq. (A.20), and the results for the sample investigated in Ch. 3 are shown in Fig.

(A.3). The radius r^+ decreases rapidly with increasing H_B over its stable range. For larger values of λ, the r^+ curve is below and to the left of the curve shown here, while for higher values, the curve is higher, and to the right. In this case, r^+ varies by a factor of three while H_B only varies by a factor of 1.4. Since $r^+(H_B)$ is almost linear, it is convenient in analyzing bias pulse experiments to approximate it by a straight line with slope $(H')^{-1}$. The value of H' at $\beta = 0.252$ (H_B=24 Oe) is 2.0 Oe/μm, in good agreement with the experimental value, 2.2 ± 0.3 Oe/μm. Note that this value is more than three times smaller than H' in parallel stripe domains, so that the domain configuration has a significant effect on the effective field gradient.

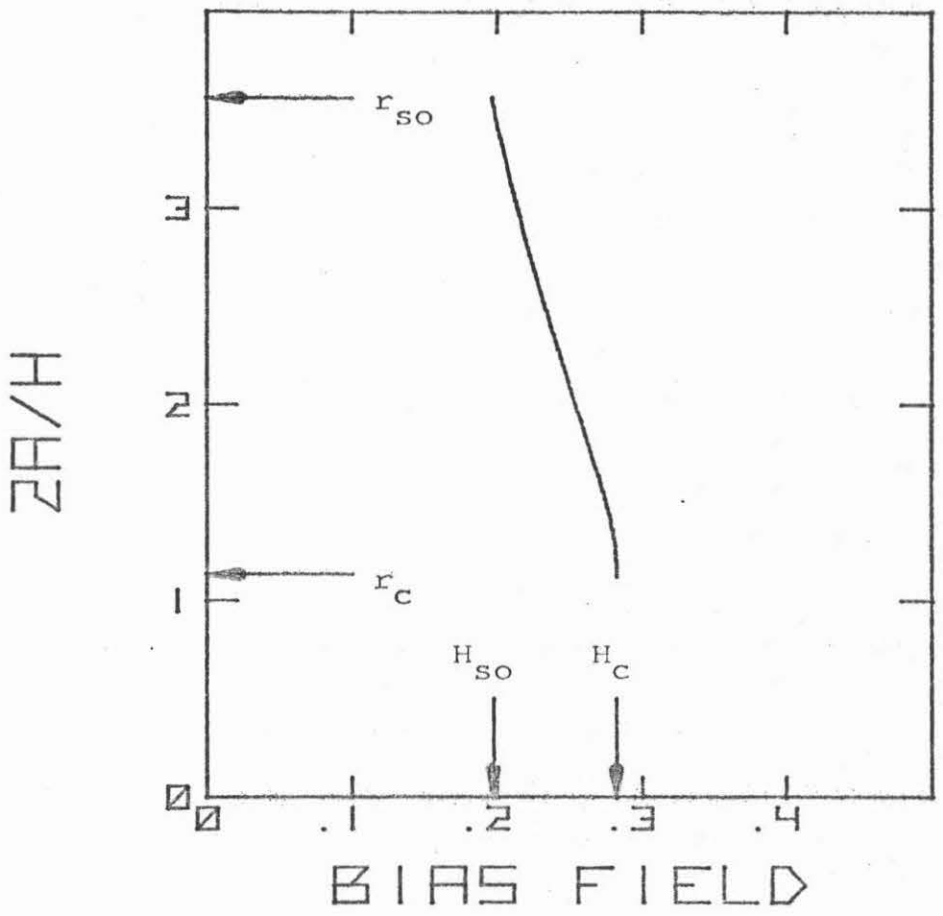

Fig. (A.3): Equilibrium Bubble Diameter 2a/h as a Function of Bias Field $H_B/4\pi M_s$ for the case $\lambda = 0.3$. The collapse radius, stripe-out radius, collapse field H_c and stripe-out field H_{so} are indicated.

References

1. C. Kooy and U. Enz, Philips Res. Repts., 15, 7 (1960).

2. A. H. Bobeck, Bell Syst. Tech. J. 46, 1901 (1967).

3. A. A. Thiele, Bell Syst. Tech. J. 48, 3287 (1969).

4. A. A. Thiele, Bell Syst. Tech. J. 50, 725 (1971).

Appendix B. Experimental Apparatus

The sampling optical microscope system used in this work uses the Faraday effect to obtain transient pictures of magnetic domains during pulsed field experiments. In contrast with stroboscopic systems, in which the necessary image intensity is obtained by repeated illumination at a high repetition rate (typically 3 kHz), this system uses a single laser flash to provide visible images. The flash is short enough so that domain walls never move a significant distance (<0.1 μm) during the exposure time. Domains are manipulated by a combination of static and dynamic magnetic fields directed both parallel and perpendicular to the sample plane. The relative timing between the field pulses and laser flash is controlled by a custom-built sampling unit. In this way, the system provides pictures of transient domain wall behavior during single experimental events. The system can also be easily modified to conduct photometric measurements, which provide greatly enhanced spatial resolution. This versatile system has proven to be a useful tool in studying domain wall dynamics.

The static and dynamic field environment is provided by current conductors. The uniform static bias field necessary for bubble stability is provided by placing the sample in the center of a bias field coil (4 cm i.d. x 8 cm o.d. x 2.5 cm). This field is calibrated by measuring the bubble collapse field of a standard sample. Static in-plane fields come from a pair of large coils (10 cm i.d. x 35 cm o.d. x 6 cm) mounted on either side of the sample. Calculations show

that this field, which is calibrated with a magnetometer, is uniform over the sample volume to within 2%. Bias field pulses are provided by a 1mm-diameter 5-turn pancake coil mounted just below the sample. When driven by an HP214A pulse generator, this coil has a 12 nsec rise time with no visible ringing present. Calculations show that the bias component of the pulsed field is uniform over the 200 μm-diameter field of view to within 2%, while the in-plane component is limited to 6% of the bias component. The pancake coil is calibrated by observing changes in bubble collapse field produced by d.c. currents. These coils provide static and dynamic control over fields perpendicular to the sample plane, and static control over in-plane fields.

A block diagram of the sampling microscope system is shown in Fig. (B.1). The sequence begins when the TV camera sends a trigger pulse to the sampling unit. This unit then triggers an Avco Everett flowing nitrogen laser at a controlled time relative to the field pulses. The laser produces a 10 nsec pulse of UV light (3371 Å) with 100 kW peak power. The nitrogen laser pumps a rhodamine 6G dye laser, which provides a 10 nsec pulse of yellow (5800 Å) light with about 1 kW peak power. This light is polarized by a prism polarizer and then undergoes Faraday rotation as it passes through the sample. Contrast is produced with a sheet analyzer. The polarizer and analyzer are part of a Leitz Ortholux polarizing microscope in which most of the optical elements have been removed, leaving only the condenser lens, a 32X objective lens, and a 5X eyepiece. A real image of the domains

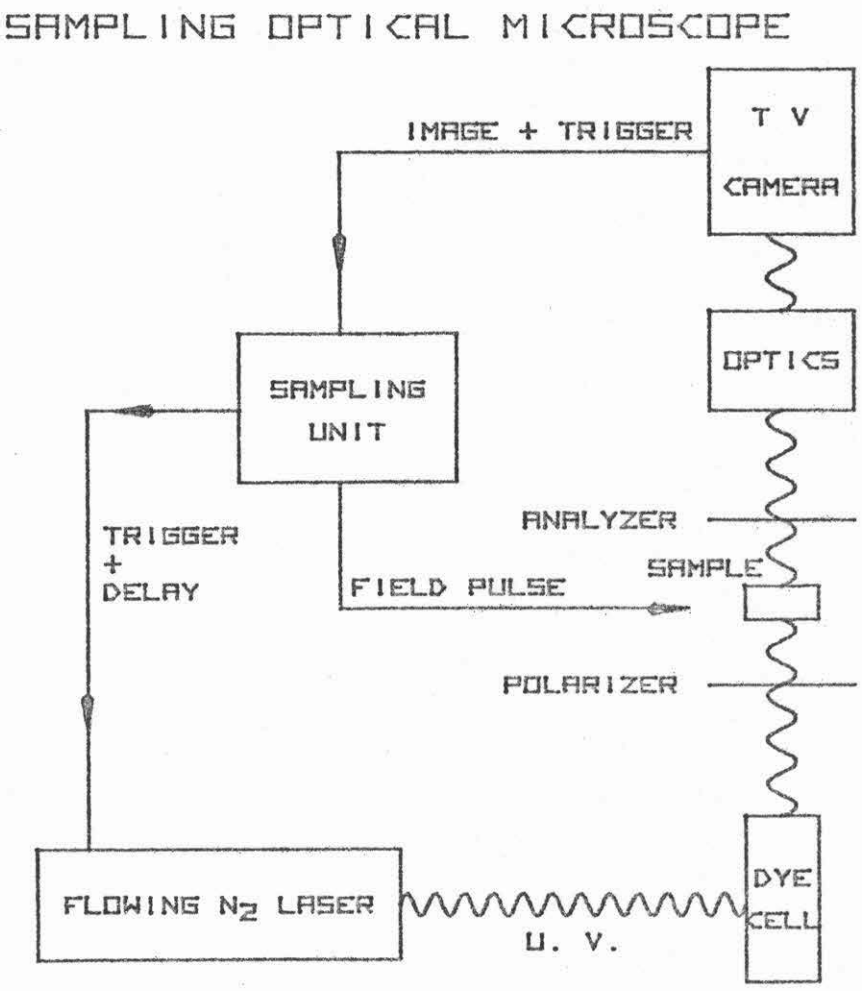

Fig. (B.1): Bloch Diagram of the Sampling Optical Microscope Used in this Work. System operation is described in the text.

is produced on the target of a Cohu 4400 SIT TV camera, which retains the image for about three vertical scans. This image is then sent to the sampling unit for processing and recording. The spatial resolution obtained by optical sampling is limited by diffraction effects to about 0.2 μm, while temporal resolution is limited by the laser pulse width to about 10 sec.

A block diagram of the sampling unit is shown in Fig. (B.2). The core of this unit is a programmable sequencer, which controls eight independent trigger lines during up to 64 program steps. In the simple example shown here, the first line is used to trigger an HP214 A pulse generator, which provides the bias field pulses, and the eighth line triggers a Tektronix 3T77 sampling sweep generator, which later triggers the nitrogen laser after a controlled delay. The image from the TV camera is encoded with digital information from the sequencer and from the sampling unit and then recorded on video tape with a Sanyo VTR 1200 recorder. Encoded information may include the delay time, the particular trigger combination being executed, the program step number, the frame number, the static bias and in-plane fields, etc. The time of the laser flash is monitored by placing a beam splitter and PIN diode in the optical path just before the light enters the microscope. The time of the current pulse is monitored by a 0.5 nsec-rise time Tektronix CT-2 current probe. The relative timing between these two signals is monitored on an oscilloscope and may be controlled to within 1 nsec. The ability to program different trigger patterns has proven to be very useful, especially

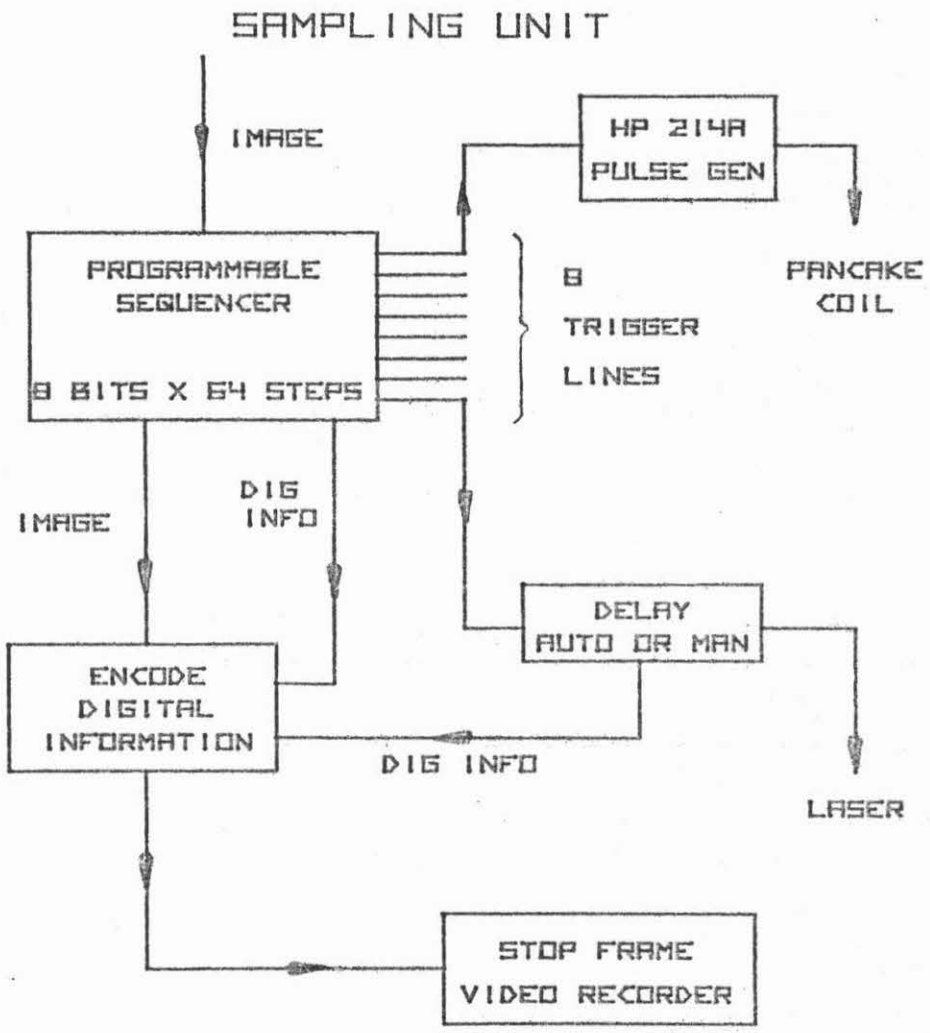

Fig. (B.2): Block Diagram of the Sampling Unit Used to Control the Experiments. Operation is described in the text.

in more complex experimental situations.

A block diagram of the photometric experiment is shown in Fig. (B.3). Light from the dye laser is split into two beams. The first (A) goes through the sample and polarizing microscope, and its intensity is measured with a UDT PIN 10 photodiode. The laser power is monitored by measuring the intensity of the second beam with a similar diode. Electrical signals from the diodes are amplified by low-noise dual FET amplifiers. The gain of these amplifiers is adjusted so that the output signals are approximately equal. Diode capacitance, together with the limited frequency response, combine to widen the 10 nsec laser pulse into a 0.5 msec electrical pulse. Since this signal still only occupies 2% of the duty cycle (30 Hz repetition rate), latch and hold circuits are used to retain the peak signal voltages throughout the entire cycle. The latches are automatically reset by a self-trigger circuit at the beginning of each cycle. Electrical signals from the latch and hold circuits are subtracted in order to compensate for fluctuations in laser power (<10%). This difference signal is detected by a PAR HR-8 lock-in amplifier, using either 1 or 5 sec time constants. The bias pulse is only applied on alternate laser flashes, and the signal is detected at half of the laser frequency (i.e., 15 Hz) in order to compensate for small changes in the domain configuration. The averaged signal is plotted on an HP 7005B X-Y recorder as a function of delay time. The noise level in the output signal is equivalent to an effective spatial resolution of 0.03 μm, while temporal resolution is still limited by the

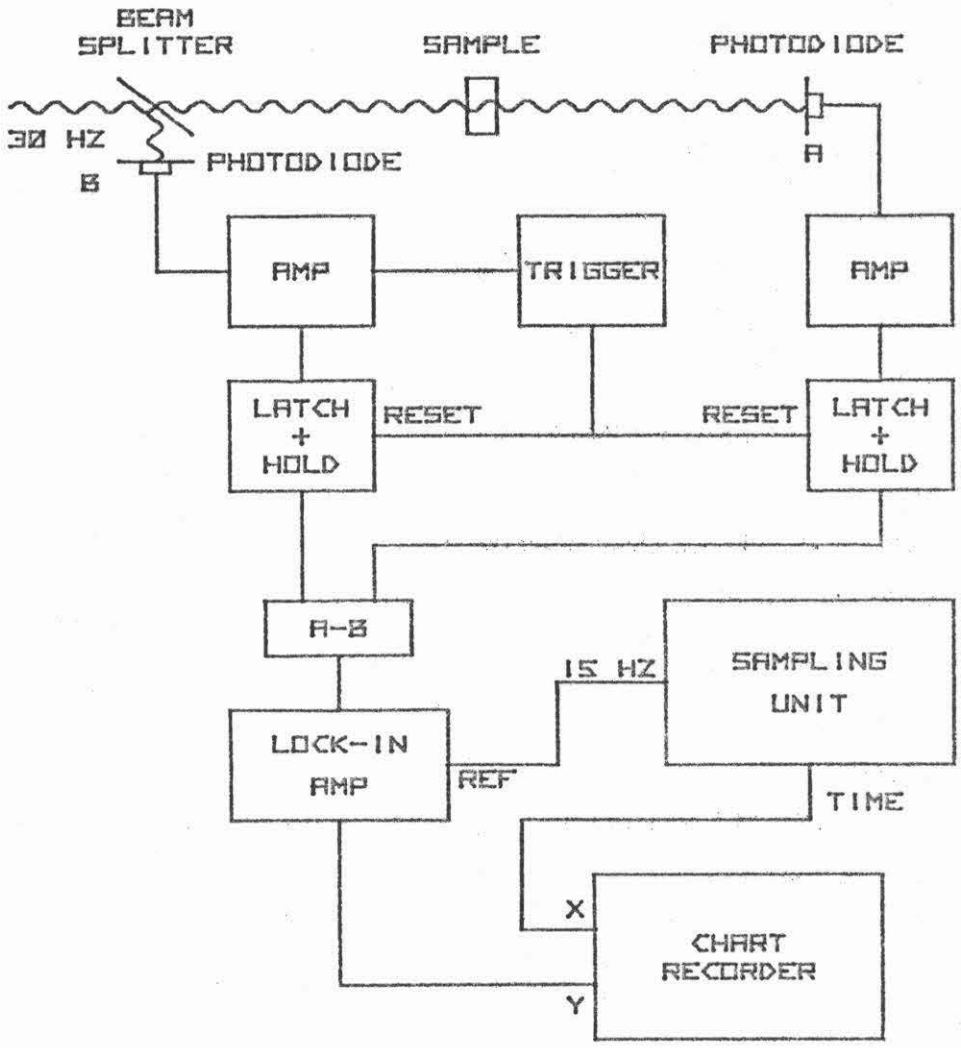

Fig. (B.3): Block Diagram of the Photometric Experiment. Operation is described in the text.

laser pulse width to about 10 nsec. By giving up the ability to monitor individual experimental events, the photometric experiment provides an order of magnitude improvement in resolution over optical sampling.

Appendix C. Notation

Magnetic Units

The cgs system is used throughout. Magnetic fields $\overline{H}$ are measured in oersteds (Oe) and magnetic induction $\overline{B}$ is measured in gauss. The relationship between these units and their MKS counterparts is given by

$$1 \text{ Oe} = 79.58 \text{ amps/m} \quad , \tag{C.1a}$$

and

$$1 \text{ gauss} = 10^{-4} \text{ webers/m}^2 \tag{C.1b}$$

Conventions

1. Vector quantities are indicated by a bar over the symbol, e.g., $\overline{H}$. Vector components are indicated by a subscript, e.g., H_x is the x-component of $\overline{H}$.

2. Partial derivatives with respect to time are indicated by a dot over the symbol, e.g.,

$$\frac{\partial \theta}{\partial t} = \dot{\theta} \tag{C.2a}$$

and

$$\frac{\partial^2 \theta}{\partial t^2} = \ddot{\theta} \tag{C.2b}$$

3. Partial derivatives with respect to spatial coordinates are indicated by subscripts, e.g.,

$$\frac{\partial\theta}{\partial x} = \theta_x \quad , \tag{C.3a}$$

and

$$\frac{\partial^2\theta}{\partial x^2} = \theta_{xx} \quad . \tag{C.3b}$$

However, subscripts on vector quantities indicate vector components, and not spatial derivatives.

4. Magnetic fields are sometimes scaled to H_k, the anisotropy field. Such fields are indicated by lower case letters, e.g., $\overline{H}/H_k = \overline{h}$, and $H_x/H_k = h_x$.

5. Averaged values through the film thickness are indicated by brackets, e.g.,

$$h^{-1}\int_0^h dz\ \phi(z) = \langle\phi\rangle \quad . \tag{C.5}$$

Use of Symbols

A table of symbols together with a brief description and units is given below. The first part of the table lists Latin symbols used in this work in alphabetical order, and the second part lists Greek symbols also in alphabetical order.

Latin Symbols	Description (units)
A	exchange constant (erg/cm)
d	dimensionless bubble diameter
d_1, d_2	stripe domain widths (cm)

E_B	bias field energy (erg or erg/cm^2)
E_d	demagnetizing energy (erg or erg/cm^2)
E_T	total domain energy (erg or erg/cm^2)
E_w	wall energy (erg or erg/cm^2)
F	dissipation per unit volume (erg/cm^3-sec)
F_a	dissipation per unit wall area (erg/cm^2-sec)
$\overline{H}$	magnetic field (Oe)
h	film thickness (cm)
H'	effective field gradient (Oe/cm)
H_a	magnitude of the externally applied bias field pulse (Oe)
$\mathcal{H}_a$	Hamiltonian per unit wall area (erg/cm^2)
$\overline{H}_B$	external bias field (Oe)
H_{co}	bubble collapse field (Oe); coercive field (Oe)
H_d	demagnetizing field (Oe)
$\overline{H}_{ip}$	in-plane field (Oe)
H_k	anisotropy field (Oe)
H_s	perpendicular component of surface demagnetizing field (Oe)
H_{so}	bubble stripe-out field (Oe)
H_{sv}	effective drag field resulting from saturated wall velocity (Oe)
H_w	Walker field (Oe)
K_u	uniaxial anisotropy energy density (ergs/cm^3)
L	Lagrangian per unit volume (erg/cm^3)
$\overline{L}$	angular momentum per unit volume (Oe^2 sec/cm)

ℓ	characteristic length (cm)
L_a	Lagrangian per unit wall area (erg/cm^2)
$\overline{M}$	magnetic moment per unit volume or magnetization (Oe)
m	effective wall mass per unit area (gm/cm^2)
m_D	Döring mass (gm/cm^2)
M_s	saturation magnetization, $\|\overline{M}\|$ (Oe)
Q	quality factor
q	wall position (cm)
r	bubble radius (cm)
v	steady-state wall velocity (cm/sec)
v_o	average wall velocity (cm/sec)
v_p	peak steady-state velocity attainable with an HBL present (cm/sec)
v_s	saturated wall velocity (cm/sec)
v_w	Walker velocity (cm/sec)
w	kinetic energy per unit volume (erg/cm^3)
W_L	HBL width (cm)
z_{c1}, z_{c2}	locations of the critical points (cm)
z_L	HBL position (cm)

Greek Symbols	Description (units)
α	Gilbert damping parameter
β	dimensionless bias field
γ	gyromagnetic ratio ($Oe^{-1}sec^{-1}$)
Δ	wall width (cm)

Δ_B	Bloch wall width (cm)
Δ_N	Neél wall width (cm)
ε_L	HBL energy per unit wall length (erg/cm)
θ	polar angle between $\overline{M}$ and +z-axis
θ^o	asymptotic value of θ far from the wall
λ	dimensionless characteristic length
μ	wall mobility (cm/sec-Oe)
ν	wall oscillation frequency (Hz)
ρ_E	potential energy per unit volume (erg/cm^3)
ρ_E^o	asymptotic value of ρ_E (erg/cm^3)
σ_B	Bloch wall energy per unit area (erg/cm^2)
σ_{KE}	kinetic wall energy per unit area (erg/cm^2)
σ_N	Neél wall energy per unit area (erg/cm^2)
σ_w	wall energy per unit area (erg/cm^2)
$\tau/2$	half-period of wall oscillations (sec)
ϕ	azimuthal angle between projection of $\overline{M}$ in the x-y plane and the +x-axis
ϕ^o	asymptotic value of ϕ far from the wall
ϕ_o	static orientation of ϕ
ϕ^i	value of ϕ inside the domain wall